UC Irvine
UC Irvine Electronic Theses and Dissertations

Title

Investigations into the Reactivity of Transition Metal Complexes with Redox-Active Ligands for Proton Coupled Electron Transfer and Nitrene Transfer

Permalink

https://escholarship.org/uc/item/2p70w8nm

Author

Charette, Bronte Joan

Publication Date

2021

Peer reviewed|Thesis/dissertation

UNIVERSITY OF CALIFORNIA,
IRVINE

Investigations into the Reactivity of Transition Metal Complexes with Redox-Active Ligands for
Proton Coupled Electron Transfer and Nitrene Transfer

DISSERTATION

submitted in partial satisfaction of the requirements
for the degree of

DOCTOR OF PHILOSOPHY

in Chemistry

by

Bronte Joan Charette

2021

DEDICATION

For

Mom and Dad

In loving memory

Lloyd Levy
November 20, 1931 – February 22, 2021

Carleigh Boutang
April 26, 1977 – November 8, 2020

Love doesn't die only people do

TABLE OF CONTENTS

Page

LIST OF FIGURES

LIST OF TABLES

LIST OF SCHEMES

LIST OF EQUATIONS

ACKNOWLEDGEMENTS

<div align="center">**CIRRICULUM VITEA**</div>

Bronte Joan Charette

Education

University of California, Irvine

<div align="right">**September 2016–April 2021**</div>

- Ph.D Chemistry <div align="right">Advisor: Professor Alan Heyduk</div>

  o My research is focused on synthetic inorganic chemistry, specifically the preparation, characterization, and analysis of thermodynamic, and kinetic properties of novel transition metal complexes with redox active ligands.

University of Manitoba

<div align="right">**September 2014–August 2016**</div>

- M.Sc. Chemistry <div align="right">Advisor: Professor Jamie Ritch</div>

  o This research was focused on the preparation and characterization of new ligands to achieve novel coordination behavior. I developed efficient synthetic routes to a series of pincer ligands containing common and uncommon donor atoms such as Se, Te.

The University of Winnipeg

<div align="right">**September 2009– April 2014**</div>

- B.Sc. Chemistry (Honours)

  o Honours research project with Professor Jamie Ritch in Inorganic Synthesis (September 2013-April 2014).

  o Directed studies project with Professor Tabitha Wood in Organic Synthesis (September 2013-December 2013).

University of New England (Australia)   **February– November 2011**

- International exchange program

Teaching Experience

University of California, Irvine

Instructor of Record   **September 2019- December 2019**
- Lecturer for Freshman General Chemistry Lecture

Supervisor: Professor Alan Heyduk   **January 2020-March 2020**
- Teaching Assistant for Graduate Level Physical Inorganic Chemistry

Supervisor: Professor Alan Heyduk   **April 2018-June 2019**
- Teaching Assistant for Honors General Chemistry Lecture

Supervisor: Professor William Evans   **January 2017- April 2018**
- Laboratory Instructor for Advanced Inorganic Chemistry Laboratory

Supervisor: Professor Kimberly Edwards   **August 2017- September 2017**
- Laboratory Instructor for General Chemistry Laboratory

Supervisor: Professor Susan King   **September 2016- June 2017**
- Laboratory Instructor for Honors Organic Chemistry Laboratory

The University of Winnipeg

Supervisor: Professor Devin Latimer   **September 2014- April 2016**
- Laboratory Instructor for Organic Chemistry Laboratory

Supervisor: Professor Joshua Hollett   **January 2014- April 2016**
- Teaching Assistant for Physical Chemistry Lecture

Awards, Certifications and Presentations

University of California, Irvine
- Department of Chemistry Dissertation Fellowship (2021)
- Department of Chemistry Most Promising Future Faculty Award (2020)
- Graduate Dean's Dissertation Fellowship (2020)
- Center for Integration of Research, Teaching and Learning - Associate Level (2019)

- Division of Teaching Excellence and Innovation - Course Design Certificate (2019)

- Mentorship Excellence Program (2019)

- Graduate Interconnect Mentorship Program – Mentor (2019)

- Department of Chemistry Safety Award (2018)

- Department of Chemistry Outstanding First Year Teaching Assistant (2017)

Natural Sciences and Engineering Research Council of Canada

- Postgraduate Fellowship – Doctoral (2018)

University of Manitoba

- Hugh J. Anderson Graduate Award in Chemistry (2015)

- Employees Scholarship (2015)

- Faculty of Graduate Studies Travel Award (2015)

- Chemistry Graduate Students Association Travel Award (2015)

- Graduate Students Association Travel Award (2015)

The University of Winnipeg

- Award for Excellence in Chemistry Laboratory Instruction (2015)

- Department of Chemistry Faculty Scholarship (2010, 2011, 2012, 2013)

- Entrance Scholarship (2009)

ACS San Diego 2019

- Poster Presentation (August 2019)

Pacifichem 2015

- Finalist in Graduate Student Poster Competition (December 2015)

International Symposium on Inorganic Ring Systems

- Poster Presentation (July 2015)

Canadian Chemical Conference and Exhibition

- Oral Presentation (June 2015)

- Poster Presentation (June 2014)

- Poster Presentation (June 2014)

Publications

- **Charette, B. J**.; Ziller, J. W.; Heyduk, A. F. Exploring ligand-centered hydride and H-atom transfer. *Inorg. Chem.* **2021**, 60, 5367-5375.

- **Charette, B. J**.; Ziller, J. W.; Heyduk, A. F. Metal ion influence on ligand-centered hydrogen atom transfer. *Inorg. Chem.* **2021**, 60, 1579-1589.

- Heyduk A. F.; **Charette, B. J**. Redox-Active Catecholate-Type Ligands. *Comprehensive Coordination Chemistry III*. 3rd ed. Elsevier, **2021**.

- Rosenkoetter, K. E.; Wojnar, M. K.; **Charette, B. J.**; Ziller, J. W.; Heyduk, A. F. Hydrogen-atom noninnocence of a tridentate [SNS] pincer ligand. *Inorg. Chem*. **2018**, 57, 9728-9737

- **Charette, B. J.**; Ritch, J. S. A selenium-containing diarylamido pincer ligand: synthesis and coordination chemistry with group 10 metals. *Inorg. Chem*. **2016**, 55, 6344-6350

- Ritch, J. S.; **Charette, B. J.** An Experimental and Computational Comparison of Phosphorus and Selenium-Based Ligands for Catalysis. *Can. J. Chem*. **2016**, 94, 386-391.

- **Charette, B. J.**; Ritch, J. S. Crystal structure of 1-bromo-2-(phenylselenyl)- benzene. *Acta. Cryst*. **2015**, E71: 327-329.

- **Charette, B. J**.; Ziller, J. W.; Heyduk, A. F. Reactivity of a Co(II) [SN(H)S] complex with aryl-azides: evidence for multi-site electron-proton transfer (MS-EPT). *In preparation.*

Activities

- Mentor for University of California, Irvine Competitive Edge Program (2020)

- Graduate student liaison/panelist for University of California, Irvine Chemistry Department Recruitment (2017-2020)

- Senior TA mentor for University of California, Irvine Chemistry Department Zoom Training Sessions (2020)

- Volunteer for University of California, Irvine Graduate Division Orientation and International Graduate Student Orientation (2019)

- Mentor for University of California, Irvine Graduate Interconnect Program (2019)

- Judge for SoCal Undergraduate Research Symposium Poster Competition (2018)

- Safety Representative for Heyduk Research Group (2017-2020)

- Graduate student representative for University of Manitoba Senate Nominations Committee (2015)

- Executive member of the University of Manitoba Chemistry Graduate Students Association (2014-2015)

- Assistant Coach for Peewee Girls Hockey Team (2012-2016)

- Student ambassador for Chemistry Department in University of Winnipeg Open House (2013)

- Vice-president of the University of Winnipeg Chemistry Club (2012-2013)

ABSTRACT OF THE DISSERTATION

Investigations into the Reactivity of Transition Metal Complexes with Redox-Active Ligands for Proton Coupled Electron Transfer and Nitrene Transfer

by

Bronte Joan Charette

Doctor of Philosophy in Chemistry

University of California, Irvine, 2021

Professor Alan F. Heyduk, Chair

The theme of this dissertation centers around understanding the propensity of transition metal complexes with redox and proton non-innocent ligands to serve as proton and electron transfer agents either in proton-coupled electron transfer or group transfer reactivity.

Chapter 2 describes kinetic and thermodynamics investigations into ligand-centered hydrogen-atom transfer (HAT) reactivity for a family of Group 10 metal complexes containing a tridentate pincer ligand derived from bis(2-mercapto-*p*-tolyl)amine, $[SNS]H_3$. Six new metal complexes of palladium and platinum were synthesized with the [SNS] ligand platform in different redox and protonation states to complete the Group 10 series previously reported with nickel. Hydrogen-atom transfer (HAT) reactivity was examined for this family of nickel, palladium, and platinum complexes to determine the impact of metal ion on the ligand-centered reactivity.

Chapter 3 discusses the preparation of a *pseudo*-tetrahedral cobalt (II) complex bearing the redox and proton non-innocent ligand, $[SN(H)S]^{2-}$. The $[SN(H)S]Co(DMAP)_2$ complex was subject reactivity studies with *p*-tolylazide to reveal its transformation into *p*-toluidine through two H-atom transfers. To elucidate the electronic structure of the cobalt by-product, reactivity studies with TEMPO•, DFT studies and kinetic analysis were conducted and indicated a resulting four-coordinate square planar [SNS]Co(DMAP) as a result electron transfer from the metal and ligand deprotonation through a binuclear mechanism.

Chapter 4 examines a new nickel(II) complex, [ON(H)O]Ni(PPh₃) ([ON(H)O]$^{2-}$ = bis(3,5-di-tert-butyl-2-phenoxy)amine), bearing a protonated redox-active ligand, for its ability to serve as a hydrogen-atom (H$^\bullet$) and hydride (H$^-$) donor. Bond dissociation free energy (BDFE) and hydricity (ΔG°_{H-}) measurements benchmark the thermodynamic propensity of this complex to participate in ligand-centered H$^\bullet$ and H$^-$ transfer reactions. The products of both (H$^\bullet$) and hydride (H$^-$) reveal interesting nickel products with unusual geometries.

Chapter 5 investigates ligand displacement and nitrene transfer reactivity for the anionic {[ONO^{cat}]Ni(L)}$^{1-}$ complex where L = PPh₃ and pyridine. Here the redox active ligand undergoes a single electron transfer to a nitrene substrate while the metal remains in the same oxidation date through a binuclear pathway. While the nickel imido complex was unable to be isolated and fully characterized, the identification of a two-electron nitrene transfer product, carbodiimide, suggests a transient nickel imido complex.

Appendix A examines the potential diverted pathways and side-products formed during the unsuccessful catalytic reactivity and attempts to isolate the nickel imido discussed in Chapter 5.

Chapter 1

Introduction

1.1 Proton and Electron Storage in Transition-metal Coordination Complexes

Many fundamental and important chemical and biological processes are dependent on the management of protons and electrons. A simple example is the conversion of water (H_2O) into oxygen and hydrogen (O_2 and H_2); this process requires a net transfer of four electrons and four protons. Water oxidation is a target reaction for the emerging field of solar energy, which focuses on harvesting sustainable energy production.[1–4] In nature, these transformations are generally carried out in enzymes that contain active sites bearing first-row transition metal centers such as Mn, Fe, Co, Ni, and Cu. These metals are often limited to one-electron processes; therefore, redox-active cofactors such as tyrosine are incorporated to mediate additional electron transfers. The change in negative charge density in such systems triggers changes in proton affinities; therefore, to avoid charge build-up, protons stored on amino-acid side chains like the histidine residue His-190 in Photosystem II,[5–9] are often transferred in concert. Biomimetic complexes aim to emulate these transformations by incorporating ligands that can access multiple oxidation and protonation states into coordination complexes with first-row transition metals.[10–12] A recent example of a copper-based system with the redox-active 6,6'-dihydroxy-2,2'-bipyridine ligand has shown to be a highly active water oxidation catalyst under basic conditions.[13] As shown in **Scheme 1.1**, the redox-active ligand serves as an electron reservoir akin to the tyrosine radical in Photosystem II in addition to assisting in proton-coupled electron transfers through the hydroxy groups.

Scheme 1.1. Electron and proton management in Photosystem II (left) and Ligand-Assisted Cu–L biomimetic system (right). Scheme adapted from reference 13.

Photosystem II

Biomimetic system
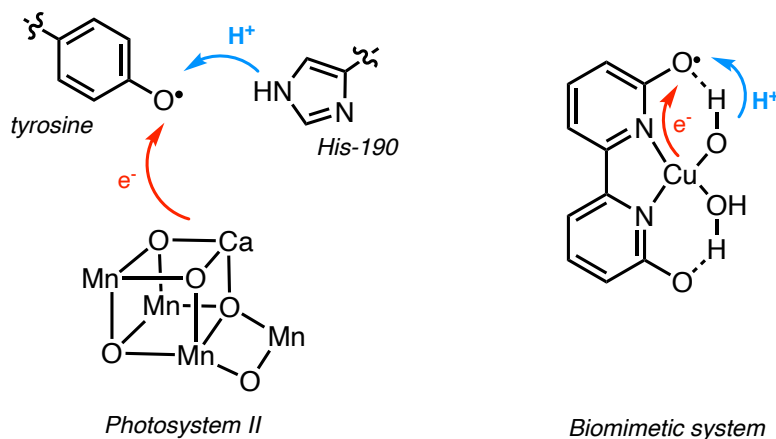
1.2 Redox-Active Ligands

Redox-active ligands constitute a class of ligand that can exist in multiple oxidation states when coordinated to metal ions. The redox activity of these ligand platforms is derived from frontier molecular orbitals that lie close in energy to the valence orbitals of the coordinated metal ions. These frontier ligand orbitals are often π and π^* type orbitals of unsaturated organic molecules containing two or more heteroatom (N, O, S) donors in conjugation through double bonds. Due to the close energetic proximity of the metal and ligand frontier orbitals in coordination complexes, the complexes often display "non-innocent" behavior, as coined by Jørgensen in 1966,[14] in which there is substantial ambiguity in the assignment of the metal oxidation state. This effect is well illustrated by one of the simplest redox-active ligands, nitric oxide (NO). **Scheme 1.2** shows that when coordinated to a metal ion, NO can adopt three different oxidation states, (a) nitrosyl cation, NO^+, which is isoelectronic with CO, (b) the neutral nitric oxide radical, $NO^{\bullet}$, and (c) the bent nitroxide anion, NO^-.

Scheme 1.2. Possible oxidation state assignments for a metal-nitrosyl complex.
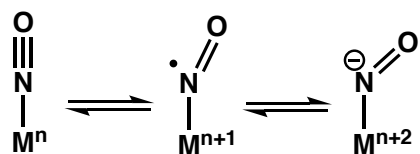
The ambiguity associated with assigning metal and ligand oxidation states in these complexes is well known and spurred the development of a unique electron-counting formalism.[15] The manifold of frontier molecular orbitals in redox-active ligand coordination complexes also engender rich electrochemical behavior at mild potentials and dramatic spectroscopic profiles throughout the visible and near-IR regions of the electromagnetic spectrum. Accordingly, the spin and electron-transfer properties of these coordination complexes have attracted the interest of researchers looking to utilize them in a variety of chemical applications.
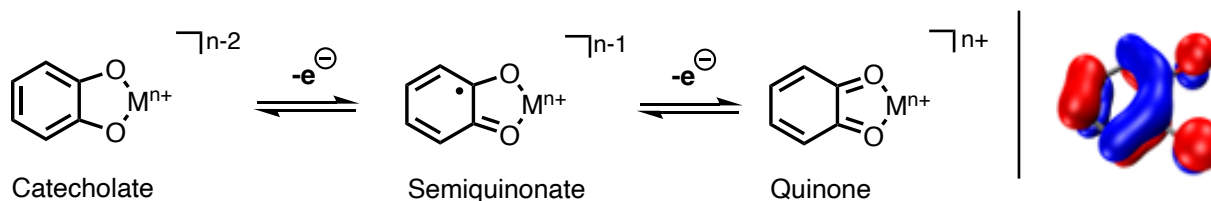
Figure 1.1. (Left) Three oxidation states of the catecholate ligand. (Right) Calculated redox-active molecular orbital of a catecholate ligand.

A prototypical redox-active ligand is catecholate, which has demonstrated the ability to exist in three oxidation states, catecholate, semiquinonate, and quinone, shown in **Figure 1.1**. Qualitative insight into the ligand oxidation state is readily accessible from analysis of the electronic and vibrational spectra. Complexes with catecholate-type ligands are often intensely colored, especially when the ligands are present in the oxidized semiquinonate and quinone forms. Intra-ligand $\pi \rightarrow \pi^*$ transitions, as well as charge transfer transitions involving multiple ligands (ligand to ligand charge transfer (LL'CT)) or a ligand and the coordinated metal ion (metal to ligand charge transfer (MLCT) and ligand to metal charge transfer (LMCT)), typically dominate

the visible and near-IR portions of the electronic absorption spectrum ($\lambda > 600$ nm).[16–18] In vibrational spectra, the oxidized forms of these ligands often show sharp, strong bands between 1100-1400 cm^{-1}.[19,20] Nuclear magnetic resonance (NMR) and electron paramagnetic resonance (EPR) spectroscopies are useful for characterizing diamagnetic and paramagnetic complexes, respectively. For diamagnetic complexes, ^{1}H NMR chemical shift values tend to vary dramatically with the oxidation state of the ligand. In cases where a ligand radical is coordinated to a diamagnetic metal ion, EPR spectra resemble those of organic radicals with simple isotropic signals near $g = 2.00$ indicative of $S = \frac{1}{2}$ spin systems.[16,21–23] Complexes with both open-shell ligands and open-shell metal ions are typically characterized by anti-ferromagnetic coupling between the unpaired electrons on the metal and ligand. In some cases, this property can simplify the characterization of the complex; for example, the coordination of three semiquinonate ligands to a chromium(III) ion, as shown in **Scheme 1.3,** results in a diamagnetic complex with an overall $S = 0$ spin state.[24] In other cases, anti-ferromagnetic coupling makes the correct assignment of the complex more complicated; for example, either cobalt(III)-catecholate or cobalt(II) semiquinonate oxidation states are proposed for cobalt catecholate complexes due to valence tautomerization and anti-ferromagnetic coupling.[25] For complicated spin systems, both EPR, and thorough magnetic susceptibility measurements are required to analyze and deconstruct the complex spin state into ligand and metal contributions.

Scheme 1.3. Anti-ferromagnetic coupling between Cr[III] and three semiquinonate ligands (left) and valence tautomers of Co[III/II] and catecholate and semiquinonate ligands. (right).

$S = 0$ $S = 0$ $S = 0$
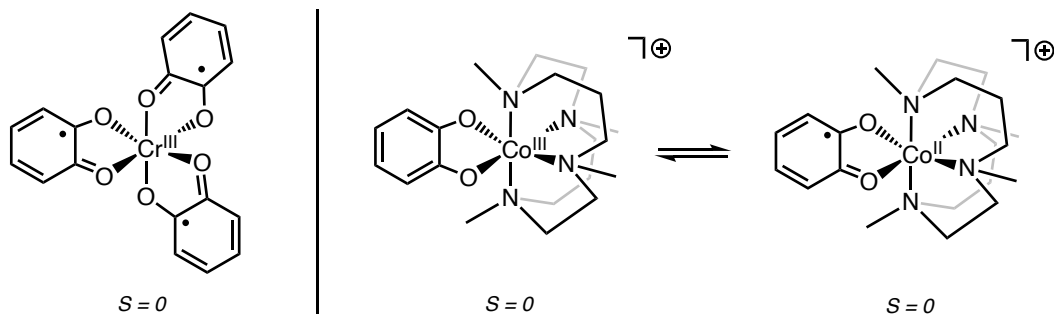
Single-crystal X-ray diffraction is a powerful technique for characterizing coordination complexes with redox-active catecholate-type ligands. Intra-ligand bond distances tend to be sensitive to the oxidation state of the ligand, and as such, high-resolution single-crystal X-ray diffraction experiments are an essential step in diagnosing ligand oxidation state.[26–29] Carbon-oxygen bond distances are approximately 1.34 Å in catecholates and contract upon oxidation to the semiquinonate form (1.30 Å) and to the quinone form (1.22 Å). In *ortho*-amidophenolate and bis(azanido) ligands, the N–C bonds follow a similar trend, decreasing from 1.38 to 1.35 and 1.31 Å as the ligand is oxidized. For the sulfur analogues, benzene-1,2-dithiolates, the S–C bonds tend to decrease from 1.76 to 1.72 Å upon ligand oxidation. Due to the low tendency to form S–C double bonds, dithiolate-type ligands are limited to two oxidation states. The C–C bond distances in the ligand backbone are also informative, as localization of the C=C double bonds becomes pronounced as the ligand is oxidized. Brown has used structural data for many catechol- and *ortho*-aminophenol-derived ligands to develop a metrical oxidation state (MOS), which allows for the calculation of an empirical ligand oxidation state from high-resolution structural data.[30]

Understanding the nature of metal-ligand interactions is highly informative when designing complexes for targeted reactivity. Through in-depth analysis of electronic structure of coordination complexes with redox-active ligands, the ability to assign ligand and metal oxidation states can be

used as a tool to tune these complexes for various applications. For example, traditionally, it is thought that early transition metal imido complexes with highly polarized metal-imido bonds can facilitate C–H bond activation,[31–33] while late transition metal imido complexes tend to undergo C–H bond amination.[34–36] An important determinant is the loci of electron density in a transition metal imido complex, which can facilitate predicting whether the complex is expected to undergo C–H bond activation or C–H bond amination. It was shown that through the incorporation of a redox-active ligand, the bis(2-isopropylamido-4-methoxyphenyl)amide ligand, an early transition metal imido complex could participate in atypical catalytic nitrene transfer reactivity.[37] The accessible redox potentials of redox-active ligands prime their coordination complexes to store and donate electrons for stoichiometric and catalytic reactivity. More recently, in addition to storing electrons, the basic amine groups on redox-active ligands have been explored for their ability to store and donate protons in proton coupled electron transfer (PCET) processes.[38–42]

1.3 Proton-Coupled Electron Transfer

The term PCET was first coined in 1981 to describe the transfer of electrons and protons *together* in the comproportionation shown in **Scheme 1.4** of $[Ru^{IV}(bpy)_2(py)(O)]^{2+}$ and $[Ru^{II}(bpy)_2(py)(OH_2)]^{2+}$.[43] Here, one electron and one proton are transferred simultaneously from the aqua species to the oxo species to afford two hydroxide complexes $[Ru^{III}(bpy)_2(py)(OH)]^{2+}$.

Scheme 1.4. Proton-coupled electron transfer in the comproportionation reaction between $[Ru(bpy)_2(py)(O)]^{2+}$ and $[Ru(bpy)_2(py)(OH_2)]^{2+}$. Scheme adapted from reference 31.
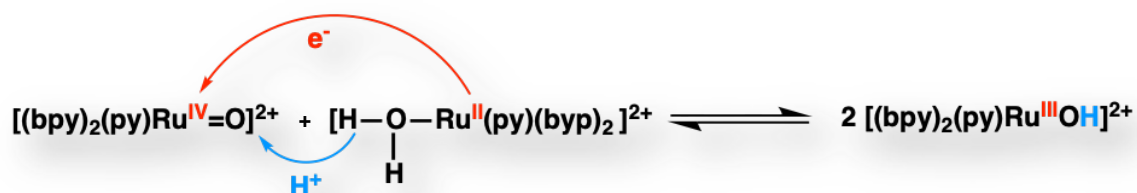
The field has grown significantly since then, and nomenclature has become loosely defined.[44–48] For the sake of this dissertation, nomenclature will be defined here. When the proton and electron are transferred in a single kinetic step, PCET is used. For separate steps of electron and proton transfer, the terms PT-ET or ET-PT are used. There are significant grey areas when exploring transfer mechanisms as one step may precede the other. Inasmuch the term asynchronous is gaining attention to provide a numerical value for the deviation from a fully concerted mechanism towards PT-ET or ET-PT.[49,50] Without deep mechanistic detail, the net transfer of one electron and one proton will be described herein as H-atom transfer (HAT) and the transfer of two electrons and one proton as hydride transfer.

Another layer of naming complexity is added when closely examining the orbitals involved in PCET. If the electron and protons are transferred from different orbitals on the donor to different orbitals on the accepter, the term EPT, electron-proton transfer, is employed. During EPT, the donor orbitals interact electronically with the acceptor orbitals, allowing for simultaneous transfer, occurring on the timescale of coupled vibrations (femtoseconds) and solvent modes (~1 picosecond). When both transfers originate from the same orbital, the term HAT is preferred. It should be noted that it is accepted that the H-atom should originate in the same bond but does not have to be transferred to the same bond in the acceptor. A classic example of PCET in biology is the hydrogen atom abstraction of the mechanistic intermediate compound I in cytochrome P450;

where the source of the H-atom is a C–H bond of a substrate molecule and the proton is transferred to the oxygen of the ferryl group (Fe=O), and the electron is transferred to the porphyrin radical cation.[51] Other terms used in literature are concerted proton-electron transfer (CPET), and concerted electron-proton transfer (CEP), all eluding to the same elementary reactions of an electron transfer coupled to a proton transfer. Additionally, when a proton and electron are transferred in the same step but to different acceptors or originate from different donors but are transferred to a single acceptor, the term multi-site electron-proton transfer (MS-EPT) is used.

From a mechanistic perspective, the multistep separate ET–PT or PT–ET processes are feasible; however, to avoid high energy intermediates, it is energetically favorable to follow a single step. Depictions of the stepwise processes are represented in **Scheme 1.5** as a thermodynamic square scheme where the proton transfer step is represented by the horizontal arrow and the electron transfer by the vertical arrows, and the coupled process by the diagonal arrow.

Scheme 1.5. Thermodynamic cycle of a HAT system.
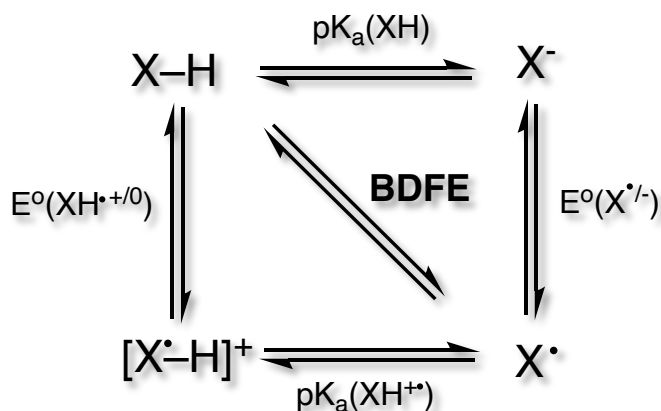
State values such as reduction potential and pK_a can be used as quantitative measurements of the ability to perform the electron and proton transfers, respectively. The diagonal values can also be directly obtained as a measure of the X–H bond strength either as the bond dissociation free energy

(BDFE or $\Delta G_{H\bullet}$) for one electron and one proton, or hydricity (ΔG_{H-}) for two electrons and one proton. To measure BDFE or hydricity of an X–H bond directly, the equilibrium constant (K_{eq}) from reaction with a known HAT or hydride transfer reagent such as TEMPO• or trityl cation must be determined.

Bordwell formulated an equation using Hess' Law and bond enthalpies to calculate the BDE by summing the half-reactions for ET and PT.[52] Equations for the ET (eq. 1.1), and PT (eq. 1.2) processes are shown below where n is the number of electrons, F is the Faraday constant, R is the gas constant, and T is the temperature.

$$\Delta G^{\circ}_{ET} = -nFE^{\circ} \qquad (1.1)$$

$$\Delta G^{\circ}_{PT} = -RTln(K_a) \qquad (1.2)$$

This method was analyzed in more detail later by Parker and Tilset to account for potential errors and assumptions.[53] Equation 1.3 uses a constant C_g value that is solvent dependent and accounts for the reduction potential of a proton $\Delta G_{solv}{}^{\circ}(H\bullet)$, and reaction entropies.[54]

$$BDFE_{sol}(X-H) = 1.37pK_a + 23.06E^{\circ} + C_{g,sol} \qquad (1.3)$$

When adding a second electron for hydride transfer, there are further considerations. First is the source of the electrons, and if they are transferred together in a $X^{2+/0}$ process or at separate potentials, $X^{2+/1+}$ followed by $X^{1+/0}$. If the electrons are transferred at the same potential, n = 2 in Equation 1.1 and the reduction potential for the two-electron process can be used as E° as shown in Equation 1.4. When the ET occurs are different potentials, n = 1 in Equation 1.1, and separate $E_1{}^{\circ}$ and $E_2{}^{\circ}$ values are used as shown in Equation 1.5 below.[55,56] The other major difference between the hydricity and BDFE equations is the $C_{g,sol}$ value. For BDFE, this value refers to the reduction potential of a proton, while for a hydride transfer, this value is the two-electron reduction potential of a proton ($\Delta G^{\circ}_{H+/H-}$).

$$\Delta G^\circ_{H-} = 1.37(pK_a) + 46.12E^\circ + \Delta G^\circ_{H+/H-} \qquad (1.4)$$
$$\text{or}$$
$$\Delta G^\circ_{H-} = 1.37(pK_a) + 23.06E_1^\circ + 23.06E_2^\circ + \Delta G^\circ_{H+/H-} \qquad (1.5)$$

With the ability to understand and control the thermodynamic contributors for PCET, stoichiometric and catalytic processes can be optimized for maximum yield and efficiency. Three main types of coordination complexes are seen in PCET reactivity schemes with various sources for the protons and electron(s). The first type consists of single-site reactions, most typically represented by metal-hydrides where the proton and electron(s) are sourced from the metal-hydride unit. The second type is considered an MS-EPT reaction, where the electrons are sourced from the metal and the protons from a coordinated ligand, often a pendent amine. The third and most underdeveloped type consists of coordination complexes where both the protons and electrons are sourced from the ligand. This third type offers the most tunability with strategic ligand design by incorporating electron withdrawing or donating groups, adding sterics or altering donor atoms. Additionally, judicial metal choice can affect the thermodynamics of the ligand centered ET and PT processes through enhanced metal-ligand interactions.

1.4 Nitrene Transfer in Late Transition-Metal Complexes

Understanding electronic structure is a crucial aspect of understanding how to control the reactivity of transition metal complexes. Ligand-field theory and symmetry arguments provide the foundation for complex design and creating reactivity profiles. These arguments are used to explain the limitations in metal-ligand multiple bonds and the *oxo wall*.[57,58] It is well-established that metal-ligand multiple bonds are efficient ways of activating C–H bonds in both synthetic and biological systems. Metal-ligand multiple bonds can also effect such transformations as olefin epoxidation and aziridination and the proton and electron transfer processes related to nitrogen fixation. The frontier molecular orbital depiction that describes the metal-ligand multiple bond for

a metal–oxo complex with C_{4v} symmetry is shown in **Figure 1.2**. It has been shown that manipulation of metal-oxo / imido complex geometry can result in enhanced reactivity that is traditionally viewed as forbidden.[59–67] In such cases, access to the metal-ligand multiple-bond is achieved when the metal-ligand π^* orbitals are vacant or partially filled. There have been several pathways implored to design complexes that satisfy this criterion. The first and most familiar is to keep the d-electron count low. In the prototypical C_{4v} metal complex with one terminal multiply bonded ligand, the antibonding orbitals from the π interaction are metal based. As the number of d electrons increases, the bond order and thus the stability of the multiple bond decreases. This approach is not limited to four-fold symmetry but is used in trigonal bipyramidal and tetrahedral geometries as well. The second pathway to achieve metal-ligand multiple bond stability is employing ligands that are σ donating and π accepting. This method invokes orbital mixing that stabilizes d-electrons that are otherwise destabilized by the π^* interactions. The third method used to achieve metal-ligand multiple bonds is to remove donor ligands from the metal center to create a distinct electronic structure that can accommodate a high number of electrons. This is commonly seen in complexes with three-fold symmetry with four and five-coordinate geometries.
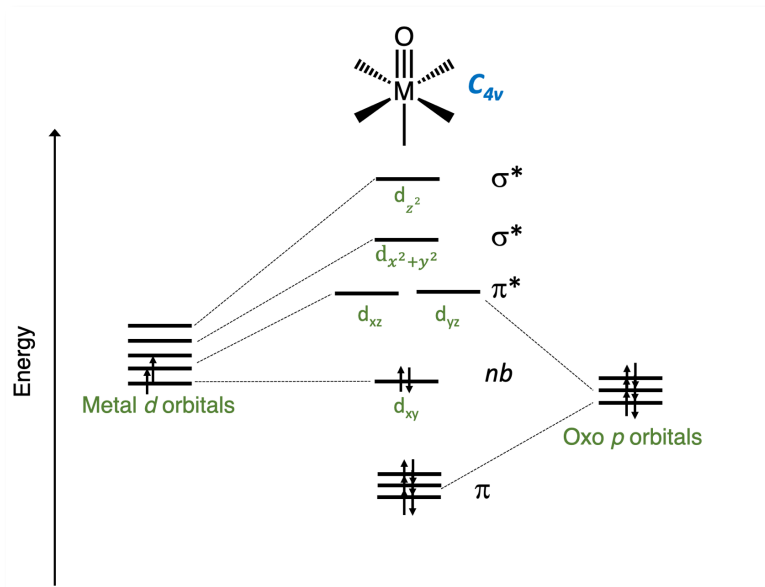
Figure 1.2. Frontier molecular orbital diagram for a C_{4v} d^2 transition metal oxo.

Examples by the Bergman group have shown the ability to isolate an iridium (III) d^6-imido and an iridium (IV) d^4-oxo by invoking a *pseudo*-tetrahedral geometry that puts the d-electrons in mainly non-bonding orbitals which are orthogonal to the Ir–O bond vector leaving the π^* orbitals unfilled.[68] Mid to late first-row transition metals have also received attention as oxo and nitrene transfer reagents with plenty of examples Fe, and a few with Mn and Co; however, examples of imido, imnyl, or nitrene complexes with nickel are more scarce.[61,62,65,67,69] Of the reported species, both methods two and three have been invoked to achieve metal-ligand multiple bonds with nickel as imides, phosphinidenes, and carbenes. Many of these systems owe their stability to electronic stabilization from their trigonal planar and *pseud*o-tetrahedral geometries and large steric bulk positioned to protect the metal-ligand multiple bond unit. These species are also stabilized by such ligands such as dipyrrinato that provide structural rigidity through chelation to enforce a low coordinate geometry.[70,71]
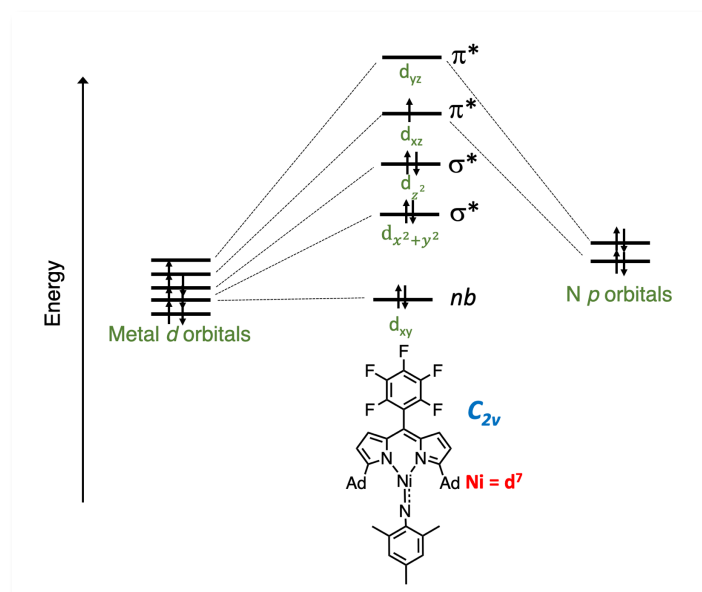
Figure 1.3. Frontier molecular orbital diagram for C_{2v} d^7 nickel iminyl.

Figure 1.3 shows the frontier orbital diagram for a d^7 nickel iminyl with C_{2v} symmetry developed by Betley.[70,71] It is hypothesized that by incorporating a redox-active ligand into the electronic structure of a nickel-nitrene, the empty π-system of the redox-active ligand can alleviate electron density in an otherwise unfavourable bonding interaction, thus facilitating a new mechanism in forming a late-transition metal-ligand multiple bond. This frontier orbital diagram for such a system is shown in **Figure 1.4**. This new metal-ligand bonding interaction would allow access to reactivity not typically observed in late transition metal imido complexes similar to the those mentioned in Section 1.2.
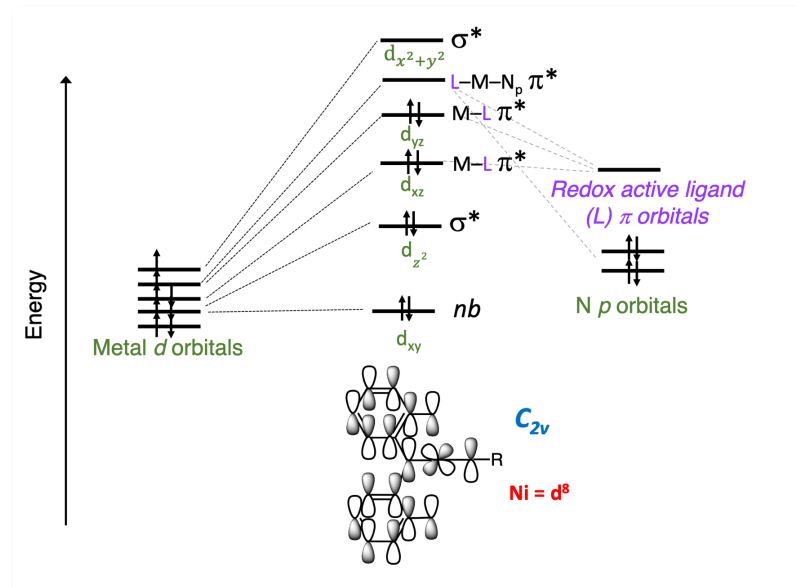
Figure 1.4. Frontier molecular orbital diagram for C_{2v} d^8 nickel iminyl with a redox-active ligand.

1.5 Contributions of This Work

The work presented in this dissertation focuses on understanding the intricacies of metal-ligand bonding and its effect on chemical reactivity. Specifically, how the incorporation of redox-active ligands in transition metal complexes allows for a tunable and systematic dissection of these properties. In addition to electronic modifications to the organic framework, a more nascent modification utilizes a basic site on the ligand backbone. By protonating the redox-active ligand, a new type of reactivity can be considered in addition to traditional electron-transfer processes such as oxidative addition and reductive elimination. *Chapter 2* explores the thermodynamic and kinetic contributions involved in transferring one proton and one electron, nominally an H-atom, when the organic framework, a protonated tridentate redox-active SNS ligand, remains unchanged and the metal center is varied. Understanding the influence of metal center on ligand-centered HAT allowed for further metal variance and tuning within the ligand framework to further enhance PCET reactivity. *Chapter 3* discusses the same proton and redox non-innocent ligand framework

with a different metal center and auxiliary ligand. Changing the metal center facilitated a change in coordination geometry and access to HAT along with nitrene transfer. Here, the fully reduced, protonated ligand [SN(H)S] is bound to a cobalt metal center with two dimethylaminopyridine (dmap) ligands in a *pseudo*-tetrahedral coordination geometry. Reactivity studies reveal the transformation of *p*-tolylazide into *p*-toluidine with mechanistic insights suggesting two H-atom transfers facilitating the nitrene transfer. Further modifications were made to the tridentate ligand framework in *Chapter 4*. Here the soft donor atoms were replaced with hard donor oxygens in the previously reported [ON(H)O] framework. When bound to nickel with triphenylphosphine as the auxiliary ligand, this ligand has the potential to serve as not only an H-atom transfer source but also has the ability to store an additional electron and serve as a modest hydride donor. The reactivity studies performed with this complex revealed higher coordinate nickel products with unique properties, which provided deeper insights into the intricate nature of the metal-ligand bonds. Lastly, *Chapter 5* describes the catalytic nitrene transfer capabilities and limitations of this ONO-Ni system. This work explores the specific bonding interactions required to facilitate nitrene transfer in late-transition metal complexes. Nitrene transfer and metal-ligand multiple bonds are rare in late-transition metal complexes due to their higher energy filled d-orbitals, however, strategic geometry-controlled electronic structures with nickel have been previously employed to overcome this limitation. The approach applied in this work uses the symmetry allowed metal-ligand interactions to transfer electron density when needed to facilitate nitrene transfer in a nickel system.

1.6 References

1   S. Y. Reece, J. A. Hamel, K. Sung, T. D. Jarvi, A. J. Esswein, J. J. H. Pijpers and D. G. Nocera, *Science* 2011, **334**, 645–648.

2   M. W. Kanan and D. G. Nocera, *Science* 2008, **321**, 1072–1075.

3   A. Fujishima and K. Honda, *Nature*, 1972, **238**, 37–38.

4   J. W. Youngblood, S. H. A. Lee, Y. Kobayashi, E. A. Hernandez-Pagan, P. G. Hoertz, T. A. Moore, A. L. Moore, D. Gust and T. E. Mallouk, *J. Am. Chem. Soc.*, 2009, **131**, 926–927.

5   K. N. Ferreira, T. M. Iverson, K. Maghlaoui, J. Barber and S. Iwata, *Science* 2004, **303**, 1831–1838.

6   J. P. McEvoy and G. W. Brudvig, *Chem. Rev.*, 2006, 106, 4455–4483.

7   Y. Umena, K. Kawakami, J. R. Shen and N. Kamiya, *Nature*, 2011, **473**, 55–60.

8   B. Loll, J. Kern, W. Saenger, A. Zouni and J. Biesiadka, *Nature*, 2005, **438**, 1040–1044.

9   N. Cox, D. A. Pantazis, F. Neese and W. Lubitz, *Acc. Chem. Res.*, 2013, **46**, 1588–1596.

10   S. Groysman and R. H. Holm, *Biochemistry*, 2009, **48**, 2310–2320.

11   E. A. Hill, A. C. Weitz, E. Onderko, A. Romero-Rivera, Y. Guo, M. Swart, E. L. Bominaar, M. T. Green, M. P. Hendrich, D. C. Lacy and A. S. Borovik, *J. Am. Chem. Soc.*, 2016, **138**, 13143–13146.

12   S. Wang, A. Aster, M. Mirmohades, R. Lomoth and L. Hammarström, *Inorg. Chem.*, 2018, **57**, 768–776.

13   T. Zhang, C. Wang, S. Liu, J. L. Wang and W. Lin, *J. Am. Chem. Soc.*, 2014, **136**, 273–281.

14   C. K. Jørgensen, *Coord. Chem. Rev.*, 1966, **1**, 164–178.

15   J. H. Enemark and R. D. Feltham, *Coord. Chem. Rev.*, 1974, **13**, 339–406.

16   M. Melnik, W. Liu, A. B. P. Lever, P. R. Auburn, E. S. Dodsworth, M. A. Haga and W. A. Nevin, *J. Am. Chem. Soc.*, 1988, **110**, 8076–8084.

17   A. B. P. Lever, H. Masui, R. A. Metcalfe, D. J. Stufkens, E. S. Dodsworth and P. R. Auburn, *Coord. Chem. Rev.*, 1993, **125**, 317–331.

18   M.-A. Haga, E. S. Dodsworth and A. B. P. Lever, *Inorg. Chem*, 1986, **25**, 447–453.

19   R. R. Kapre, E. Bothe, T. Weyhermüller, S. D. B. George, N. Muresan and K. Wieghardt, *Inorg. Chem.*, 2007, **46**, 7827–7839.

20   M. Haga, E. S. Dodsworth, A. B. Lever, S. R. Boone and C. G. Pierpont, *J. Am. Chem. Soc.*, 1986, **108**, 7413–7414.

21   J. Rall and W. Kaim, *J. Chem. Soc. Faraday Trans.*, 1994, **90**, 2905–2908.

22   K. Chłopek, E. Bothe, F. Neese, T. Weyhermuller and K. Wieghardt, *Inorg. Chem.*, 2006, **45**, 6298–6307.

23   K. Ray, T. Weyhermüller, F. Neese and K. Wieghardt, *Inorg. Chem.*, 2005, **44**, 5345–5360.

24   C. G. Pierpont, *Inorg. Chem.*, 2001, **40**, 5727–5728.

25   A. Caneschi, A. Dei, D. Gatteschi and V. Tangoulis, *Inorg. Chem.*, 2002, **41**, 3508–3512.

26   C. G. Pierpont and R. M. Buchanan, *Coord. Chem. Rev.*, 1981, **38**, 45–87.

27   P. Chaudhuri, C. N. Verani, B. Eckhard, B. Eberhard, T. Weyhermüller, K. Wieghardt, C. Nazari Verani, E. Bill, E. Bothe, T. Weyhermüller and K. Wieghardt, *J. Am. Chem. Soc.*, 2001, **123**, 2213–2223.

28   E. Bill, E. Bothe, P. Chaudhuri, K. Chlopek, D. Herebian, S. Kokatam, K. Ray, T. Weyhermüller, F. Neese and K. Wieghardt, *Chem. - A Eur. J.*, 2005, **11**, 204–224.

29   O. Carugo, *Inorganica Chim. Acta*, 1994, **215**, 219–223.

30   S. N. Brown, *Inorg. Chem.*, 2012, **51**, 1251–1260.

31   H. M. Hoyt and R. G. Bergman, *Angew. Chemie - Int. Ed.*, 2007, **46**, 5580–5582.

32   C. P. Schaller, C. C. Cummins and P. T. Wolczanski, *J. Am. Chem. Soc*, 1996, **118**, 591–611.

33   L. M. Slaughter, P. T. Wolczanski, T. R. Klinckman and T. R. Cundari, *J. Am. Chem. Soc.*, 2000, **122**, 7953–7975.

34   E. R. King and T. A. Betley, *Inorg. Chem.*, 2009, **48**, 2361–2363.

35   Y. M. Badiei, A. Dinescu, X. Dai, R. M. Palomino, F. W. Heinemann, T. R. Cundari and T. H. Warren, *Angew. Chemie - Int. Ed.*, 2008, **47**, 9961–9964.

36   H. Y. Thu, W. Y. Yu and C. M. Che, *J. Am. Chem. Soc.*, 2006, **128**, 9048–9049.

37   A. I. Nguyen, R. A. Zarkesh, D. C. Lacy, M. K. Thorson and A. F. Heyduk, *Chem. Sci.*, 2011, **2**, 166–189.

38   K. M. Waldie, S. Ramakrishnan, S.-K. Kim, J. K. Maclaren, C. E. D. Chidsey and R. M. Waymouth, *J. Am. Chem. Soc.*, 2017, **139**, 4540–4550.

39   E. A. McLoughlin, K. M. Waldie, S. Ramakrishnan and R. M. Waymouth, *J. Am. Chem. Soc.*, 2018, **140**, 13233–13241.

40   F. Lu, R. A. Zarkesh and A. F. Heyduk, *Eur. J. Inorg. Chem.*, 2012, 467–470.

41   L. A. Berben, *Chem. – A Eur. J.*, 2015, **21**, 2734–2742.

42   E. J. Thompson and L. A. Berben, *Angew. Chemie Int. Ed.*, 2015, **54**, 11642–11646.

43   R. A. Binstead, B. A. Moyer, G. J. Samuels and T. J. Meyer, *J. Am. Chem. Soc.*, 1981, **103**, 2897–2899.

44   J. W. Darcy, B. Koronkiewicz, G. A. Parada and J. M. Mayer, *Acc. Chem. Res.*, 2018, **51**, 2391–2399.

45   J. M. Mayer, *Acc. Chem. Res.*, 2011, **44**, 36–46.

46   S. Hammes-Schiffer, *J. Am. Chem. Soc.*, 2015, **137**, 8860–8871.

47   R. Tyburski, T. Liu, S. D. Glover and L. Hammarström, *J. Am. Chem. Soc.*, 2021, **143**, 560–576.

48   R. I. Cukier and D. G. Nocera, *Annu. Rev. Phys. Chem.*, 1998, **49**, 337–369.

49   D. Bím, M. Maldonado-Domínguez, L. Rulísek and M. Srnec, *Proc. Natl. Acad. Sci. U. S. A.*, 2018, **115**, E10287–E10294.

50   M. K. Goetz and J. S. Anderson, *J. Am. Chem. Soc.*, 2019, **141**, 4051–4062.

51   J. Rittle, J. M. Younker and M. T. Green, *Inorg. Chem.*, 2010, **49**, 3610–3617.

52   F. G. Bordwell, J. P. Cheng and J. A. Harrelson, *J. Am. Chem. Soc.*, 1988, **110**, 1229–1231.

53   M. Tilset and V. D. Parker, *J. Am. Chem. Soc.*, 1989, **111**, 6711–6717.

54   J. J. Warren, T. A. Tronic and J. M. Mayer, *Chem. Rev.*, 2010, **110**, 6961–7001.

55   E. S. Wiedner, M. B. Chambers, C. L. Pitman, R. M. Bullock, A. J. M. Miller and A. M. Appel, *Chem. Rev.*, 2016, **116**, 8655–8692.

56   A. F. Sasayama, C. P. Kubiak, K. M. Waldie, A. L. Ostericher and M. H. Reineke, *ACS Catal.*, 2018, **8**, 1313–1324.

57   C. J. Ballhausen and H. B. Gray, *Inorg. Chem.*, 1962, **1**, 111–122.

58   V. A. Larson, B. Battistella, K. Ray, N. Lehnert and W. Nam, *Nat. Rev. Chem.*, 2020, **4**, 404–419.

59   B. Wang, Y. M. Lee, W. Y. Tcho, S. Tussupbayev, S. T. Kim, Y. Kim, M. S. Seo, K. Bin Cho, Y. Dede, B. C. Keegan, T. Ogura, S. H. Kim, T. Ohta, M. H. Baik, K. Ray, J. Shearer and W. Nam, *Nat. Commun.*, 2017, **8**, 14839.

60   F. Felix Pfaff, F. Heims, S. Kundu, S. Mebs and K. Ray, *Chem. Commun.*, 2012, **48**, 3730–3732.

61   Y. Dong, J. T. Lukens, R. M. Clarke, S. L. Zheng, K. M. Lancaster and T. A. Betley, *Chem. Sci.*, 2020, **11**, 1260–1268.

62   C. E. MacBeth, J. C. Thomas, T. A. Betley and J. C. Peters, *Inorg. Chem.*, 2004, **43**, 4645–4662.

63   Y. Baek, E. T. Hennessy and T. A. Betley, *J. Am. Chem. Soc*, 2019, **141**, 16944–16953.

64   K. M. Carsch, I. M. DiMucci, D. A. Iovan, A. Li, S. L. Zheng, C. J. Titus, S. J. Lee, K. D. Irwin, D. Nordlund, K. M. Lancaster and T. A. Betley, *Science*, 2019, **365**, 1138–1143.

65   E. Kogut, H. L. Wiencko, L. Zhang, D. E. Cordeau and T. H. Warren, *J. Am. Chem. Soc.*, 2005, **127**, 11248–11249.

66   P. Sarkar, A. Sarmah and C. Mukherjee, *Chem. Commun.*, 2021, **57**, 1352–1355.

67   D. J. Mindiola and G. L. Hillhouse, *J. Am. Chem. Soc.*, 2001, **123**, 4623–4624.

68   D. S. Glueck, J. Wu, F. J. Hollander and R. G. Bergman, *J. Am. Chem. Soc.*, 1991, **113**, 2041–2054.

69   C. A. Laskowski and G. L. Hillhouse, *Organometallics*, 2009, **28**, 6114–6120.

70   Y. Dong, C. J. Lund, G. J. Porter, R. M. Clarke, S.-L. L. Zheng, T. R. Cundari and T. A. Betley, *J. Am. Chem. Soc.*, 2021, **143**, 817–829.

71   Y. Dong, R. M. Clarke, G. J. Porter and T. A. Betley, *J. Am. Chem. Soc.*, 2020, **142**, 10996–11005.

Chapter 2

Metal Ion Influence on Ligand-Centered Hydrogen Atom Transfer

2.1 Introduction

Tuning the thermodynamics of hydrogen atom transfer (HAT) reagents is critical to the development of new catalysts for multi-electron, multi-proton processes. Such processes are relevant in both chemical and biological reactions, such as C–H oxidation in cytochrome P450 for drug metabolism.[1] The ability to control the factors that govern these transformations would allow for the design of systems with enhanced reactivity. For coordination complexes, HAT reactivity (and more broadly proton-coupled electron transfer) generally fall into two types: single-site and multisite electron-proton transfer (MS-EPT) reactions. Single-site reactions are exemplified by metal hydride complexes, in which the metal-hydride unit is the source of both the proton and the electron during HAT.[2–5] In MS-EPT reactions, the electron and proton associated with the HAT originate at different loci; typically, the metal center serves as the source of the electron while a coordinated ligand serves as the source of the proton.[6–9] Recent attention has been drawn to a third type of HAT reactivity in coordination complexes, ligand-centered HAT, in which a ligand serves as the source of both electron and proton.[10–18]

Considerable effort has been devoted to understanding how various factors govern the thermodynamics and kinetics of HAT reactions in transition metal complexes.[19–21] The thermodynamics are often partitioned between redox and pK_a factors. For example, previous studies on single-site HAT revealed that changing the metal ion within a series of isoelectronic metal hydrides had a notable effect on the pK_a values across the series.[3,4,22,23] Whereas, tuning the ligand environment through steric changes or by the addition of electron-donating/withdrawing groups had a more dramatic effect on the reduction potential.[9,22,24] While often tuned independently, these thermodynamic factors are difficult to control simultaneously as tuning one is often compensated for by the effects of the other, leading to a net cancellation of their anticipated

effect on BDFE. These correlations have been made on the traditional single-site transition metal hydrides and multi-site transition metal complexes mentioned above; however, less work has been devoted to studying these effects in ligand-centered HAT when the electron and proton both reside on the ligand backbone.[14]

This Chapter presents the thermodynamics and kinetics of ligand-centered HAT reactivity in a family of coordination complexes containing the tridentate pincer ligand derived from bis(2-mercapto-p-tolyl)amine, [SNS]H$_3$. Herein, the synthesis and characterization of [SN(H)S]M(PPh$_3$), K(THF){[SNS^{cat}]M(PPh$_3$)}, and [SNS$^\bullet$]M(PPh$_3$) (M = Pd, Pt) complexes are described. These complexes are isostructural and isoelectronic with the nickel derivatives that have been reported previously.[10] Electrochemical, spectroscopic, and equilibrium HAT measurements were used to evaluate the thermodynamics of HAT across the nickel, palladium, and platinum series and to examine how the measured BDFEs partition into redox and pK_a effects. Isotope effects and activation parameters have been measured for complexes of all three metals to determine the kinetic factors that govern HAT reactivity and how the metal ion influences these factors.

2.2 Results

2.2.1 Synthesis and structural characterization

The synthetic routes used to obtain new palladium and platinum complexes of the proligand bis(2-mercapto-*p*-tolyl)amine, [SNS]H$_3$, are summarized in **Scheme 2.1**. These synthetic methods follow the routes previously reported for the analogous nickel complexes.[10] For all six new complexes, empirical formulation was confirmed by electrospray ionization mass spectrometry (ESI), and bulk composition was verified by elemental analysis. The diamagnetic complexes [SN(H)S]M(PPh$_3$) and K(THF){[SNS^{cat}]M(PPh$_3$)} (M = Pd, Pt) were readily characterized by multinuclear NMR spectroscopy in solution, with the spectra for each complex conforming to nominal C_s and C_{2v} symmetries, respectively. The ^{1}H NMR spectrum of K(THF){[SNS^{cat}]Pd(PPh$_3$)} was characterized by broad signals; however, the analogous [Et$_3$NH] {[SNS^{cat}]Pd(PPh$_3$)} derivative afforded sharp ^{1}H NMR resonances. For the [SN(H)S]M(PPh$_3$) derivatives, the ^{1}H NMR spectra were distinguished by broad, down-field resonances for the N–H protons at 9.23, 10.03, and 10.52 ppm for the nickel, palladium, and platinum complexes, respectively.

Scheme 2.1. Synthesis of [SN(H)S]M(PPh₃), K(THF){[SNSᶜᵃᵗ]M(PPh₃)} and [SNS•]M(PPh₃) where M = Pd and Pt.
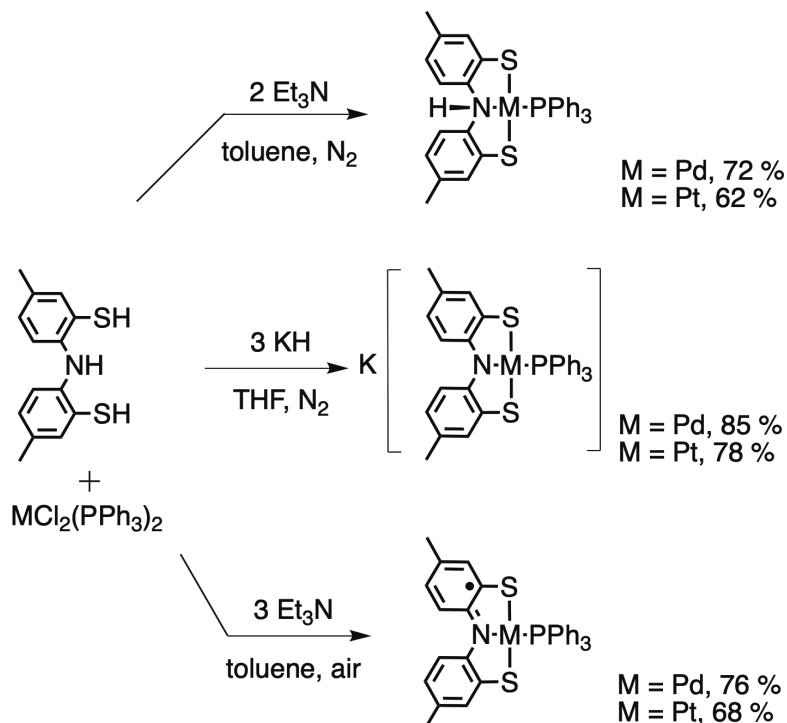
The molecular structures of all new palladium and platinum complexes were determined by single-crystal X-ray diffraction experiments. For the salts, K(THF){[SNSᶜᵃᵗ]M(PPh₃)}, single crystals were obtained by slow diffusion of pentane into concentrated THF solutions of the salt in the presence of 2.2.2-cryptand at –36 °C. Cryptand-containing crystals, K(2.2.2-crypt){[SNSᶜᵃᵗ]M(PPh₃)}, were obtained as purple needles for the palladium derivative and green needles for the platinum derivative. Diffusion of pentane into THF solutions of [SN(H)S]M(PPh₃) at –36 °C under an inert atmosphere afforded single crystals of both the palladium and platinum congeners as orange and green prisms, respectively. In contrast, under aerobic conditions, solutions of [SN(H)S]Pt(PPh₃) in acetonitrile or [SN(H)S]Pd(PPh₃) in ethanol afforded single crystals of [SNS•]Pt(PPh₃) or [SNS•]Pd(PPh₃), respectively. **Figure 2.1** shows the molecular structures of the six new palladium and platinum complexes, [SN(H)S]M(PPh₃), [SNS•]M(PPh₃), and K(2.2.2-crypt){[SNSᶜᵃᵗ]M(PPh₃)}, with uncoordinated solvents and hydrogen atoms excluded

24

for clarity. **Table 2.1** shows select metrical parameters for the six new complexes of palladium and platinum, all of which display square-planar coordination geometry at the metal center with calculated τ_4 values close to zero.[25] Metrical data for the nickel complexes have been previously reported.[10]

Metal-ligand bond distances are notably similar in analogous palladium and platinum structures with M–S, M–N, and M–P bond distances within 0.02 Å of each other, consistent with the similar sizes of palladium(II) and platinum(II) complexes in square-planar environments.[22,26–28] Whereas the ligand nitrogen atom of the [SNS$^\bullet$]M(PPh$_3$) radicals and the {[SNS^{cat}]M(PPh$_3$)}$^{1-}$ anions show clear sp^2 hybridization (sum of angles around N is ~360°), for the [SN(H)S]M(PPh$_3$) complexes, the sum of the heavy-atom angles around nitrogen drops to 344°, consistent with sp^3 hybridization and binding of the proton to the nitrogen atom. In comparing the structures of the [SNS$^\bullet$]M(PPh$_3$) radicals and the {[SNS^{cat}]M(PPh$_3$)}$^{1-}$ anions for both palladium and platinum, the N–C and S–C bond distances elongate by approximately 0.02 Å upon reduction of the ligand; whereas, the M–N bond distances contract by 0.02 Å. Ligand reduction in both the palladium and platinum derivatives results in changes to the M–S bond distances that are less than 0.01 Å. Changes to the protonation state of the ligand also manifest changes in metrical parameters that are consistent across both palladium and platinum derivatives. Notably, the M–N and N–C bonds elongate by more than 0.06 Å with the addition of the proton that transforms anionic {[SNS^{cat}]M(PPh$_3$)}$^{1-}$ into neutral [SN(H)S]M(PPh$_3$). The [SNS] ligand also appears to be slightly less symmetric in the protonated form, with intra-ligand M–S distances that differ by 0.026 Å, S–C distances that differ by 0.012 Å, and S–M–N bite angles that differ by approximately 2.7°.
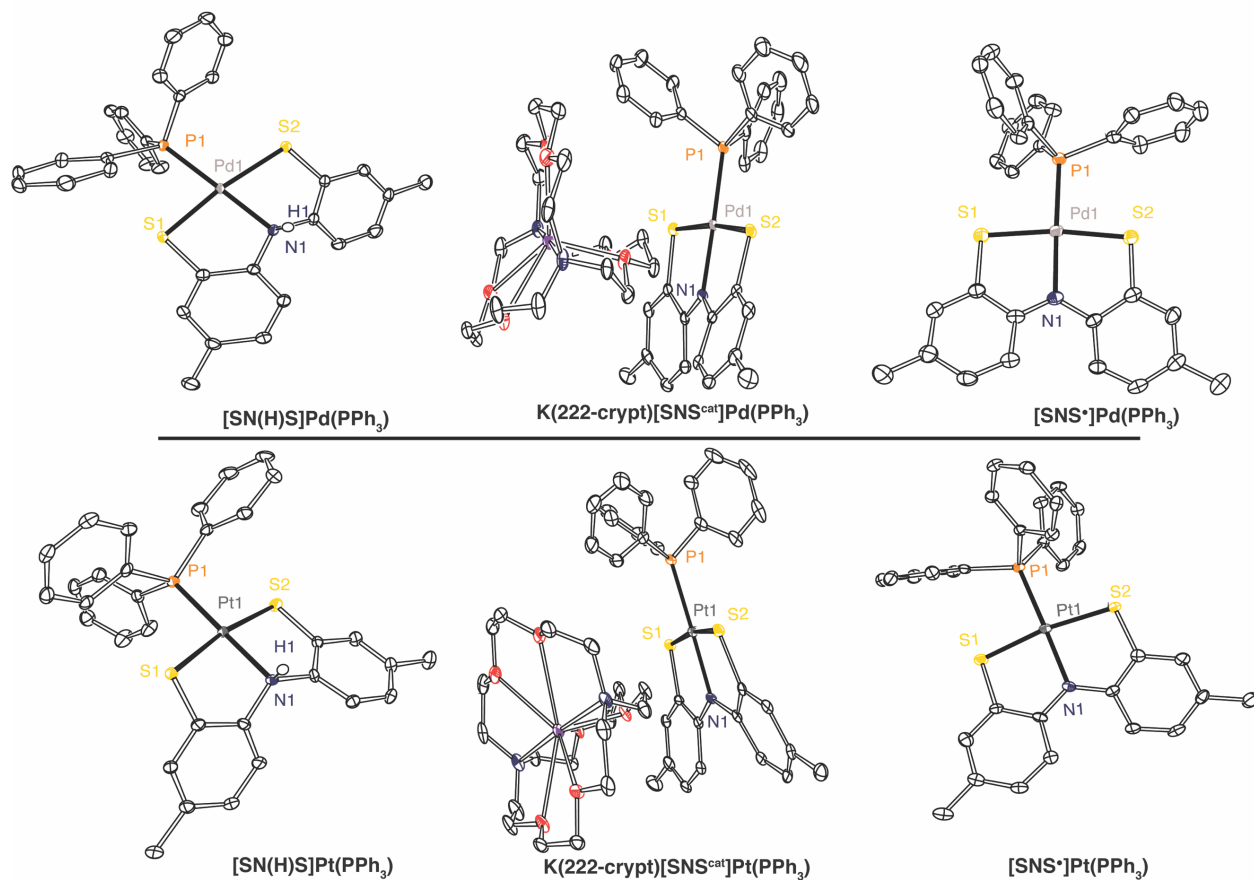
Figure 2.1. Representative ORTEP diagrams for [SN(H)S]M(PPh$_3$) (left), K(2.2.2.-crypt){[SNS^{cat}]M(PPh$_3$)} (middle) and [SNS$^\bullet$]M(PPh$_3$) (right) where M = Pd (top) and Pt (bottom) with thermal ellipsoids shown at 50% probability. Hydrogen atoms and solvent molecules have been omitted for clarity.

Table 2.1. Selected bond distances (Å) and τ_4 values from solid-state structures of [SNS$^\bullet$]M(PPh$_3$), K(2.2.2.-crypt){[SNS^{cat}]M(PPh$_3$)}, and [SN(H)S]M(PPh$_3$) (M = Pd, Pt).

	[SNS$^\bullet$]M(PPh$_3$)			
	K(2.2.2.-crypt){[SNS^{cat}]M(PPh$_3$)}			
	[SN(H)S]M(PPh$_3$)			
	M = Pd		M = Pt	
M–S	2.2878(10)	2.3021(9)	2.2987(16)	2.3074(15)
	2.3052(7)	*2.2898(7)*	*2.3106(19)*	*2.3018(18)*
	2.3136(8)	2.2869(8)	2.3170(9)	2.2906(9)
M–N	2.057(3)		2.065(5)	
	2.036(2)		*2.043(4)*	
	2.100(3)		2.106(3)	
M–P	2.2602(9)		2.2501(15)	
	2.2501(7)		*2.2280(16)*	
	2.2400(8)		2.2266(9)	
C–N	1.379(4)	1.365(5)	1.377(8)	1.394(8)
	1.395(3)	*1.394(3)*	*1.391(6)*	*1.406(6)*
	1.472(4)	1.464(4)	1.483(4)	1.462(4)
C–S	1.745(4)	1.749(4)	1.745(6)	1.757(7)
	1.766(3)	*1.766(3)*	*1.770(5)*	*1.763(5)*
	1.778(3)	1.766(3)	1.776(4)	1.764(4)
$\tau_4{}^a$	0.070		0.075	
	0.075		*0.084*	
	0.073		0.078	

$${}^a\tau_4 = \frac{360° - (\alpha - \beta)}{360° - 2\theta}$$

2.2.2 EPR Spectroscopy

Paramagnetic [SNS•]M(PPh$_3$) (M = Pd, Pt) complexes were readily characterized using X-band electron paramagnetic resonance (EPR) spectroscopy thanks to their $S = \frac{1}{2}$ spin state. **Figure 2.2** shows the X-band EPR spectra for all three [SNS•]M(PPh$_3$) complexes (M = Ni, Pd, Pt) in C$_6$H$_6$ at 77 K. The palladium derivative exhibits an isotropic signal with g = 1.99. The spectra of the nickel and platinum derivatives are different, showing evidence of distortion. The spectrum of the nickel complex appeared rhombic and was simulated with g values of 1.95, 2.00, and 2.05.[29] For the platinum complex, the observed spectrum was simulated as axial with g values of 1.92 and 1.98 and including hyperfine splitting from the [195]Pt nucleus with A([195]Pt) 30 and 200 MHz.
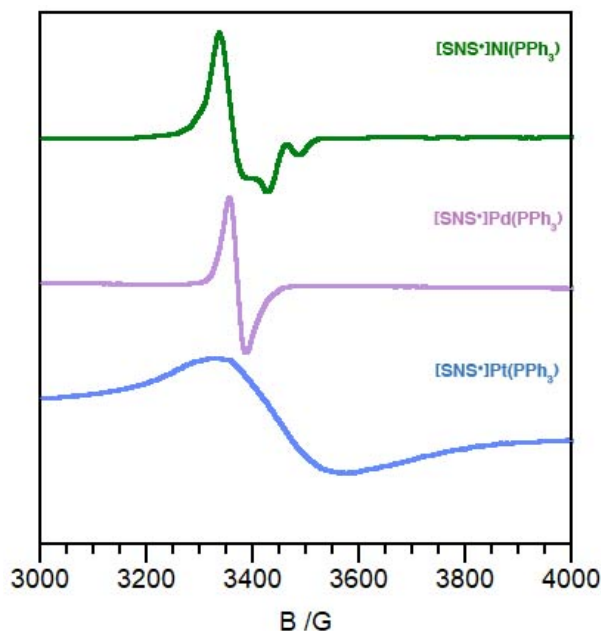
Figure 2.2. Experimental X-band EPR spectra of ligand radical complexes [SNS•]M(PPh$_3$) (M= Ni (top), Pd (middle), Pt (bottom) in C$_6$H$_6$ at 77 K.

2.2.3 Electronic Spectroscopy

The electronic absorbance spectra of the new coordination complexes with different ligand protonation and redox states are readily distinguished in the UV-vis-NIR regions. **Figure 2.3**

shows the electronic absorption spectra for all nine metal complexes [SNS$^\bullet$]M(PPh$_3$) (2.3A), K(THF){[SNS^{cat}]M(PPh$_3$)} (2.3B) and [SN(H)S]M(PPh$_3$) (2.3C) for M = Ni, Pd and Pt; with comparative spectra of all three palladium complexes (2.3D). The calculated extinction coefficients for all nine complexes are reported in **Table 2.2**. The radical [SNS$^\bullet$]M(PPh$_3$) complexes have the most feature-rich absorption spectra with strong absorptions in the near-UV, visible, and near-IR portions of the spectrum. The intense, visible-energy transition characteristic of radical semiquinonate complexes was observed for [SNS$^\bullet$]Pd(PPh$_3$) at 606 nm and red-shifted to 623 nm for [SNS$^\bullet$]Pt(PPh$_3$). The same transition was observed at 663 nm for [SNS$^\bullet$]Ni(PPh$_3$). The K(THF){[SNS^{cat}]M(PPh$_3$)} anions show simpler spectra, dominated by a metal-sensitive absorption in the near-UV, which appeared at 359 nm for the nickel derivative, 356 nm for the palladium derivative, and 348 nm for the platinum derivative. Protonation of the ligand in the [SN(H)S]M(PPh$_3$) derivatives further simplifies the electronic absorption spectra, with only a subtle shoulder visible in the spectrum near 320 nm. The spectra of the protonated [SN(H)S]M(PPh$_3$) complexes for M = Ni and Pt and K(THF){[SNS^{cat}]Pd(PPh$_3$)} show small features resembling the [SNS$^\bullet$]M(PPh$_3$) complexes at low energy owning to the air-sensitive nature of these samples.
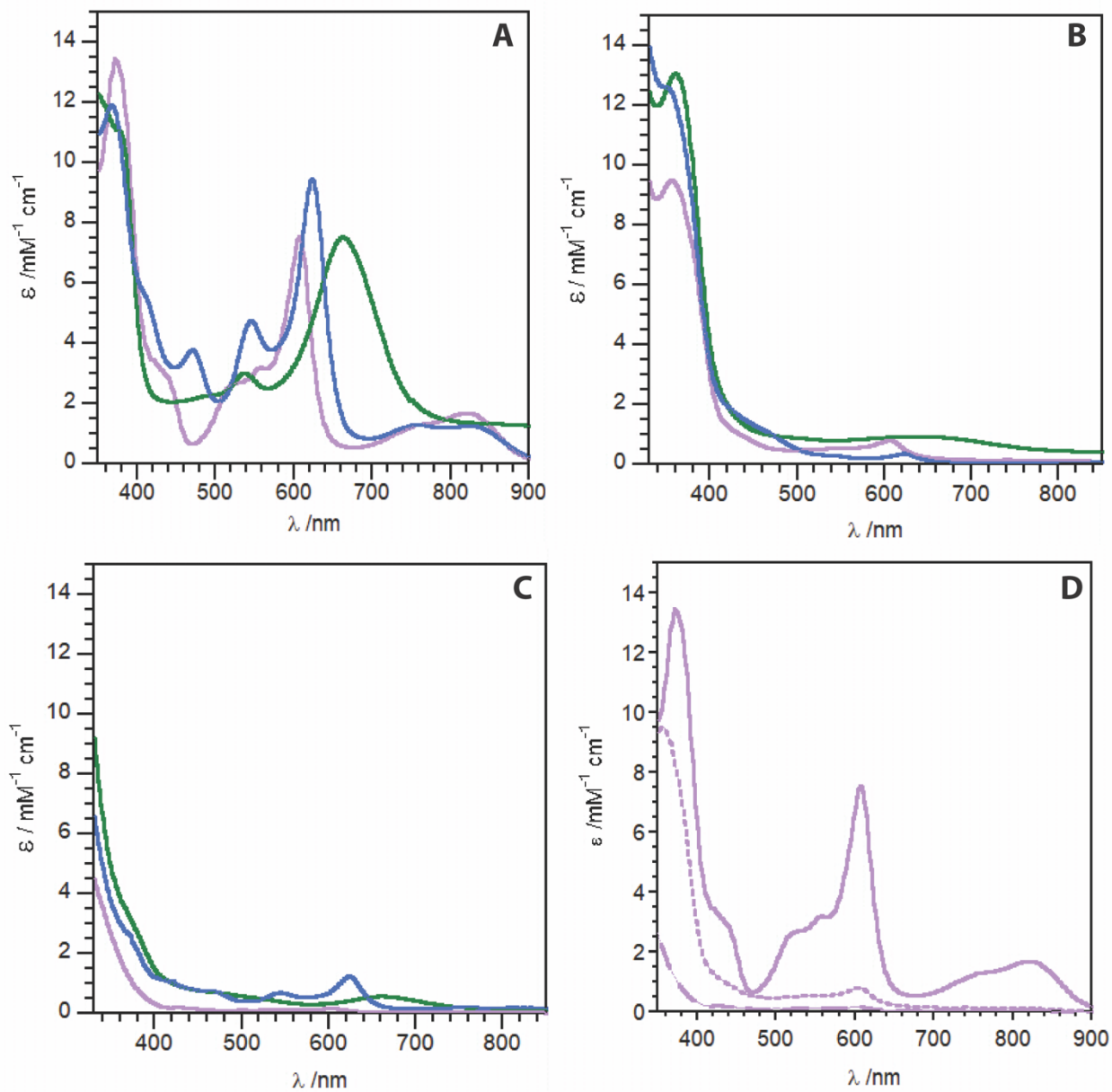
Figure 2.3. Electronic absorption spectra recorded for [SNS•]M(PPh₃) in CH₂Cl₂ (A), K(THF){[SNS^cat]M(PPh₃)} (B) and [SN(H)S]M(PPh₃) (C) in MeCN where M = Ni (green), Pd, (purple), Pt (blue). (D) Comparative electronic absorption spectra of [SNS•]Pd(PPh₃) (——) in CH₂Cl₂, K(THF){[SNS^cat]Pd(PPh₃)} (---) and [SN(H)S]Pd(PPh₃) (– – –) in MeCN.

Table 2.2. Reported λ_{max} (nm) and extinction coefficients (M^{-1} cm^{-1}) for nickel, palladium, and platinum complexes.

	Ni	Pd	Pt
[SNS•]M(PPh$_3$)	376 (11100), 537 (3000), 663 (7500)	372 (13500), 606 (7600), 824 (1700)	368 (11900), 471 (3800), 546 (4800), 623 (9500)
K(THF)[{SNS^{cat}}M(PPh$_3$)]	359 (13000)	356 (9500), 605 (800)	348 (12 600), 623 (400)
[SN(H)S]M(PPh$_3$)	661 (600)	--	545 (700), 624 (1200)

2.2.4 Redox properties of [SNS$^{•}$]M(PPh$_3$)/ K(THF){[SNS^{cat}]M(PPh$_3$)}

Cyclic voltammetry was used to probe the ligand-centered redox event relating [SNS$^{•}$]M(PPh$_3$) and {[SNS^{cat}]M(PPh$_3$)}$^{1-}$ complexes for all three Group 10 metals. Data were collected on MeCN solutions containing 1 mM analyte and 0.1 M [Bu$_4$N][PF$_6$] as the supporting electrolyte using a standard three-electrode configuration: a glassy carbon working electrode, a platinum wire counter electrode, and a silver wire pseudo-reference electrode. All potentials were referenced to the [Cp$_2$Fe]$^{+/0}$ couple using an internal standard added to the cell at the end of the data collection. **Figure 2.4** shows the cyclic voltammograms collected for solutions of the salts K(THF){[SNS^{cat}]M(PPh$_3$)} (M = Ni, Pd, Pt). All three metal derivatives show reversible one-electron reductions ($i_{pa}/i_{pc} \cong 1$ and E_a-E_c = 80 mV), with the nickel derivative reduced at –0.61 V and the palladium and platinum derivatives reduced at progressively less-negative potentials of –0.58 V and –0.51 V, respectively. These values are reported in **Table 2.3**. Analogous results were obtained for [SNS$^{•}$]M(PPh$_3$) complexes in CH$_2$Cl$_2$ and THF; however, the neutral, radical species were not soluble enough in MeCN for direct measurement.
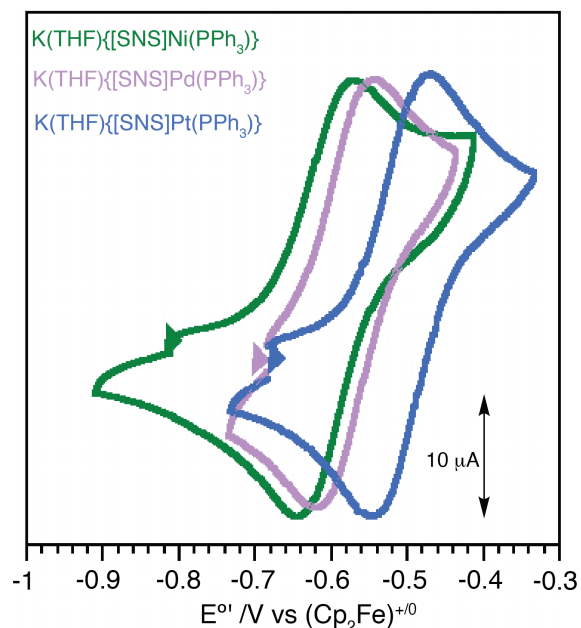
Figure 2.4. Cyclic voltammetry recorded with 1 mM analyte concentration K(THF){[SNS^{cat}]M(PPh$_3$)}, where M = Ni (green), Pd (purple), and Pt (blue), with 0.1 M [NBu$_4$][PF$_6$] electrolyte in dry, degassed MeCN under a nitrogen atmosphere using a 3 mm glass carbon working electrode, Pt wire counter electrode and Ag$^{+/0}$ pseudo-reference electrode at room temperature with 200 mV sec^{-1} scan rates. Open circuit potential indicated by arrowhead.

2.2.5 pK_a Determinations

The acidity of [SN(H)S]M(PPh$_3$) complexes were determined in non-aqueous solution by spectrophotometric titration, and the corresponding pK_a values are reported in **Table 2.3**. Previously, the pK_a of the nickel derivative was determined to be 15.9 in MeCN by titration with 2,4,6-trimethylpyridine (p$K_a^{(MeCN)}$ 14.98).[10,30] The *p*K_a of the palladium congener was determined using a similar procedure, monitoring the appearance of the absorbance band associated with {[SNS^{cat}]Pd(PPh$_3$)}$^{1-}$ at ~360 nm upon the portion-wise addition of base. **Figure 2.5** shows representative absorption spectra (A) and mass balance plots (B) for the [SN(H)S]M(PPh$_3$) titrations. Approximately 8000 equivalents of 2,4,6-trimethylpyridine were required to drive the reaction to completion, affording a pK_a value of 17.4. Additions were continued to 10 000 equivalents to ensure no competing or secondary reactions occurred. For the platinum derivative,

2,4,6-trimethylpyridine was not basic enough to drive the deprotonation to completion at reasonable concentrations of base, so triethylamine ($pK_a^{(MeCN)}$ 18.82)[30] was used to measure a pK_a value of 22.2 for [SN(H)S]Pt(PPh$_3$).

2.2.6 Equilibrium H-atom transfer reactions

The ability of [SN(H)S]M(PPh$_3$) complexes to participate in HAT reactions was verified under equilibrium conditions using established HAT reagents. As shown in representative spectra **Figure 2.5C**, the portion-wise addition of three equivalents of TEMPO$^\bullet$ (BDFE(O–H) = 66.2 kcal mol^{-1})[31] to a MeCN solution of [SN(H)S]Pd(PPh$_3$) resulted in the quantitative formation of [SNS$^\bullet$]Pd(PPh$_3$) giving an equilibrium constant K_{eq} of 4.4. Titration of [SN(H)S]Ni(PPh$_3$) with TEMPO$^\bullet$ gave similar results but required only 1.5 equivalents to reach completion, affording a K_{eq} of 120. In the case of the platinum derivative, [SN(H)S]Pt(PPh$_3$), addition of up to 100 equivalents of TEMPO$^\bullet$ did not affect the conversion to [SNS$^\bullet$]Pt(PPh$_3$). To probe H-atom abstraction from the platinum derivative, a stronger H-atom acceptor, galvinoxyl radical, was employed using benzene as the solvent (BDFE(O–H) = 74.1 kcal mol^{-1}).[32] In these experiments, approximately 5 equivalents of galvinoxyl radical were required to drive the reaction to completion affording an equilibrium constant of 2.2.
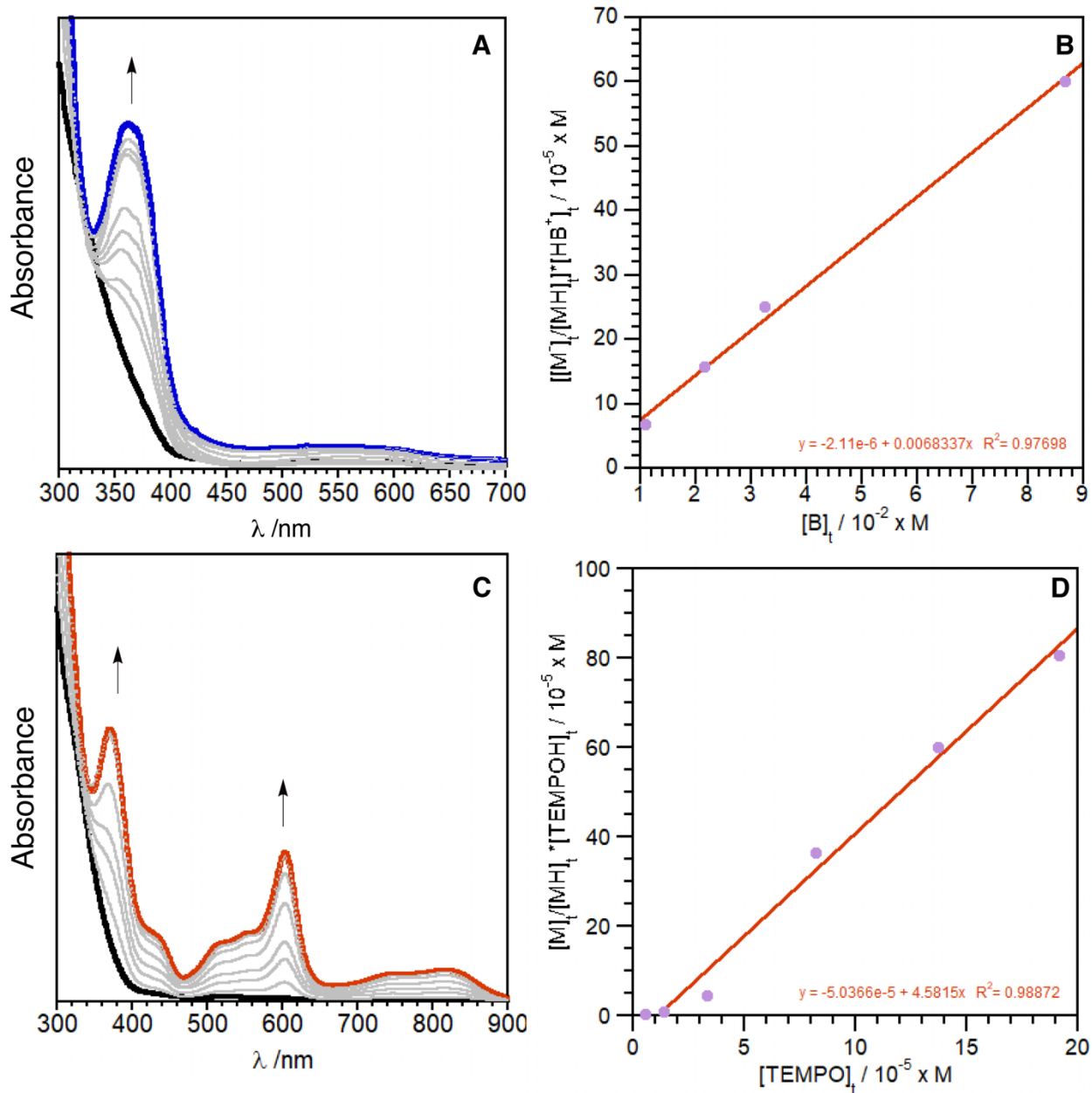
Figure 2.5. UV-vis absorption spectra associated with (A) the titration of [SN(H)S]Pd(PPh₃) with 2,4,6-trimethylpyridine at 298 K in MeCN showing the formation of {[SNS^{cat}]Pd(PPh₃)}$^{1-}$ and its associated K_{eq} determination plot (B) using mass balance formulas, and (C) the titration of [SN(H)S]Pd(PPh₃) with TEMPO• at 298 K in MeCN showing the formation of [SNS•]Pd(PPh₃) and its associated K_{eq} determination plot (D) using mass balance formulas.

Table 2.3. Experimentally determined thermodynamic properties in MeCN.

M	$E_1^{\circ\prime}$ / V[a]	pK_a[b]	BDFE[c] / kcal mol^{-1})	K_{eq}[d]	BDFE[e] / kcal mol^{-1}
Ni	-0.61	15.9 ± 0.5	62.6 ± 0.8	122 ± 10	63.8 ± 1.4
Pd	-0.58	17.4 ± 0.5	65.4 ± 0.7	4.4 ± 0.4	65.8 ± 0.6
Pt	-0.51	22.2 ± 0.4	73.6 ± 0.4	2.2 ± 0.2^f	73.6 ± 1.0^f

[a] Redox potentials of K(THF){[SNS^{cat}]M(PPh$_3$)} complexes referenced to [Cp$_2$Fe]$^{+/0}$. [b] pK_a measurements determined from deprotonation of [SN(H)S]M(PPh$_3$) with base. [c]Values determined using Equation 1. [d]Equilibrium measurements determined from [SN(H)S]M(PPh$_3$) with TEMPO. [e]BDFE(N–H) = BDFE(TEMPOH) – RTln(K_{eq}). [f]Equilibrium measurement determined from [SN(H)S]M(PPh$_3$) with galvonxyl radical in benzene.

2.2.7 Kinetics

To gain further insight into the influence of the metal ion on ligand-centered HAT reactivity by [SNS] complexes, kinetics measurements were carried out using TEMPO$^\bullet$ and TEMPO–H to probe the forward and reverse HAT reactions, respectively. In a typical experiment, shown in **Figure 2.6A**, a MeCN solution containing 45 µM [SN(H)S]M(PPh$_3$) (M = Ni and Pd), and 450 µM TEMPO$^\bullet$ was monitored by UV-vis spectroscopy at 298 K. Growth of a strong absorbance feature near 600 nm signaled the formation of the [SNS$^\bullet$]M(PPh$_3$) product. Under these conditions, the reactions followed pseudo-first-order kinetics; furthermore, **Figure 2.6B** shows the evaluation of k_{obs} for TEMPO$^\bullet$ concentrations between 450 and 2000 µM confirmed overall second-order kinetics as given by the rate law,

$$rate = k_{obs}\big[[SN(H)S]M(PPh_3)\big] = k_f\big[[SN(H)S]M(PPh_3)\big][TEMPO\cdot]$$

As expected given the thermodynamic constraints, while kinetics experiments for the forward reaction between TEMPO$^\bullet$ and [SN(H)S]M(PPh$_3$) proceeded smoothly for the nickel and

palladium derivatives, the analogous reaction between TEMPO$^{\bullet}$ and [SN(H)S]Pt(PPh$_3$) did not proceed. For all three metal ions, the kinetics of the reverse reaction could be probed by monitoring the reaction of [SNS$^{\bullet}$]M(PPh$_3$) (M = Ni, Pd, Pt) with excess TEMPO–H. The representative plot for this reaction is shown in **Figure 2.6D**. In all three cases, the reaction proceeded according to pseudo-first order kinetics to give the second-order rate law,

$$rate = k_{obs}\big[[SNS\cdot]M(PPh_3)\big] = k_r\big[[SNS\cdot]M(PPh_3)\big][TEMPOH]$$

Table 2.4 shows the second-order rate constants for the forwards and backwards HAT reaction at 298 K. **Table 2.4** also shows the ratio k_f/k_r for the nickel and palladium derivatives, and these ratios are consistent with the K_{eq} values measured under equilibrium conditions and presented in **Table 2.3**.
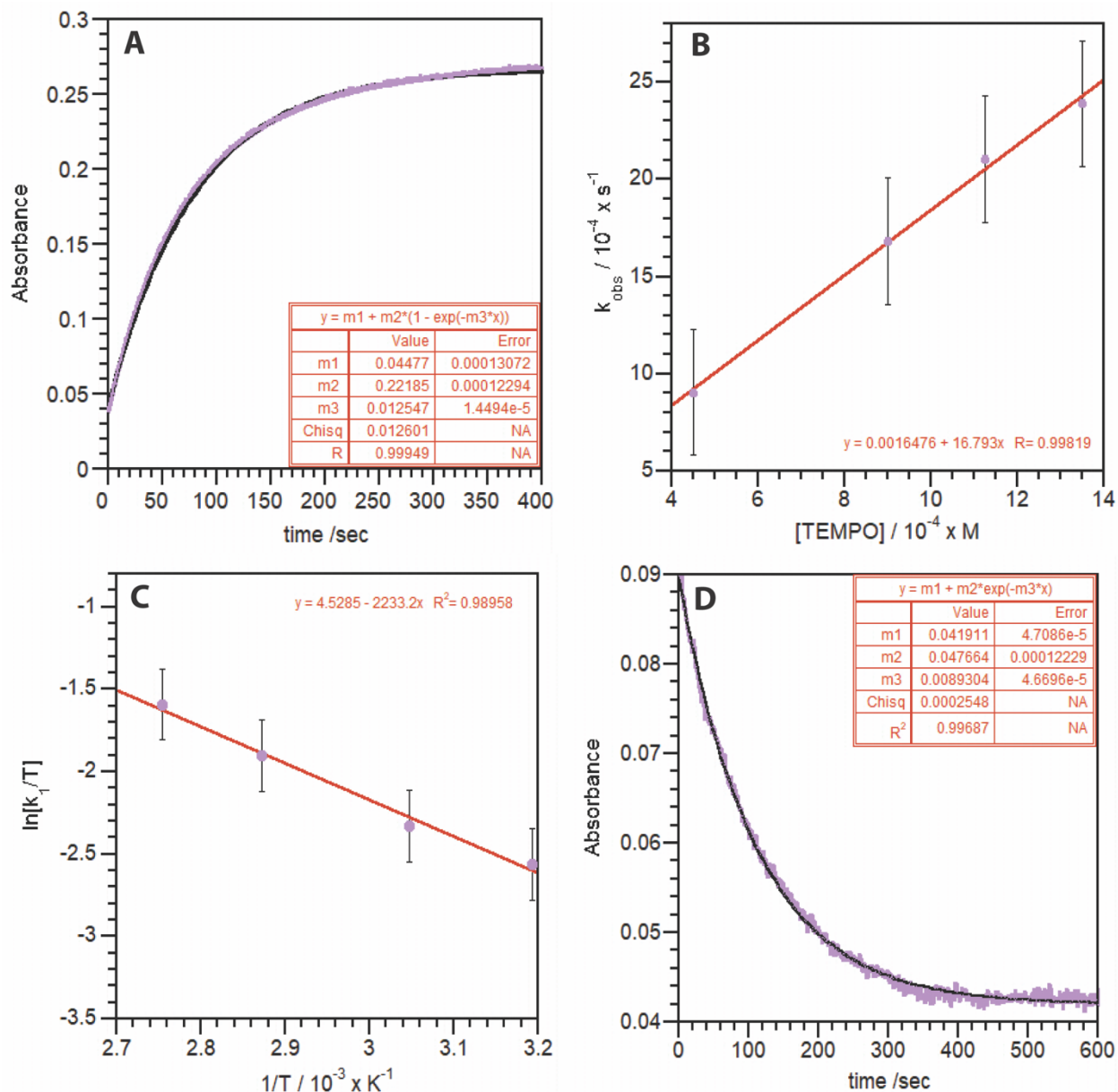
Figure 2.6. (A) Kinetic trace (606 nm) for the reaction of [SN(H)S]Pd(PPh₃) and TEMPO•. (B) Plot of k_{obs} versus [TEMPO•] for the reaction between [SN(H)S]Pd(PPh₃) and TEMPO•. The slope of the linear fit is the second-order rate constant, k_1. (C) Plot of $\ln(k_1/T)$ versus $1/T$ (where k_1 = second-order rate constant, T = temperature in K) for the reaction of [SN(H)S]Pd(PPh₃) with TEMPO•. The shown linear fit was used to calculate the activation parameters listed in Table 4 *via* the Eyring equation. (D) Kinetic trace (606 nm) for the reaction of [SNS•]Pd(PPh₃) and TEMPOH. Plots A–D are similar for M = Ni and Pt, and associated values are reported in Table 4.

Given that the backwards reaction between [SNS$^\bullet$]M(PPh$_3$) and TEMPO–H proceeds cleanly and completely for all three metal ions, the kinetic isotope effect for the HAT reaction could be determined readily at 298 K using TEMPO–D. The nickel complex [SNS$^\bullet$]M(PPh$_3$) afforded a KIE value of 1.8, while the palladium and platinum complexes gave smaller KIE values of 1.3 and 1.4, respectively.

Temperature dependencies of the pseudo-first-order rate constants for HAT were determined to help understand the activation parameters for reactivity. For the nickel and palladium derivatives, the temperature dependence of the forward HAT reaction between [SN(H)S]M(PPh$_3$) and TEMPO$^\bullet$ was determined under pseudo-first-order conditions. For the nickel derivative, the temperature window was 293-348 K; for the palladium derivative, the temperature window was 313-363 K. Eyring analyses, shown in **Figure 2.6C**, were used to extract $\Delta H^\ddagger$ and $\Delta S^\ddagger$ values that are collected in **Table 2.4**. In both the nickel and palladium cases, the activation barrier for the HAT reaction is dominated by the entropic rather than the enthalpic term. For the platinum derivative, the temperature dependence of the reverse reaction between [SNS$^\bullet$]Pt(PPh$_3$) and TEMPO–H was examined between 293 and 343 K. Again, as shown in **Table 2.4**, the activation barrier associated with the HAT reaction appears to be dominated by entropic considerations with a smaller enthalpic contribution.[33,34]

Table 2.4. Kinetic data for the HAT reaction between [SN(H)S]M(PPh₃) and TEMPO• and [SNS•]M(PPh₃) and TEMPOH in MeCN.

M	k_f / M⁻¹ s⁻¹	k_r / M⁻¹ s⁻¹	k_f/k_r	$\Delta H^{\ddagger}_f$ / kcal mol⁻¹	$\Delta S^{\ddagger}_f$ / eu	$\Delta H^{\ddagger}_r$ / kcal mol⁻¹	$\Delta S^{\ddagger}_r$ / eu	KIE (k_H/k_D)
Ni	59 ± 7	0.53 ± 0.01	110 ± 14	3.9 ± 0.2	-29 ± 0.7	--	--	1.8 ± 0.4
Pd	16 ± 5	1.8 ± 0.1	9 ± 3	5.5 ± 0.3	-27 ± 1.0	--	--	1.3 ± 0.4
Pt	--	87 ± 9	--	--	--	1.7 ± 0.3	-62 ± 2	1.4 ± 0.3

2.2.7 Density functional theory calculations for [SNS•]M(PPh₃)

The radical complexes [SNS•]M(PPh₃) (M = Pd, Pt) were examined using DFT calculations to further elucidate their electronic structures. Analogous calculations have been previously reported for the nickel derivative.[29] Gas-phase, spin-unrestricted DFT computations were carried out at the TPSS/def2-TZVP level of theory. The solid-state structures for [SNS•]Pd(PPh₃) and [SNS•]Pt(PPh₃) were used as starting points for geometry optimizations. Metal-heteroatom bond distances fell within 0.04 Å of the solid-state values, and intra-ligand bond distances all fell within 0.01 Å of the solid-state values. The distribution of spin-density for the radical complexes was of interest, and tabulated spin density distributions for all three complexes are given in **Table 2.5**. The total spin density on the metal ion follows a non-Periodic trend with 9% spin density on the nickel in [SNS•]Ni(PPh₃), only 3% spin density on the palladium in [SNS•]Pd(PPh₃), and 5% spin density on the platinum in [SNS•]Pt(PPh₃). Across all three complexes, the spin density on the ligand nitrogen remains relatively constant at 24-25%; whereas, the spin density on the phenyl rings and sulfur atoms are sensitive to the metal ion, with these fragments accounting for 67% of the spin density in the nickel derivative, 71% in the palladium

derivative, and 69% in the platinum derivative. Another point of interest in the calculations is the π-type interactions between the metal ion and the nitrogen atom of the ligand. **Figure 2.7** shows the Kohn-Sham molecular orbitals for the π and π* interactions between the metal ion and the ligand nitrogen atom. The π* orbitals are the SOMOs of the [SNS•]M(PPh₃) series of complexes and correlate well with the calculated spin density plots. The M–N π-bonding orbitals shown in **Figure 2.7** are low-lying, filled orbitals. For these π-bonding orbitals, the metal contribution is reversed: the nickel contributes 4%, the palladium accounts for 13%, and the platinum accounts for 11.5% occupancy. To a first approximation, the strength of this π interaction can benchmarked by the energy difference between the π-bonding and π* orbitals, which are calculated to be 3.66 eV for the nickel derivative, 3.82 eV for the palladium derivative, and 3.83 eV for the platinum derivative.
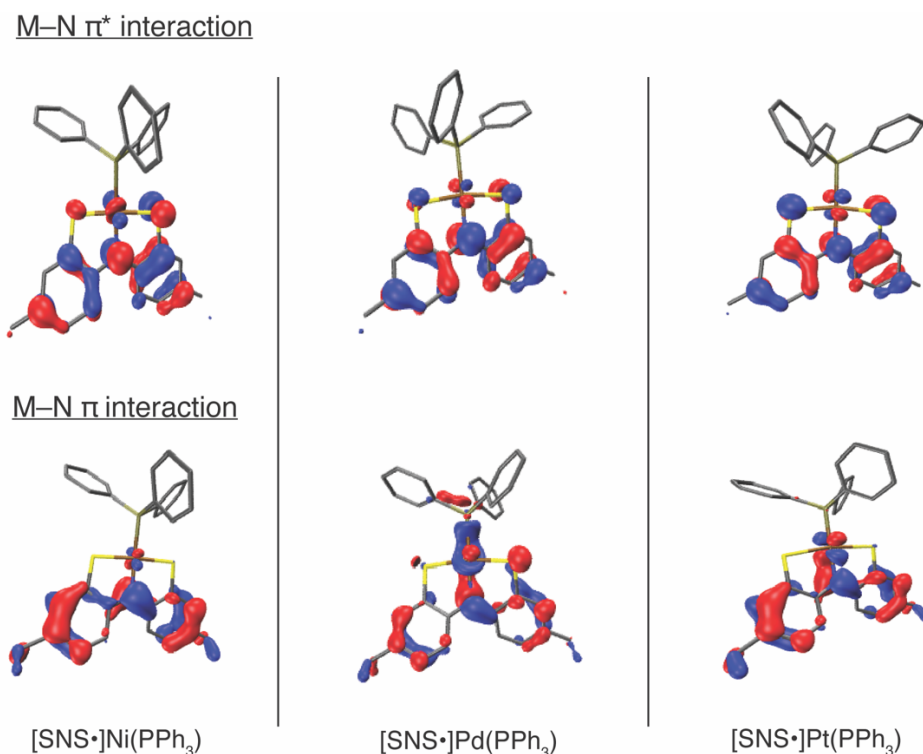
Figure 2.7. Kohn-Sham molecular orbitals showing M–N π (bottom) and π* (top) interactions for M = Ni, Pd, Pt. The π* orbital combination also is the SOMO of [SNS•]M(PPh₃).

Table 2.5. Spin density distributions for [SNS$^{\bullet}$]M(PPh$_3$) for M = Ni, Pd, and Pt.

	M	S	N	C^{SNS}	PPh$_3$
Ni	9.0	7.1	24.1	59.8	0.0
Pd	3.3	10.1	25.3	61.1	0.0
Pt	4.6	9.7	24.6	59.3	0.0

2.3 Discussion

The available structural and spectroscopic data for the [SNS] complexes of nickel, palladium, and platinum reveal subtle differences between the series. Solid-state structural data shows that changes to the ligand oxidation state and protonation state manifest similar changes to bond distances and angles within the complexes regardless of the identity of the coordinated metal ion. These structural variations implicate the ligand nitrogen atom as the primary locus both of one-electron redox and of proton binding in the metal complexes. Outside of the metrical variations directly associated with the size difference between the 3d metal nickel and the heavier metals palladium and platinum, bond lengths and angles for complexes with the same ligand oxidation and protonation state show a high degree of similarity. Spectroscopically, the complexes are similar as well. ^{1}H NMR data of the [SN(H)S]M(PPh$_3$) complexes are indistinguishable except for the N–H proton resonance, which shifts by 1.3 ppm to higher frequency going from nickel to palladium to platinum. The radical species, [SNS$^{\bullet}$]M(PPh$_3$), all exhibit features > 600 nm in the visible region of the electromagnetic spectrum, which are characteristic for ligand-based radicals and are typically assigned as intra-ligand (π-π*) charge-transfer transitions.[26,35] In the present study, these low-energy transitions show a non-periodic trend, increasing in energy from nickel to platinum to palladium. The EPR spectra of the [SNS$^{\bullet}$]M(PPh$_3$) complexes similarly show a non-Periodic trend. While all three derivatives conform to the expected ligand-centered-radical $S = \frac{1}{2}$ spin state,[36] the nickel and platinum spectra show evidence of low-symmetry distortions suggestive

of delocalization of the radical onto the metal center. This contention is supported by DFT computations performed on the $[SNS^\bullet]M(PPh_3)$ complexes, which show that the metal ion carries the greatest spin density in the nickel derivative, followed by the platinum derivative, and the metal ion carries the least spin density in the palladium derivative. Beyond this simple interpretation of the EPR spectral data, a more insightful correlation is difficult owing to the irregular shifts in the observed g values. The isotropic $g = 2$ spectrum of the palladium derivative is consistent with a ligand-based radical and minimal contribution from the metal center. In the case of the nickel derivative, a rhombic spectrum centered at $g = 2$ was obtained, most likely due to an increase in electron density on the metal center and contributions from the sulfur atom.[37] While the DFT calculations suggest that the total spin density on sulfur is smallest in the nickel derivative, it also shows that this spin density (7%) is shifted to only one sulfur atom, which breaks the symmetry of the complex and would lead to the observed rhombic splitting pattern. In the platinum derivative, a very broad signal was observed that was best fit assuming a weak axial distortion and hyperfine coupling to the platinum nucleus; however, the g values are lower than what would be expected for a SOMO with metal character. This type of shift has been previously observed with platinum diimine complexes, where mixing of low-energy excited states that contain significant contributions from vacant metal valence orbitals resulted in g values less than 2.0.[38–42]

Given the similarities across the Group 10 metal complexes of the $[SNS^\bullet]^{2-}$, $[SNS]^{3-}$, and $[SN(H)S]^{2-}$ ligands, it is difficult to rationalize the trend in BDFE values determined for the N–H bond of the $[SN(H)S]M(PPh_3)$ complexes. It is well established that the thermodynamics of HAT reactions – or more broadly PCET reactions – conform to Hess' Law and may be determined from the corresponding reduction potentials and pK_a values.[43] The relationships between the key complexes in this study are given in **Scheme 2.2**. As shown in **Table 2.3**, the reduction potentials

relating radical [SNS•]M(PPh₃) complexes to {[SNScat]M(PPh₃)}¹⁻ anions are all negative of the [Cp₂Fe]⁺/⁰ reference, with the nickel derivative showing the most negative potential at –0.61 V and the platinum derivative showing the least negative potential at –0.51 V. Thus, descending the Group 10 metals, the {[SNScat]M(PPh₃)}¹⁻ anions become successively *harder to oxidize*, a trend that is somewhat counterintuitive since 4*d* and 5*d* transition metals usually access higher oxidation states more readily than 3*d* transition metals. In this case, where oxidation is localized on the ligand, the trend is reversed, albeit over a relatively narrow 100 mV window. A more pronounced effect was observed in the measured pK_a values for the [SN(H)S]M(PPh₃) derivatives, specifically for the heaviest metal in the triad, platinum. According to **Table 2.3**, the pK_a values range from 15.9 for [SN(H)S]Ni(PPh₃) to 17.8 for [SN(H)S]Pd(PPh₃), and to 22.2 for [SN(H)S]Pt(PPh₃). Thus, descending the Group 10 metals, the [SN(H)S]M(PPh₃) complexes become less acidic or *harder to deprotonate*. Inasmuch as the removal of a hydrogen atom from [SN(H)S]M(PPh₃) is by definition the collective removal of a proton and an electron, it follows that the BDFE of the N–H bond increases upon descending the Group 10 metals according to the order Ni < Pd < Pt. The relationship between BDFE, redox potential ($E°'$) and acidity (pK_a) is given by **Eq. 1.3**, where C_g is the 54.9 kcal mol⁻¹.[31] Calculated BDFE values for the N–H bond of [SN(H)S]M(PPh₃) complexes are tabulated in **Table 2.3** and range from 63.8±1.4 kcal mol⁻¹ for nickel up to 73.6±1.0 kcal mol⁻¹ for platinum.

Equilibrium HAT reactions with TEMPO• and galvinoxyl radical were performed as an independent measurement of the calculated N–H BDFE values. These values are also presented in **Table 2.3,** and they correlate well with the values calculated according to **Eq. 1.3**. Notably, the N–H bonds of the nickel and palladium derivatives are weak enough that a facile reaction was observed with TEMPO•. For the platinum derivative, with the least negative $E°'$ value and the

lowest acidity (highest pK_a), **Eq. 1.3** predicts a stronger N–H bond. Accordingly, the platinum

derivative did not react with TEMPO$^\bullet$ under any conditions. Only upon addition of the stronger

H-atom acceptor galvinoxyl radical could HAT be observed. The big jump in N–H BDFE for the

platinum derivative was surprising and is mainly accounted for in the significantly higher pK_a

value associated with [SN(H)S]Pt(PPh$_3$). Such higher weighting from the pK_a value has been

reported by Borovik in an oxomanganese complex where the high basicity of the oxo ligand

accounts for its ability to abstract H-atoms from phenols.[19] Additionally, Tolman demonstrated

that a copper hydroxide complex that is highly basic but weakly oxidizing can still be a potent H-

atom abstractor.[44] These examples do not however, explain the large change in the pK_a value of

the platinum derivative compared to its $3d$ and $4d$ congeners. Similar equilibrium studies on a

series of Group 6 metal-hydrides observed a large change in pK_a from Cr (13.3) < Mo (13.9) <<

W (16.1), which was attributed to the larger size of the tungsten metal ion destabilizing the

resulting deprotonated complex rendering it more basic.[23,45] Therefore, the larger size of platinum

compared to palladium and nickel could be a large contributing factor to the observed increase in

basicity.

Scheme 2.2. H-atom transfer reaction between [SN(H)S]M(PPh$_3$) and TEMPO•.
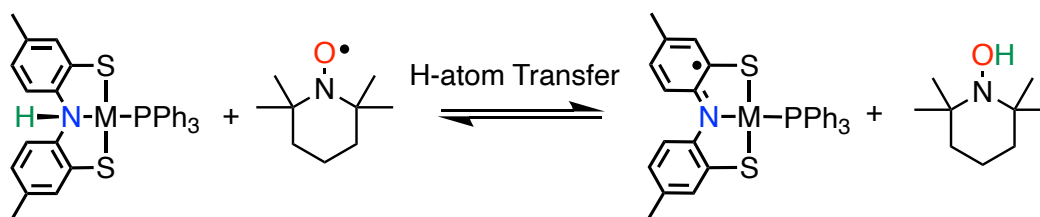
A second interesting thermodynamic feature in this family of [SN(H)S]M(PPh$_3$)

complexes, where the redox-active ligand serves as the source of both the proton and the electron

in the HAT reaction, is that the redox potentials and pK_a values *trend in the same direction*. That

is, moving down the Group 10 metal triad, the trend in the redox potentials and the trend in the

pK_a values trend together to increase the calculated N–H BDFE. This parallel trend in redox potential and pK_a upon substitution of isoelectronic metal ion is different than what is observed in many other synthetic systems, where the trends in redox potential and pK_a tend to counteract rather than reinforce one another. For example, this has been observed in Group 10 metal hydrides bearing bidentate phosphine ligands where the platinum complex is the least acidic but also the easiest to oxidize compared to its nickel and palladium analogues.[3] Another example from calorimetric studies on Group 6 and 8 metal-hydrides showed the pK_a values increased while the redox potentials decreased descending from Cr to W and Fe to Os.[23]

From a mechanistic perspective, the [SNS] complexes of nickel, palladium, and platinum appear to participate in HAT reactions that follow second-order kinetics, indicative of a simple bimolecular rate-determining step. Under pseudo-first-order conditions, the kinetics of HAT from [SN(H)S]M(PPh$_3$) to TEMPO$^\bullet$ were monitored by UV-vis spectroscopy for both nickel and palladium derivatives over a range of temperatures and TEMPO$^\bullet$ concentrations to afford second-order rate laws. In the platinum case, the kinetics of the reverse reaction were measured, namely [SNS$^\bullet$]M(PPh$_3$) and TEMPO–H, which also conformed to a second-order rate law. As summarized in **Table 2.4**, the barriers to HAT increase upon descending to the heavier Group 10 metals, but across all three metal ions, the activation barriers comprise small enthalpic factors and larger entropic factors. The large entropic contribution for a bimolecular reaction can be attributed to the organization required to bring together and organize the H-atom donor and acceptor in the transition state. The small kinetic isotope effect measured for HAT across the series of complexes is consistent with this interpretation, as it suggests that while HAT contributes to the rate-determining step, the enthalpic penalty for homolytic bond cleavage is not the dominant energy term in passing through the transition state.

2.4 Conclusions

Redox-active ligands continue to attract interest for implementation in the design of catalysts for multi-electron reactions. Given that many redox-active ligands owe their unique electronic properties to the presence of heteroatom donors like nitrogen or oxygen, it stands to reason that these ligand platforms can be effective reservoirs for both protons and electrons, leading to HAT type reactivity. In the homologous series of Group 10 complexes studied here, a clear trend in the thermodynamic parameters governing ligand-centered HAT emerged, summarized by an approximate 10 kcal mol^{-1} increase in N–H BDFE along the series Ni < Pd < Pt. The origin of this trend in BDFE values can be traced to increases both in the redox potential (complexes become harder to oxidize) and in the pK_a value (complexes become less acidic) upon descending from nickel to palladium to platinum. This trend highlights a strategy for the design of future HAT reagents and catalysts as judicious choice of the coordinated metal ion can be used to tune the ligand N–H BDFE and accordingly the H-atom donor or acceptor strength of the complex.

2.5 Experimental

General Considerations. The compounds and reactions reported below show various levels of air- and moisture- sensitivity; therefore all manipulations were performed using standard Schlenk-line and glovebox techniques. Hydrocarbon and ethereal solvents were sparged with argon being deoxygenated and dried by passage through Q5 and activated alumina columns, respectively. Halogenated solvents and triethylamine were sparged with argon and passed through two activated alumina columns. d$_8$-tetrahydrofuran (d$_8$-THF) and 2,4,6-trimethylpyridine were freeze-pump thawed thrice and stored over 3 Å molecular sieves. Acetonitrile-d$_3$ (CD$_3$CN) was dried over calcium hydride and distilled under reduced pressure prior to use. Triphenylphosphine was used as received, and potassium hydride was obtained in mineral oil and washed with pentane prior to

use. The ligand [SNS]H$_3$,[46] Cl$_2$Pd(PPh$_3$)$_2$,[47] Cl$_2$Pt(PPh$_3$)$_2$[48] and TEMPOH[49] were prepared from literature procedures. was prepared in a similar manner to the palladium analogue. 2,2,6,6-tetramethyl-piperidine-1-oxyl (TEMPO), ferrocene and decamethylcobaltocene were purified by vacuum sublimation and tetrabutylammonium hexafluorophosphate was recrystallized from ethanol three times and dried under vacuum.

Physical Methods. NMR spectra were collected at either 298 K or 258 K on a Bruker Avance 400 MHz, 500 MHz or 600 MHz spectrometer in dry, degassed C$_6$D$_6$ or d$_8$-THF. ^{1}H NMR spectra were referenced to tetramethylsilane (TMS) using residual proteo impurities of the solvent (7.16 ppm or 3.58 ppm) and ^{31}P{^{1}H} NMR spectra were referenced with an external standard of phosphoric acid (H$_3$PO$_4$, 85%, 0.00 ppm). All chemical shifts are reported in standard δ notation in parts per million. Perpendicular-mode X-band (9.352 GHz) EPR spectra were collected at 77 K using a Bruker EMX spectrometer equipped with ER041XG microwave bridge. The following spectrometer settings were used: attenuation = 20 dB, microwave power 1.997 mW, frequency = 9.352 GHz, modulation amplitude = 10.02 G, gain = 1.00 x 10^3, conversion time = 4.91 ms, time constant = 81.92 ms, sweep width 5500 G and resolution 1024 points. The spectra were simulated using EasySpin for MATLAB. Electrospray ionization mass spectrometry (ESI-MS) data were collected on a Waters LCT Premier mass spectrometer using dry, degassed MeCN or THF. Electronic absorption spectra were recorded using a Jasco V-670 or Cary 60 absorption spectrometer in dry, degassed MeCN using a 1-cm pathlength cells at ambient temperature (20-24 °C). Infrared (IR) spectra were recorded on a Thermo Scientific Nicolet iS5 spectrometer with an iD5 ATR attachment. **Electrochemical Methods**. Electrochemical experiments were performed on a Gamry series G300 potentiostat/galvanostat/ZRA (Gamry Instruments, Warminster, PA) using a 3.0 mm glassy

carbon working electrode, a platinum wire auxiliary electrode, and a silver wire pseudo reference electrode. Electrochemical experiments were performed at ambient temperature (20-24 °C) in a nitrogen-filled glovebox. Sample concentrations were 1.0 mM in analyte in MeCN containing 100 mM [NBu$_4$][PF$_6$] as the supporting electrolyte. All potentials are referenced to [Cp$_2$Fe]$^{+/0}$ using ferrocene or decamethylcobaltocene (-1.91 V vs [Cp$_2$Fe]$^{+/0}$) as an internal standard.[50]

Crystallographic Methods. X-ray diffraction data were collected at low temperature on single crystals covered in Paratone and mounted on glass fibers. Data were acquired using a Bruker SMART APEX II diffractometer equipped with a CCD detector. Measurements were carried out using Mo Kα (λ = 0.71073 Å) radiation, which was wavelength selected with a single-crystal graphite monochromator. A full sphere of data was collected for each crystal structure. The SMART program package was used to determine unit-cell parameters and to collect data. The raw frame data were processed using SAINT[51] and SADABS[52] to yield the reflection data files. Subsequent calculations were carried out using the SHELXTL program suite.[53] For [SN(H)S]M(PPh$_3$) and [SNS]M(PPh$_3$) (M = Pd and Pt), the diffraction symmetries were *2/m*, and *mmm*, respectively, and the systematic absences were consistent with the monoclinic space group P2$_1$/c, and orthorhombic space group P2$_1$2$_1$2$_1$, respectively and that were later determined to be correct. Structures were solved by direct methods and refined on F^2 by full-matrix least-squares techniques to convergence. Analytical scattering factors for neutral atoms were used throughout the analyses.[54] For [SN(H)S]Pd(PPh$_3$) and [SN(H)S]Pt(PPh$_3$), hydrogen atom H(1) was located from a difference-Fourier map and refined (x,y,z and U$_{iso}$). All other hydrogen atoms, though visible in the difference Fourier map, were generated at calculated positions and their positions refined using the riding model. ORTEP diagrams were generated using ORTEP-3 for Windows.[55]

Table 2.6. X-ray diffraction data collection and refinement parameters for [SNS•]Pd(PPh₃), K(2.2.2-crypt){[SNS]Pd(PPh₃)}, and [SN(H)S]Pd(PPh₃).

	[SNS•]Pd(PPh₃)	K(2.2.2-crypt) [[SNS]Pd(PPh₃)]• 2(C₄H₈O)	[SN(H)S]Pd(PPh₃) • 2(C₄H₈O)
empirical formula	C₃₂ H₂₇ N P Pd S₂	C₅₀ H₆₃ K N₃ O₆ P Pd S₂ • 2(C₄H₈O)	C₃₂ H₂₈ N P Pd S₂ • 2(C₄H₈O)
formula weight	627.03	1186.83	772.25
crystal system	Orthorhombic	Triclinic	Monoclinic
space group	$P2_12_12_1$	$P\bar{1}$	$P2_1/c$
T(K)	133(2)	88(2)	133(2)
a / Å	10.6609(12)	11.6753(14)	13.2925(14)
b / Å	13.5644(16)	15.4548(18)	20.468(2)
c / Å	19.067(2)	18.524(2)	13.7374(14)
α / deg	90	66.2747(14)	90
β / deg	90	79.8697(15)	105.2013(13)
γ / deg	90	69.6222(14)	90
V / Å³	2757.3(6)	2866.0(6)	3606.8(6)
Z	4	4	4
refl. collected	29908	33526	39733
indep. refl.	5664 [R(int) = 0.0298]	13474 [R(int) = 0.0282]	7944 [R(int) = 0.0433]
R1 ($I > 2\sigma$)[a]	0.0228 (0.0548)	0.0455 (0.1060)	0.0448 (0.1171)
wR2 (all data)[b]	0.0248 (0.0557)	0.0570 (0.1131)	0.0562 (0.1258)
GOF	1.067	1.039	1.041

[a]R1 = Σ||F_o|–|F_c||/Σ|F_o|; [b]wR2 = [Σ[w(F_o²–F_c²)²]/Σ[w(F_o²)²]]^½

Table 2.7. X-ray diffraction data collection and refinement parameters for [SNS•]Pt(PPh₃), K(2.2.2-crypt){[SNS]Pt(PPh₃)}, and [SN(H)S]Pt(PPh₃).

	[SNS•]Pt(PPh₃)	K(2.2.2-crypt){[SNS]Pt(PPh₃)}• 2(C₄H₈O)	[SN(H)S]Pt(PPh₃) • 2(C₄H₈O)
empirical formula	$C_{32} H_{27} N P Pt S_2$	$C_{50} H_{63} K N_3 O_6 P Pt S_2 \cdot 2(C_4H_8O)$	$C_{32} H_{28} N P Pt S_2 \cdot 2(C_4H_8O)$
formula weight	715.72	1275.52	860.94
crystal system	Orthorhombic	Triclinic	Monoclinic
space group	$P2_12_12_1$	$P\bar{1}$	$P2_1/c$
T(K)	88(2)	133(2)	88(2)
a / Å	10.6277(17)	11.738(8)	13.252(3)
b / Å	13.587(2)	15.455(11)	20.489(4)
c / Å	19.104(3)	18.560(13)	13.767(3)
α / deg	90	66.341(8)	90
β / deg	90	79.905(9)	105.201(3)
γ / deg	90	69.827(8)	90
V / Å³	2758.7(8)	2892(3)	3607.1(13)
Z	4	4	4
refl. collected	25475	20540	42768
indep. refl.	6556 [R(int) = 0.0521]	11490 [R(int) = 0.0325]	9169 [R(int) = 0.0419]
R1 ($I > 2\sigma$)[a]	0.0279 (0.0578)	0.0412 (0.0983)	0.0332 (0.0812)
wR2 (all data)[b]	0.0329 (0.0596)	0.0539 (0.1056)	0.0441 (0.0869)
GOF	1.026	1.042	1.024

[a]R1 = $\Sigma||F_o|-|F_c||/\Sigma|F_o|$; [b]wR2 = $[\Sigma[w(F_o^2-F_c^2)^2]/\Sigma[w(F_o^2)^2]]^{1/2}$; GOF = $[\Sigma w(|F_o| - |F_c|)^2/(n - m)]^{1/2}$

Theoretical Calculations. All calculations were performed with *TURBOMOLE 7.2*[56] using the non-empirical TPSS meta-generalized-gradient-approximation (meta-GGA) functional. For computational efficiency, initial geometry optimizations were performed using moderate split-valence plus polarization basis sets (def2-SVP)[57] and then refined using bases sets of triple-ζ valence plus polarizations (def2-TZVP) quality.[58,59] Atomic coordinates from the solid-state structures obtained from X-ray diffraction experiments were used as starting points for the geometry optimization no molecular symmetry was imposed. Molecular geometries and orbital energies were evaluated self-consistently to tight convergence criteria (energy converged to 0.1

μHartree; maximum norm of the Cartesian gradient $<10^{-4}$ au). Molecular orbital images were rendered using Visual Molecular Dynamics (VMD 1.9.3) software.[60]

pK_a and Equilibrium Measurements. The pK_a and K_{eq} values were determined by spectrophotometric titration following published methods.[61] Aliquots (200 μL) were removed from a MeCN stock solution of metal complex and a series of varying volumes of appropriate base (Ni and Pd, 2,4,6-trimethylpyridine, Pt, triethylamine) or TEMPO (TEMPOH for Pt) were added using a volumetric syringe and these solutions were diluted to 5 mL. Spectra changes were monitored between samples with a Jasco V-670 absorption spectrometer in 10 mm quartz cuvettes at 298 K.

Kinetic Measurements. In a typical experiment a solution of [SN(H)S]M(PPh$_3$) or [SNS•]M(PPh$_3$) (45 μM) in dry degassed MeCN in a 10 mm pathlength quartz cuvette that was fitted with a threaded stem and sealed with a rubber septum was placed in a Cary 60 spectrometer equipped with a thermostat cell holder that was connected to a Quantum Northwest TC1 temperature-regulated water bath. The sample was allowed to equilibrate at the 298 K for 2 minutes before it was injected with selected concentrations of an MeCN solution of TEMPO or TEMPOH (450-2000 μM) from a dram vial prepared in glovebox and sealed with a rubber septum. The course of the reaction was followed by monitoring the change in absorbance at 606 for palladium, 623 for platinum, and 663 for nickel. The kinetic studies were also carried out in the temperature range (293 K- 348 K) with set concentrations of 45 μM [SN(H)S]M(PPh$_3$) or [SNS•]M(PPh$_3$) and 500 μM TEMPO or TEMPOH(D).

[SNHS]Pd(PPh$_3$). In a 20 mL scintillation vial under a nitrogen glovebox atmosphere, a solution of [SNS]H$_3$ (100 mg, 0.38 mmol, 1.0 equiv.) in toluene (5 mL) was deprotonated using triethylamine (0.106 mL, 0.76 mmol, 2.0 equiv.). Yellow Cl$_2$Pd(PPh$_3$)$_2$ was then added (265 mg, 0.38 mmol, 1.0 equiv.) and an immediate color change to red was observed. The reaction stirred

at room temperature for 1 hour and color change to blue with red precipitate was observed. The solution was filtered through Celite using a medium porous fritted funnel, washed with toluene (15 mL) and an orange solid was collected in a 72 % yield. X-ray quality crystals were obtained from slow diffusion of a concentrated solution of analyte in THF into pentane at -36 °C. Anal. Calcd. $C_{32}H_{28}NPdPS_2$: C, 61.19; H, 4.49; N, 2.23. Found C, 59.53; H, 5.00; N, 1.91. ^{1}H NMR (400 MHz, d_8-THF) δ/ppm: 10.03 (s, 1H, -NH), 7.69-7.65 (t, J= 9.2Hz, 6H, aryl-H), 7.44-7.37 (dd, J= 6.88 Hz, 9H, aryl-H), 6.90 (br, 4H, aryl-H) 6.54 (br, 2H, aryl-H), 2.15 (s, 6H, -CH$_3$). ^{31}P{^{1}H} NMR (162 MHz, d_8-THF) δ/ppm: 34.45 ppm. MS (ESI+) (THF) m/z: 628 (M)$^+$.
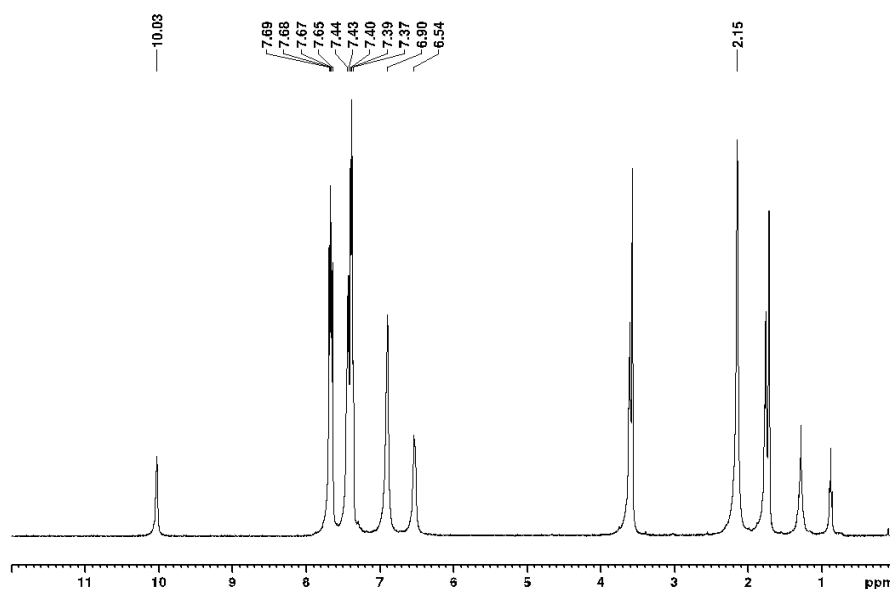
Figure 2.8. ^{1}H NMR spectrum of [SN(H)S]Pd(PPh$_3$) in d_8-THF at 298 K.

K(THF)$_n$[{SNS^{cat}}Pd(PPh$_3$)] Method A. In a 20 mL scintillation vial under a nitrogen glovebox atmosphere, a solution of [SNS]H$_3$ (94 mg, 0.37 mmol, 1.0 equiv.) in THF (5 mL) was deprotonated using KH (44 mg, 1.10 mmol, 3.0 equiv.) to yield an immediate white precipitate formation and the evolution of gas (H$_2$). Once the gas ceased, yellow Cl$_2$Pd(PPh$_3$)$_2$ was added

(2.54 mg, 0.37 mmol, 1.0 equiv.) and an immediate color change to purple was observed. The reaction stirred at room temperature for 1 hour then was filtered through Celite using a medium porous fritted funnel and washed with THF (40 mL). The filtrate volatiles were reduced in volume to 5 mL and a solid was precipitated from solution with pentane to afford a purple solid in a 62 % yield. X-ray quality crystals were obtained from slow diffusion of a concentrated solution of analyte with 2.2.2-cryptand in THF into pentane at -36 °C. Anal. Calcd. $C_{32}H_{27}NPdPS_2K(C_4H_8O)$: C, 58.57; H, 4.78; N, 1.90. Found C, 58.64; H, 4.82; N, 1.47. $^{31}P\{^1H\}$ NMR (162 MHz, d_8-THF) δ/ppm: 36.3 ppm. MS (ESI-)(THF) m/z: 625 (M)$^-$.

(Et$_3$NH)[{SNS^{cat}}Pd(PPh$_3$)] Method B. To an orange solution of [SN(H)S]Pd(PPh$_3$) (269 mg, 0.43 mmol) in THF, triethylamine was added (89 μL, 0.64 mmol, 1.5 equiv.). An immediate color change to purple was observed. The reaction was stirred for 1 hour at room temperature. The solution was filtered, and the solvent was removed *in vacuo* to afford a purple solid in a 62 % yield. ^1H NMR (400 MHz, C$_6$D$_6$) δ/ppm: 9.08 (s, 1.0H, Et$_3$N-H), 7.89-7.84 (m, 6H, aryl-H), 7.36 (br, 1H, aryl-H), 7.03-6.99 (m, 11H, aryl-H), 6.45 (br, 2H, aryl-H), 2.42-2.36 (q, J = 7.1 Hz, 6H, CH$_3$CH$_2$N-H), 2.00 (s, 6H, -CH$_3$), 0.94-0.91 (t, J = 14.2 Hz, 9H, CH$_3$CH$_2$N-H).
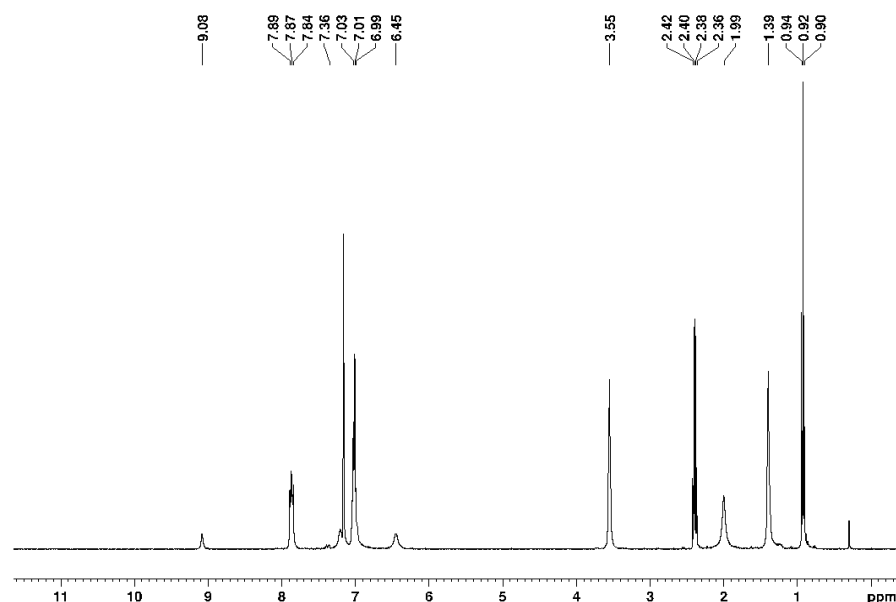
Figure 2.9. ^{1}H NMR spectrum of Et$_3$NH(THF)[SNS^{cat}]Pd(PPh$_3$) in C$_6$D$_6$ at 298 K.

[SNS•]Pd(PPh$_3$). In air, a 250 mL round bottom flask was charged with yellow Cl$_2$Pd(PPh$_3$)$_2$ (269 mg, 0.38 mmol, 1.0 equiv.) in 40 mL of toluene to give a yellow suspension. A solution of [SNS]H$_3$ (100 mg, 0.38 mmol, 1.0 equiv.) in toluene (10 mL) was added to the suspension and no immediate color change was observed. Triethylamine (0.16 mL, 1.14 mmol, 3.0 equiv.) was then added via syringe to induce a color change to brown followed by blue. The reaction was stirred at room temperature for 2 hours and the volatiles were removed *via* rotovap. The remaining solid was re-suspended in THF (10 mL) and stirred for 30 minutes. The mixture was filtered via Buchner funnel to remove Et$_3$NHCl and a red solid. The blue filtrate was collected, and volatiles were removed *via* rotovap. The resulting solids were re-dissolved in THF (5 mL) and a solid was precipitated from solution using pentane. A dark blue solid was collected on a Buchner funnel and dried under vacuum in a 76 % yield. X-ray quality crystals were obtained from aerobic oxidation of a concentrated solution of [SN(H)]Pt(PPh$_3$) in ethanol. Anal. Calcd. C$_{32}$H$_{27}$NPdPS$_2$: C, 61.29; H, 4.34; N, 2.23. Found C, 61.02; H, 4.53; N, 2.02. MS (ESI+) (THF) m/z: 627 (M)$^+$.

[SNHS]Pt(PPh₃). In a 20 mL scintillation vial under a nitrogen glovebox atmosphere, a solution of [SNS]H₃ (100 mg, 0.38 mmol, 1.0 equiv.) in toluene (5 mL) was deprotonated using triethylamine (0.106 mL, 0.76 mmol, 2 equiv.). White $Cl_2Pt(PPh_3)_2$ was then added (265 mg, 0.38 mmol, 1 equiv.) and an immediate color change to yellow was observed. The reaction stirred at room temperature for 1 hour. The solution was filtered through Celite using a medium porous fritted funnel and washed with toluene (15 mL) and a green solid was collected in a 62 % yield. X-ray quality crystals were obtained from slow diffusion of a concentrated solution of analyte in THF into pentane at -36 °C. Anal. Calcd. $C_{32}H_{28}NPtPS_2$: C, 53.62; H, 3.94; N, 1.95. Found C, 54.03; H, 4.06; N, 1.69. ¹H NMR (400 MHz, d₈-THF) δ/ppm: 10.53 (s, 1H, -NH), 7.70-7.65 (m, 6H, aryl-H), 7.43-7.39 (t, J=7.92 Hz, 9H, aryl-H), 7.01-6.96 (dd, J=20.52 Hz, 4H, aryl-H) 6.52 (s, J=7.60 Hz, 2H, aryl-H), 2.18 (s, 6H, -CH₃). ³¹P{¹H} NMR (162 MHz, d₈-THF) δ/ppm: 14.29 ppm. MS (ESI+) (THF) m/z: 1434 (dimer) (M)⁺.
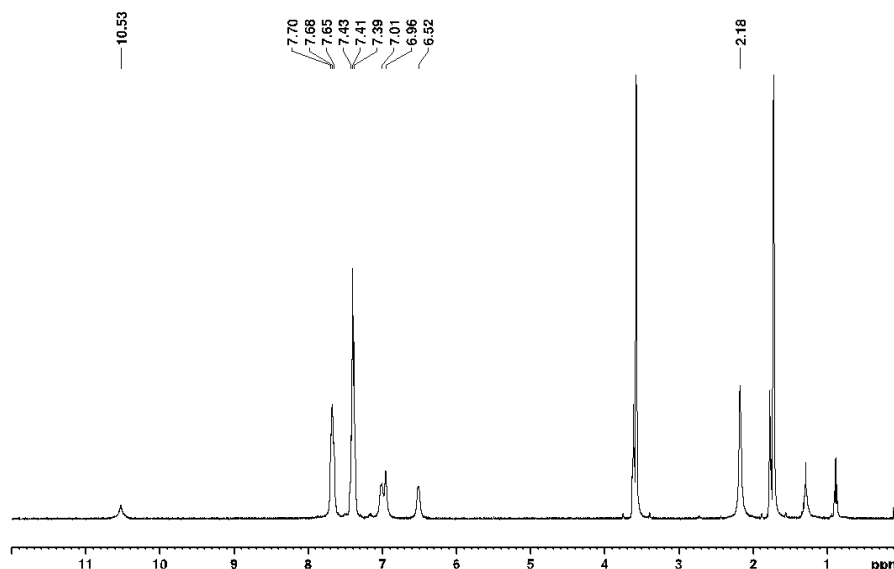
Figure 2.10. ¹H NMR spectrum of [SN(H)S]Pt(PPh₃) in d₈-THF at 298 K.

K(THF)$_n$[{SNS^{cat}}Pt(PPh$_3$)]. In a 20 mL scintillation vial under a nitrogen glovebox atmosphere, a solution of [SNS]H$_3$ (94 mg, 0.37 mmol, 1.0 equiv.) in THF (5 mL) was deprotonated using KH (44 mg, 1.10 mmol, 3 equiv.) to yield an immediate white precipitate formation and the evolution of gas (H$_2$). Once the gas ceased, white Cl$_2$Pt(PPh$_3$)$_2$ was added (254mg, 0.37 mmol, 1 equiv.) and an immediate color change to yellow was observed. The reaction was stirred at room temperature for 1 hour then was filtered through Celite using a medium porous fritted funnel and washed with THF (40 mL). The filtrate volatiles were reduced in volume to 5 mL and a solid was precipitated out of solution from pentane to afford a yellow solid in a 74 % yield. X-ray quality crystals were obtained from slow diffusion of a concentrated solution of analyte with 2.2.2-cryptand in THF into pentane at -36 °C. C$_{32}$H$_{27}$NPtPS$_2$K(C$_4$H$_8$O): C, 52.29; H, 4.27; N, 1.69. Found C, 52.15; H, 4.34; N, 1.55. ^{1}H NMR (500 MHz, d$_8$-THF) δ/ppm: 7.75-7.71 (t, J=8.45 MHz, 6H, aryl-H), 7.36-7.35 (d, J=7.25 MHz, 9H, aryl-H), 7.21 (br, 2H, aryl-H), 6.93 (br, 2H, aryl-H), 6.39 (br, 2H, aryl-H), 2.15 (s, 6H, -CH$_3$). ^{31}P{^{1}H} NMR (162 MHz, d$_8$-THF) δ/ppm: 20.2 ppm. MS (ESI$^-$)(THF) m/z: 716 (M)$^-$.
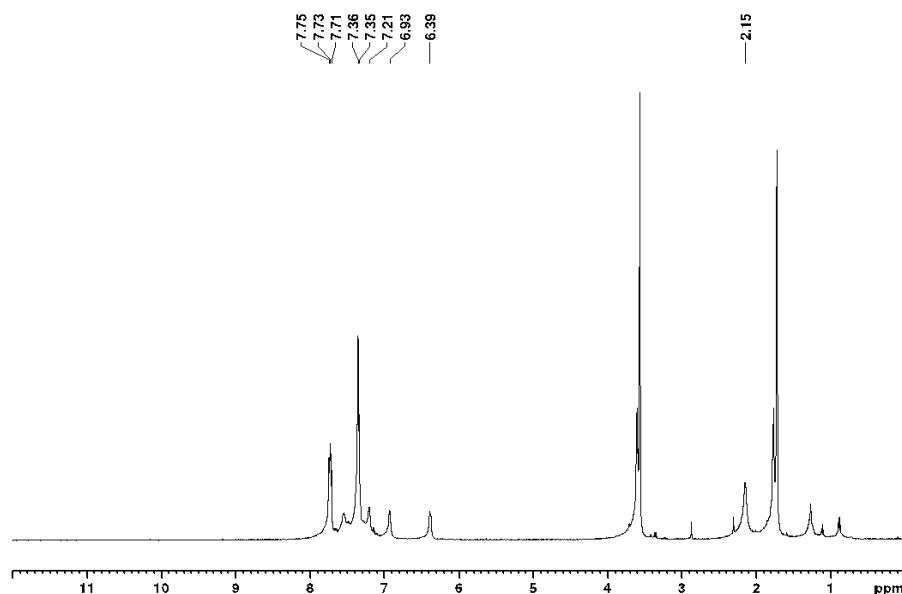
Figure 2.11. ^{1}H NMR spectrum of K(THF)[SNS^{cat}]Pt(PPh$_3$) in d$_8$-THF at 228 K.

[SNS•]Pt(PPh$_3$). In air, a 250 mL round bottom flask was charged with white Cl$_2$Pt(PPh$_3$)$_2$ (269 mg, 0.38 mmol, 1.0 equiv.) in 40 mL of toluene to give a white suspension. A solution of [SNS]H$_3$ (100 mg, 0.38 mmol, 1.0 equiv.) in toluene (10 mL) was added to the suspension and no immediate color change was observed. Triethylamine (0.16 mL, 1.14 mmol, 3.0 equiv.) was then added via syringe to induce a color change to brown followed by blue. The reaction stirred at room temperature for 2 hours and the volatiles were removed *via* rotovap. The remaining solid was re-suspended in THF (10 mL) and stirred for 30 minutes. The mixture was filtered via Buchner funnel to remove Et$_3$NHCl. The blue filtrate was collected, and volatiles were removed *via* rotovap. The resulting solids were re-dissolved in THF (5 mL) and a solid was precipitated from solution using pentane. A dark blue/green solid was collected on a Buchner funnel and dried under vacuum in a 68 % yield. X-ray quality crystals were obtained from aerobic oxidation of a concentrated solution

of [SN(H)S]Pt(PPh$_3$) in CD$_3$CN. C$_{32}$H$_{27}$NPtPS$_2$ (H$_2$O): C, 52.38; H, 3.98; N, 1.91. Found C, 52.27; H, 3.28; N, 1.84. MS (ESI+) (THF) m/z: 732 (M+ H$_2$O)$^+$.
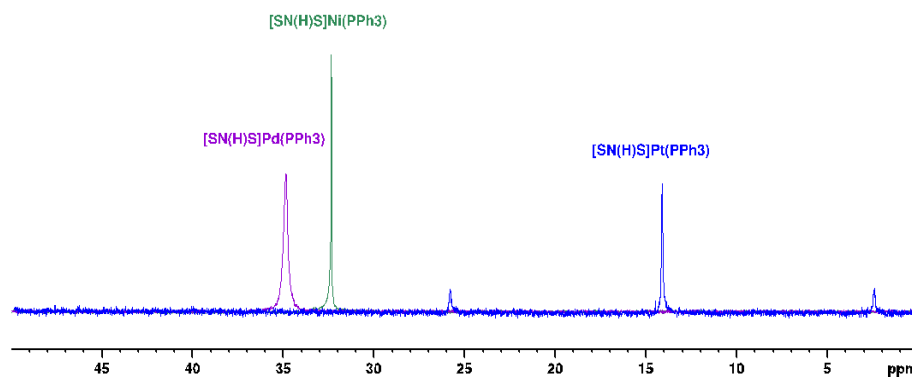
Figure 2.12. ^{31}P{^{1}H} NMR spectra of [SN(H)S]M(PPh$_3$) (M= Ni, Pd, Pt) in d$_8$-THF at 298 K.
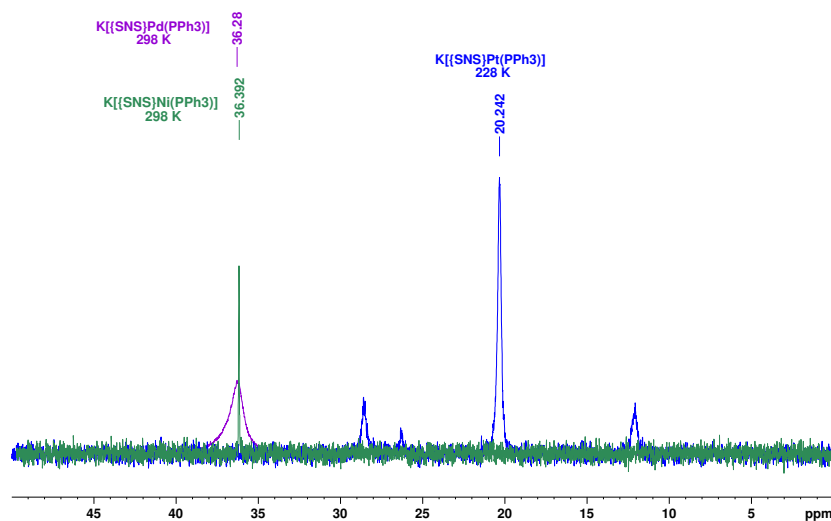
Figure 2.13. ^{31}P{^{1}H} NMR spectra of K(THF)[SNS^{cat}]M(PPh$_3$) in d$_8$-THF at 298 K for M= Ni and Pd, and 228 K for M= Pt.
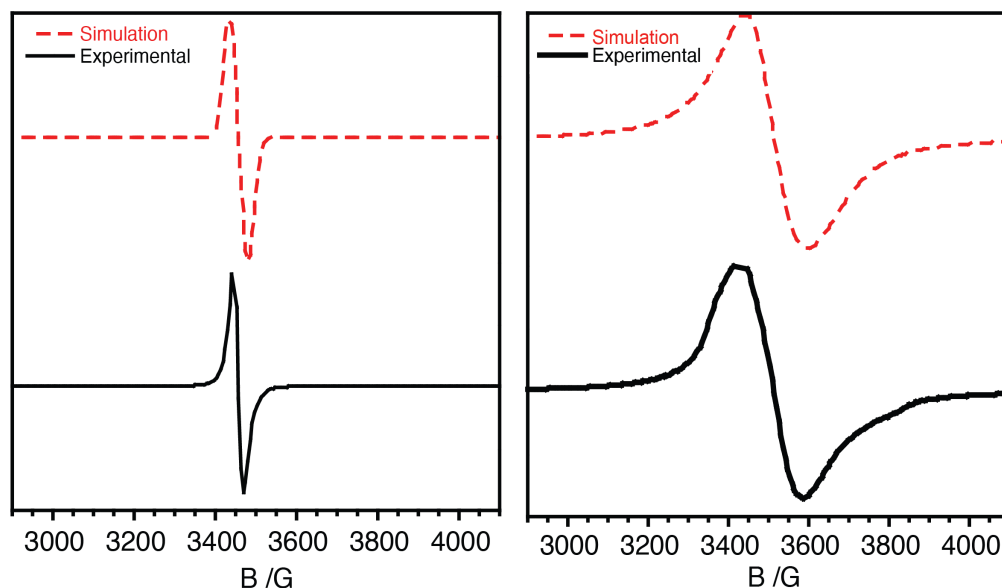
Figure 2.14. X-band EPR spectra (black) and simulation (red) of [SNS•]M(PPh₃) dissolved in C_6H_6 at 77 K where M = Pd (left) and M = Pt (right).

2.6 References

1   J. T. Groves, G. A. McClusky, R. E. White and M. J. Coon, *Biochem. Biophys. Res. Commun.*, 1978, **81**, 154–160.
2   Y. Hu and J. R. Norton, *J. Am. Chem. Soc.*, 2014, **136**, 5938–5948.
3   C. J. Curtis, A. Miedaner, J. W. Raebiger and D. L. DuBois, *Organometallics*, 2004, **23**, 511–516.
4   A. F. Sasayama, C. P. Kubiak, K. M. Waldie, A. L. Ostericher and M. H. Reineke, *ACS Catal.*, 2018, **8**, 1313–1324.
5   T. Y. Cheng, B. S. Brunschwig and R. M. Bullock, *J. Am. Chem. Soc.*, 1998, **120**, 13121–13137.
6   A. Wu and J. M. Mayer, *J. Am. Chem. Soc.*, 2008, **130**, 14745–14754.
7   E. A. McLoughlin, K. M. Waldie, S. Ramakrishnan and R. M. Waymouth, *J. Am. Chem. Soc.*, 2018, **140**, 13233–13241.
8   S. Raugei, S. Chen, M. H. Ho, B. Ginovska-Pangovska, R. J. Rousseau, M. Dupuis, D. L. DuBois and R. M. Bullock, *Chem. – A Eur. J.*, 2012, **18**, 6493–6506.
9   A. Wu, J. Masland, R. D. Swartz, W. Kaminsky and J. M. Mayer, *Inorg. Chem.*, 2007, **46**, 11190–11201.
10   K. E. Rosenkoetter, M. K. Wojnar, B. J. Charette, J. W. Ziller and A. F. Heyduk, *Inorg. Chem.*, 2018, **57**, 9728–9737.
11   M. C. Chang, A. J. McNeece, E. A. Hill, A. S. Filatov and J. S. Anderson, *Chem. - A Eur. J.*, 2018, **24**, 8001–8008.
12   E. J. Thompson and L. A. Berben, *Angew. Chemie Int. Ed.*, 2015, **54**, 11642–11646.
13   J. T. Henthorn and T. Agapie, *Inorg. Chem.*, 2016, **55**, 5337–5342.
14   T. J. Sherbow, J. C. Fettinger and L. A. Berben, *Inorg. Chem.*, 2017, **56**, 8651–8660.
15   G. W. Margulieux, M. J. Bezdek, Z. R. Turner and P. J. Chirik, *J. Am. Chem. Soc.*, 2017,

139, 6110–6113.

16   R. Pramanick, R. Bhattacharjee, D. Sengupta, A. Datta and S. Goswami, *Inorg. Chem.*, 2018, **57**, 6816–6824.

17   T. Matsumoto, H. C. Chang, M. Wakizaka, S. Ueno, A. Kobayashi, A. Nakayama, T. Taketsugu and M. Kato, *J. Am. Chem. Soc.*, 2013, **135**, 8646–8654.

18   K. T. Horak and T. Agapie, *J. Am. Chem. Soc.*, 2016, **138**, 3443–3452.

19   S. K. Barman, J. R. Jones, C. Sun, E. A. Hill, J. W. Ziller and A. S. Borovik, *J. Am. Chem. Soc.*, 2019, **141**, 11142–11150.

20   J. M. Mayer, *Acc. Chem. Res.*, 2011, **44**, 36–46.

21   J. J. D. Sacramento and D. P. Goldberg, *Acc. Chem. Res.*, 2018, **51**, 2641–2652.

22   D. E. Berning, B. C. Noll and D. L. DuBois, *J. Am. Chem. Soc.*, 1999, **121**, 11432–11447.

23   J. R. Sowa, J. B. Bonanno, V. Zanotti and R. J. Angelici, *Inorg. Chem.*, 1992, **31**, 1370–1375.

24   E. P. Cappellani, S. D. Drouin, G. Jia, P. A. Maltby, R. H. Morris and C. T. Schweitzer, *J. Am. Chem. Soc.*, 1994, **116**, 3375–3388.

25   L. Yang, D. R. Powell and R. P. Houser, *Dalton Trans.*, 2007, 955–964.

26   D. Herebian, E. Bothe, E. Bill, T. Weyhermüller and K. Wieghardt, *J. Am. Chem. Soc.*, 2001, **123**, 10012–10023.

27   M. Kato, T. A. Okamura, H. Yamamoto and N. Ueyama, *Inorg. Chem.*, 2005, **44**, 1966–1972.

28   J. Yasuda, K. Inoue, K. Mizuno, S. Arai, K. Uehara, A. Kikuchi, Y. N. Yan, K. Yamanishi, Y. Kataoka, M. Kato, A. Kawai and T. Kawamoto, *Inorg. Chem.*, 2019, **58**, 15720–15725.

29   K. E. Rosenkoetter, M. K. Wojnar, B. J. Charette, J. W. Ziller and A. F. Heyduk, *Inorg. Chem.*, 2018, **57**, 9728–9737.

30   I. Kaljurand, T. Rodima, I. Leito, I. A. Koppel and R. Schwesinger, *J. Org. Chem.*, 2000, **65**, 6202–6208.

31   J. J. Warren, T. A. Tronic and J. M. Mayer, *Chem. Rev.*, 2010, **110**, 6961–7001.

32   K. M. Conner, A. M. C. Arostegui, D. D. Swanson and S. N. Brown, *Inorg. Chem.*, 2018, **57**, 9696–9707.

33   S. N. Dhuri, Y.-M. Lee, M. S. Seo, J. Cho, D. D. Narulkar, S. Fukuzumi and W. Nam, *Dalton Trans.*, 2015, **44**, 7634–7642.

34   S. Wiese, J. L. McAfee, D. R. Pahls, C. L. McMullin, T. R. Cundari and T. H. Warren, *J. Am. Chem. Soc.*, 2012, **134**, 10114–10121.

35   A. M. Hollas, J. W. Ziller and A. F. Heyduk, *Polyhedron*, 2018, **143**, 111–117.

36   E. I. Stiefel, J. H. Waters, E. Billig and H. B. Gray, *J. Am. Chem. Soc.*, 1965, **87**, 3016–3017.

37   C. Makedonas and C. A. Mitsopoulou, *Eur. J. Inorg. Chem.*, 2006, 2460–2468.

38   K. Ray, T. Weyhermüller, F. Neese and K. Wieghardt, *Inorg. Chem.*, 2005, **44**, 5345–5360.

39   J. J. Loughrey, N. J. Patmore, A. Baldansuren, A. J. Fielding, E. J. L. McInnes, M. J. Hardie, S. Sproules and M. A. Halcrow, *Chem. Sci.*, 2015, **6**, 6935–6948.

40   E. J. L. McInnes, R. D. Farley, S. A. Macgregor, K. J. Taylor, L. J. Yellowlees and C. C. Rowlands, *J. Chem. Soc. - Faraday Trans.*, 1998, **94**, 2985–2991.

41   E. A. M. Geary, K. L. McCall, A. Turner, P. R. Murray, E. J. L. McInnes, L. A. Jack, L. J. Yellowlees and N. Robertson, *J. Chem. Soc. Dalt. Trans.*, 2008, 3701–3708.

42   J. A. Weinstein, M. T. Tierney, E. S. Davies, K. Base, A. A. Robeiro and M. W. Grinstaff, *Inorg. Chem.*, 2006, **45**, 4544–4555.

43   F. G. Bordwell, J. P. Cheng and J. A. Harrelson, *J. Am. Chem. Soc.*, 1988, **110**, 1229–1231.

44   D. Dhar and W. B. Tolman, *J. Am. Chem. Soc.*, 2015, **137**, 1322–1329.

45   R. F. Jordan and J. R. Norton, *J. Am. Chem. Soc.*, 1982, **104**, 1255–1263.

46   D. W. Shaffer, G. Szigethy, J. W. Ziller and A. F. Heyduk, *Inorg. Chem.*, 2013, **52**, 2110–2118.

47   N. P. Ramirez, I. Bosque and J. C. Gonzalez-Gomez, *Org. Lett.*, 2015, **17**, 4550–4553.

48   W. Oberhauser, C. Evangelisti, S. Caporali, V. Dal Santo, F. Bossola and F. Vizza, *J. Catal.*, 2017, **350**, 133–140.

49   E. A. Mader, A. S. Larsen and J. M. Mayer, *J. Am. Chem. Soc.*, 2004, **126**, 8066–8067.

50   N. G. Connelly and W. E. Geiger, *Chem. Rev.*, 1996, **96**, 877–910.

51   SAINT, version 8.34a; Bruker AXS Inc.: Madison, WI, 2013

52   G. M. Sheldrick, *SADBAS*, Bruker AXS Inc.: Madison, WI, 2014.

53   G. M. Sheldrick, SHELXTL; Bruker AXS Inc.: Madison, WI, 2014.

54   *International tables for crystallography. Vol. C: Mathematical, physical and chemical tables*, Kluwer Acad. Publ, Dordrecht, 3 *ed*., 1992.

55   L. J. Farrugia, *J. Appl. Crystallogr.*, 2012, **45**, 849–854.

56   *TURBOMOLE V7.2*; Turbomole GMBH; Karlsuhe, Germany, 2018.

57   A. Schäfer, H. Horn and R. Ahlrichs, *J. Chem. Phys.*, 1992, **97**, 2571–2577.

58   J. Tao, J. P. Perdew, V. N. Staroverov and G. E. Scuseria, *Phys. Rev. Lett.*, 2003, **91**, 146401.

59   A. Schäfer, C. Huber and R. Ahlrichs, *J. Chem. Phys.*, 1994, **100**, 5829–5835.

60   W. Humphrey, A. Dalke and K. Schulten, *J. Mol. Graph.*, 1996, **14**, 33–38.

61   A. Albers, S. Demeshko, S. Dechert, C. T. Saouma, J. M. Mayer and F. Meyer, *J. Am. Chem. Soc.*, 2014, **136**, 3946–3954.

Chapter 3

Reactivity of a Co(II) [SN(H)S] complex with aryl azides: evidence for multi-site electron-proton transfer (MS-EPT)

3.1 Introduction

Nitrene transfer or N-group transfer is an essential step for the formation of new X–N bonds, a process required for the production of natural products,[1] pharmaceuticals, and agrochemicals.[2] An attractive approach to achieve these transformations, from a conceptual perspective, is from reactivity of organic azides with transition metal complexes through nitrenoid intermediates which, include imido ($M(NR^{2-})$), iminyl ($M(NR^{-})$), and nitrene ($M(NR)$) complexes shown in **Scheme 3.1**. Organic azides are attractive choices for atom-economical nitrogen transfer reagents as molecular nitrogen is the only side-product generated. It is well established that such nitrenoid intermediates, which can possess metal-ligand multiple bonds, offer highly reactive sites for X–N bond formation, however, their direct isolation or spectroscopic detection of such species remain elusive.[3–9]

Scheme 3.1 Oxidation-state formalisms for transition metal nitrenoids complexes.

imido   *imnyl*   *nitrene*
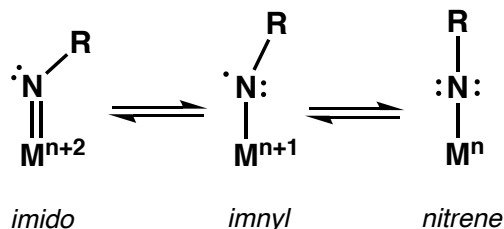
Late transition metal-nitrenoid complexes and their reactivity are relatively unexplored compared to their early and mid-transition metal counterparts due to their lack of propensity to form metal-ligand multiple bonds thanks to electron-rich metals with filled dπ orbitals. These limitations are circumvented through strategic ligand design and control over coordination and electronic environment.[10–16] The use of late transition metals with metal-ligand multiple bonds is advantageous over early or mid-transition metals for specific reactivity such as olefin aziridination and C–H bond aminations. The preferred reactivity is attributed to the less polarized nature of the metal-ligand multiple bond and a more electrophilic nitrene unit. For cobalt complexes with a

terminal [M(NR)] fragment, there exists several electronic possibilities shown in **Scheme 3.2**, including a high-valent cobalt imido $[Co^{n+2}(NR^{2-})]$, an iminyl adduct $[Co^{n+1}(\bullet NR^-)]$ or a nitrene adduct $[Co^n(NR)]$.

Scheme 3.2. Oxidation-state formalisms for cobalt nitrenoid complexes.
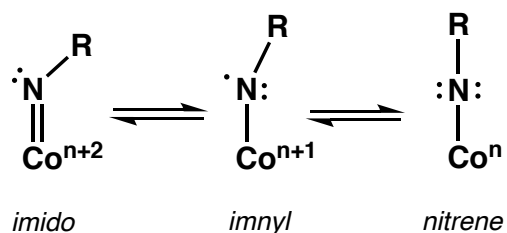
These oxidation-state assignments become more complicated when a redox-active ligand backbone is attached to the cobalt center. This situation allows for additional oxidation assignments as a result of electron transfer between the redox-active ligand and cobalt ion. For example, using the catecholate, semiquinonate, quinone nomenclature, one can pose three possible electronic assignments, $[(L^{cat})Co^{III}]$ or $[(L\bullet)Co^{II}]$ or $[(L^q)Co^I]$, for the same complex. For cobalt-nitrenoid complexes, low-spin electronic configurations often support complex stability as opposed to their open-shell alternatives, which often populate anti-bonding orbitals and facilitate a reactive species. Often, cobalt coordination complexes containing metal-ligand multiple bonds exist in low-spin ground state configurations; however, through the incorporation of weak field ligands, the ground state spin state can be tuned to high-spin through thermal spin crossover.[13,17] This spin-crossover, in conjunction with sterically unencumbered dipyrromethane ligands, has allowed for the characterization and isolation of an open shell metal-ligand multiple bond functionality useful for imido-group transfers.

This Chapter presents a *pseudo*-tetrahedral cobalt(II) complex, with a protonated redox-active ligand, [SN(H)S], that is capable of converting *p*-tolylazide into *p*-toluidine through the

transfer of two electrons and two protons. Through solid-state and spectroscopic analysis, the [SN(H)S]Co(dmap)$_2$ (dimethylaminopyridine = dmap) complex was determined to be *pseudo*-tetrahedral, with a high-spin $S = 3/2$ ground state. Reactivity studies with *p*-tolylazide revealed a 2:1 complex to reactant stoichiometry affording a singly oxidized and deprotonated [SNS]Co(dmap) complex, free dmap, and *p*-toluidine. This product is reminiscent of the results of hydrogen atom transfer reactivity with the parent Co(II) complex and H-atom acceptor TEMPO•. The resulting cobalt complex from these reactions has yet to be isolated; however, NMR studies indicate a diamagnetic species with one [SNS] ligand and one bound dmap ligand. Due to the lack of planarity, it is hypothesized that the [SN(H)S] serves only as a proton source while the cobalt (II) ion provides the electron in the observed reactivity. Further kinetic analysis was conducted to make inferences regarding the mechanism, including a slow loss of dmap ligand as the rate-determining step.

3.2 Results

3.2.1 Synthesis and Spectroscopic Characterization of [SN(H)S]Co(dmap)$_2$

Cobalt complexes of the bis(2-mercapta-*p*-tolyl)amine proligand [SNS]H$_3$, are directly accessible through metathesis reactions. This metathesis strategy is shown for the preparation of a new cobalt complex with double deprotonated ligand [SN(H)S]$^{2-}$ in **Scheme 3.3**. Here, stoichiometric deprotonation of the fully reduced [SNS]H$_3$ ligand with potassium hydride followed salt metathesis with CoCl$_2$(dmap)$_2$ afforded an olive-green solid with the formula [SN(H)S]Co(dmap)$_2$ in a 48 % yield.

Scheme 3.3. Synthesis of [SN(H)S]Co(dmap)₂.
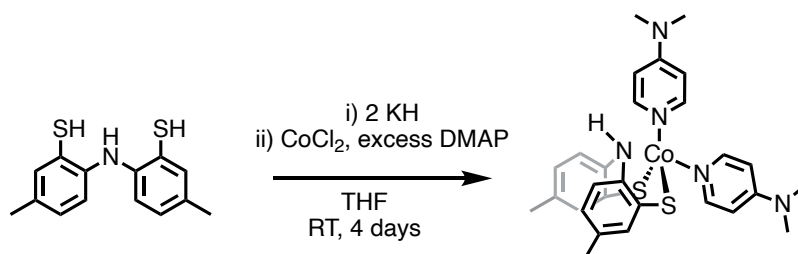
To probe the oxidation-state assignments of the metal and ligand, spectroscopic investigations on the new cobalt complex were conducted. The isolated olive-green complex afforded broad signals in the ^1H NMR spectrum indicative of a paramagnetic ground state. The X-band EPR spectrum, shown in **Figure 3.1,** was taken in CH_2Cl_2 at 4 K. The spectrum is characterized by a broad asymmetric signal with a g value of 3.58 with no visible hyperfine from ^{59}Co. The empirical formulation of [SN(H)S]Co(dmap)₂ was identified by ESI mass spectrometry.
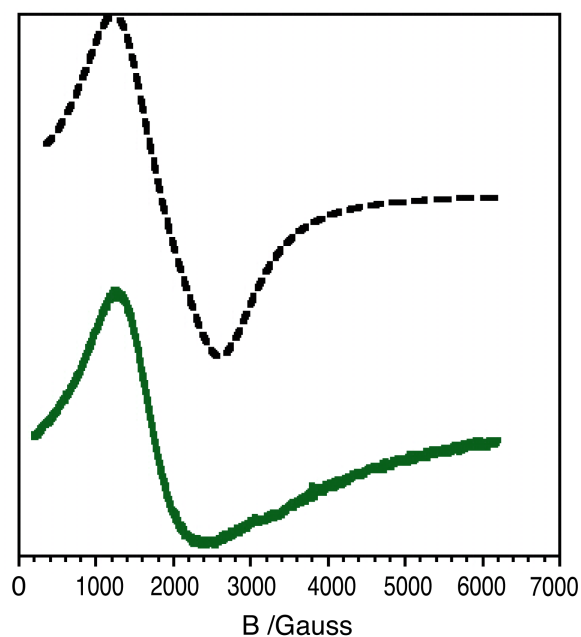
Figure 3.1. X-band EPR spectrum of [SN(H)S]Co(dmap)₂ in CH_2Cl_2 at 4 K with experimental spectrum shown in green and simulation in black.

3.2.2 Structural Characterization of [SN(H)S]Co(dmap)$_2$

To identify the cobalt coordination environment in the [SN(H)S]Co(dmap)$_2$ complex, single-crystal X-ray diffraction studies were performed. Green single-crystals suitable for X-ray diffraction studies were grown from slow diffusion of pentane into a concentrated solution of analyte in tetrahydrofuran (THF) at –36 °C. Pertinent bond distances and angles for [SN(H)S]Co(dmap)$_2$ are listed in **Table 3.1**. The coordination environment about the cobalt center is *pseudo*-tetrahedral with a τ_4 value of 0.92. **Figure 3.2** shows a cobalt metal center coordinated to the [SN(H)S] ligand in a κ^2-S$_2$ manner and two dmap ligands. The Co–S bond distances are similar to other cobalt (II) thiolates.[18–20] Average C–C and S–C intra-ligand bond distances are consistent with a fully reduced [SNS] ligand as would be expected for the protonated species.[21] The N–C bond distances are slightly shorter than the average 1.46 Å of the [SN(H)S] ligands with Group 10 metals, but due to its lack of coordination, is expected for an *sp^2* (*Csp^2 -Nsp^3*) amine bond.[22,23]
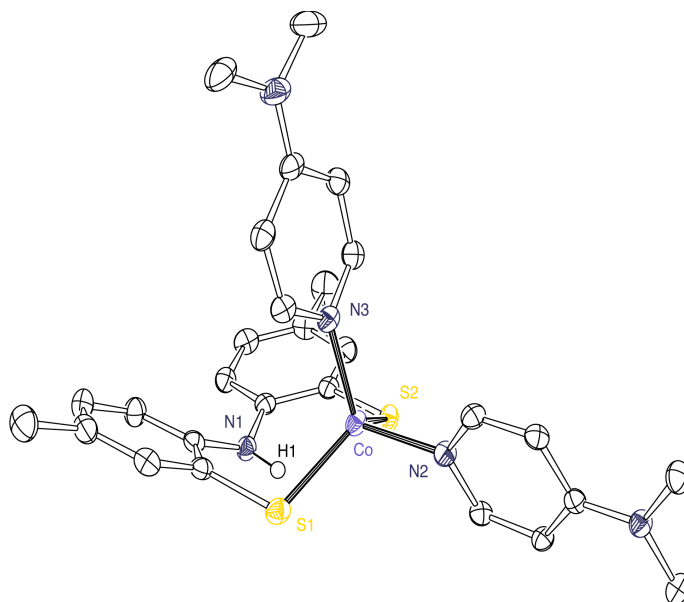
Figure 3.2. Solid-state structure for [SN(H)S]Co(dmap)$_2$ with thermal ellipsoids set at 50% probability. Hydrogen atoms and solvent molecules (Et$_2$O) are omitted for clarity.

Table 3.1. Selected bond distances (Å) and angles (°) from solid-state structures of [SN(H)S]Co(dmap)$_2$.

Bond Lengths (Å)		Bond Angles (°)	
Co–S1	2.2903(6)	S1–Co–S2	121.96(2)
Co–S2	2.2921(6)	N2–Co–S1	113.00(5)
N1–C8	1.401(3)	N2–Co–S2	107.31(5)
N1–C1	1.403(3)	N2–Co–N4	108.27(7)
C1–C2	1.419(3)	S2–Co–N4	106.03(5)
C8–C9	1.425(3)	S1–Co–N4	99.06(5)
S1–C2	1.773(2)	C8–N1–C1	129.90(17)
S2–C9	1.776(2)	τ_4	0.92

$$\tau_4 = \frac{360° - (\alpha + \beta)}{360° - 2\theta}$$

3.2.3 Reactivity with *p*-tolylazide and TEMPO•

With the tetrahedral $S = 3/2$ cobalt (II) complex in hand, reactivity with an aryl azide, a common source of transition metal imidos, was explored. **Scheme 3.4** shows the room temperature reaction of [SN(H)S]Co(dmap)$_2$ with *p*-tolylazide in THF. The reaction mixture was analyzed by various techniques, including ^{1}H NMR, UV-vis spectroscopy, and GC-MS. The ^{1}H NMR spectra and GC-MS showed the appearance of *p*-toluidine and free dmap by their characteristic methyl resonances and unique m/z ratios. To investigate the reactant stoichiometry, the reaction was monitored by UV-vis spectroscopy. **Figure 3.3A** shows Job plot analysis of the reaction mixture, which displayed a maximum value of 0.66, suggesting the reaction stoichiometry to be 2:1 cobalt complex to azide.
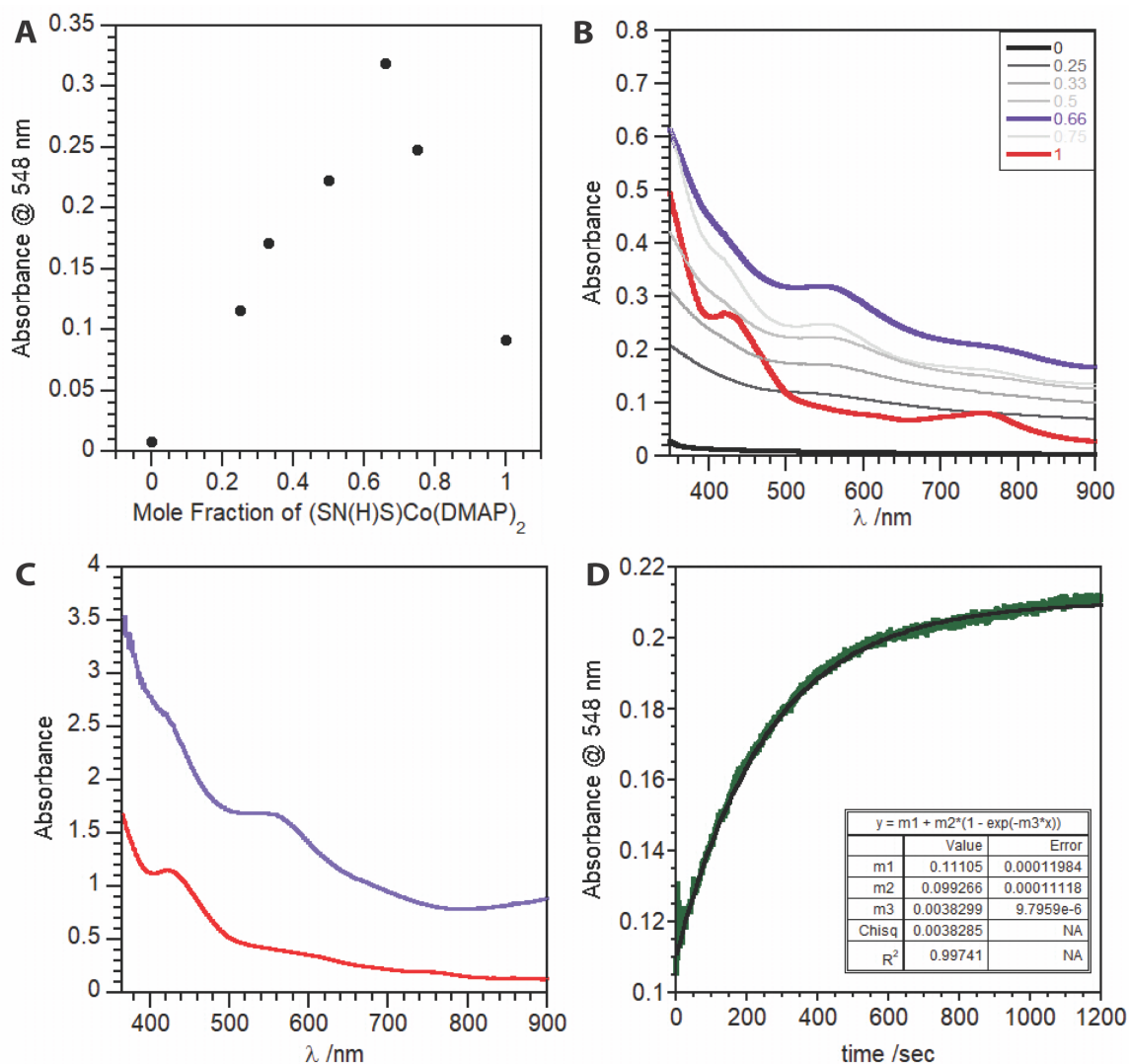
Figure 3.3. A Job plot analysis between [SN(H)S]Co(dmap)₂ and *p*-tolylazide in THF at 25 °C. **B** Absorbance plots with varying ratios of [SN(H)S]Co(dmap)₂ (red) to *p*-tolylazide (black) in THF at 25°C after 4 days. **C** Absorbance plot of [SN(H)S]Co(dmap)₂ (red) and following addition of TEMPO• (purple) in THF 25°C. **D** Kinetic trace (548 nm) for the reaction of [SN(H)S]Co(dmap)₂ and *p*-tolylazide. Reaction conditions: [[SN(H)S]Co(dmap)₂] = 100 μM, [*p*-tolyazide] = 1000 μM, THF, 298 K. The data were fit to a pseudo-first order model where [*p*-tolylazide] is ≥ 10-fold excess of [SN(H)S]Co(dmap)₂.

The identity of the resulting cobalt species was difficult to elucidate from the ¹H NMR spectrum due to overlapping signals from free dmap and *p*-toluidine. To overcome this limitation and to investigate further the reaction stoichiometry that suggested the transfer of two protons and

two electrons (two H-atom transfers), the HAT reactivity of the [SN(H)S]Co(dmap)$_2$ complex with known H-atom transfer acceptor TEMPO• (BDFE$_{O-H}$ = 66.2 kcal mol^{-1})[24] was explored.

Scheme 3.4. Reactivity assessment of [SN(H)S]Co(dmap)$_2$ with *p*-tolylazide (top) and TEMPO• (bottom).
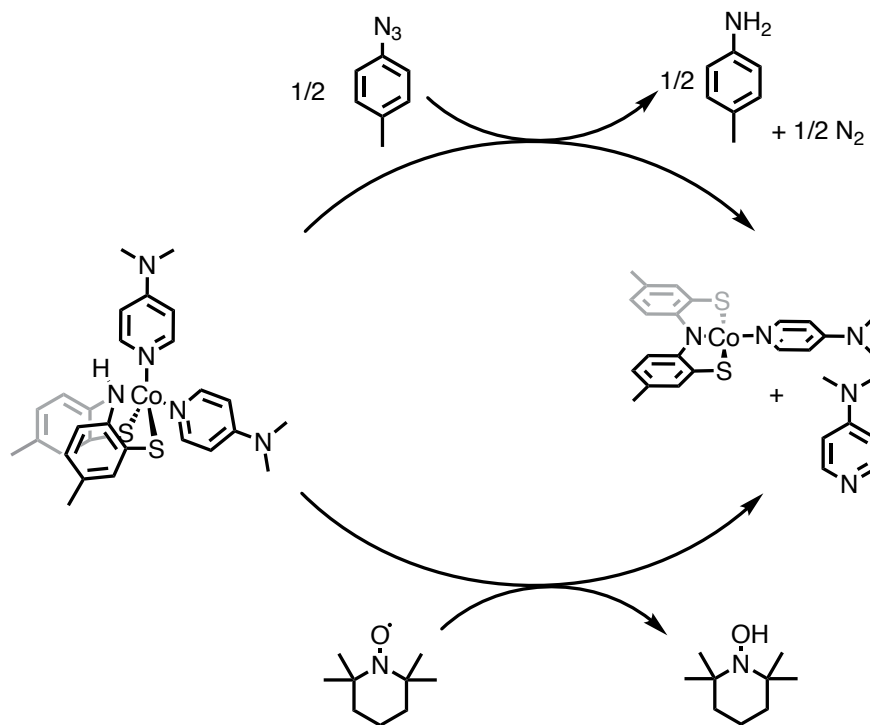
The reaction of H-atom transfer acceptor TEMPO• with the [SN(H)S]Co(dmap)$_2$ was monitored by ^{1}H NMR and UV-vis spectroscopy. The treatment of [SN(H)S]Co(dmap)$_2$ with one equivalent of TEMPO• afforded three diamagnetic products: free dmap, TEMPOH, and a deprotonated, singly oxidized cobalt complex [SNS]Co(dmap). At this time, two oxidation state assignments for this product can be considered, either [SNS^{cat}]Co^{III}(dmap) or [SNS•]Co^{II}(dmap). ^{1}H NMR analysis revealed a diamagnetic product with six unique aromatic resonances integrating to a total of 10 protons. The integration assignments align with a four-coordinate complex with one [SNS] ligand and one dmap ligand. Characteristic methyl resonances were also apparent around ~ 2.0 ppm. The four methyl resonances were assigned to free dmap, one bound dmap, and

two asymmetric tolyl groups on the [SNS] backbone. The reaction was also monitored by UV-vis spectroscopy to assist in discerning the identity of the final cobalt product. **Figure 3.3C** shows the initial spectrum (red) prior to addition of TEMPO• and the final spectrum (purple). The purple product spectrum shows similar features to the resultant spectrum from the reaction of [SN(H)S]Co(dmap)$_2$ with p-tolylazide shown in **Figure 3.3B**. Based on this evidence, it was determined that the cobalt product from both reactions are the same. Work into independently isolating this complex is still in progress.

3.2.4 Kinetic Analysis

To gain further insights into the mechanism of the transformation of p-tolylazide to p-toluidine, kinetic measurements were carried out. A typical experiment, shown in **Figure 3.3D**, consisted of 1000 µM of p-tolylazide added to 100 µM of [SN(H)S]Co(dmap)$_2$ either in the absence or presence of 1000 µM of dmap, monitored by UV-vis spectroscopy at 298 K. Initial reaction rates are reported in **Table 3.2**, which were determined in pseudo-first order conditions by monitoring reaction progression through the appearance of a charge-transfer band at 548 nm. In the presence of excess dmap, the initial rate decreased 1.5-fold. Kinetic isotope effects were measured by performing a deuterium exchange of the N–H bond in the [SN(H)S]Co(dmap)$_2$ complex and measuring the rate of reaction following the above procedure.

Table 3.2. Initial Rates and KIE of [SN(H)S]Co(dmap)$_2$ with p-tolylazide.

		+10 equiv. dmap	KIE (k_H/k_D)
Initial Rate /M^{-1} s^{-1}	3.83 ± 0.01	2.19 ± 0.004	1 ± 0.5

3.3.5 Density Functional Theory Calculations

In the absence of experimental characterization, computational work was conducted in an attempt to elucidate the potential structure and electronic nature of the resulting cobalt product from the reactions with p-tolylazide and TEMPO•. Gas-phase, spin-unrestricted DFT calculations

were carried out at the TPSS level using a def2-TZVP basis set[25,26] on four-coordinate [SNS]Co(dmap) and five-coordinate [SNS]Co(dmap)$_2$ structures built in Avogadro. Both calculations were refined and converged normally. The four-coordinate converged with a square planar geometry with a τ_4 value of 0.02. Similarly, the five-coordinate structure was best represented by a square-pyramidal geometry with a τ_5 value of 0.02. Mulliken population analysis of the HOMO of both structures was also similar, with the majority of the population residing on the [SNS] π system with contributions of 90 % for [SNS]Co(dmap) and 82 % for [SNS]Co(dmap)$_2$. **Figure 3.4** shows the Kohn-Sham diagrams for the HOMOs of the four and five-coordinate [SNS]Co(dmap)x (x = 1, 2) complexes. The relative energies extracted from the calculations proposed that a four-coordinate square planar [SNS]Co(dmap) structure is 3.0 kcal mol^{-1} lower in energy than a five-coordinate [SNS]Co(dmap)$_2$ alternative.

[SNS]Co(dmap)   [SNS]Co(dmap)$_2$
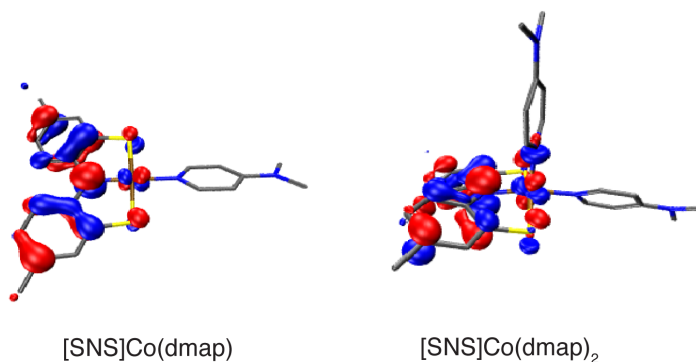
Figure 3.4 Kohn-Sham molecular orbitals of the HOMO for the [SNS]Co(dmap) and [SNS]Co(dmap)$_2$ optimized structures.

3.3 Discussion

3.3.1 Spin-state assignment for [SN(H)S]Co(dmap)$_2$

The spectroscopic and structural characterization of [SN(H)S]Co(dmap)$_2$ revealed a *pseudo*-tetrahedral Co(II) $S = 3/2$ complex with C_2 symmetry (**Figure 3.5**). Solid-state structural data revealed that compared to previously characterized [SN(H)S] complexes with Group 10

metals reported in Chapter 2,[21,27] there is a noticeable change in geometry from square planar to *pseudo*-tetrahedral. It is well established that four-coordinate coordination complexes generally adopt tetrahedral geometries with the exception of complexes with d^8 metals, which prefer square-planar geometries. This geometry change is therefore not surprising due to the change in d-electron count from d^8 in the Group 10 complexes to d^7 in [SN(H)S]Co(dmap)$_2$. The κ^2–S$_2$ coordination mode of the [SN(H)S] ligand was unexpected. The Group 10 complexes adopted four coordinate square planar geometries with the [SN(H)S] binding in a κ^3–S$_2$N tridentate fashion with one auxiliary triphenylphosphine (PPh$_3$) ligand.[27] This difference could be the result of the change in auxiliary ligand from PPh$_3$ to dmap as dmap is a better σ -donor than PPh$_3$ and the amine of the [SN(H)S] ligand. Therefore, the coordination of two dmap ligands with the κ^2–S$_2$ coordination mode from the [SN(H)S] ligand would be preferable over one dmap and the κ^3–S$_2$N mode. Various other N-donor ligand complexes are reported to have similar hypodentate character due to constrained geometries, bulky substituents and in the case of basic donor atoms, ligand protonation.[28–36]
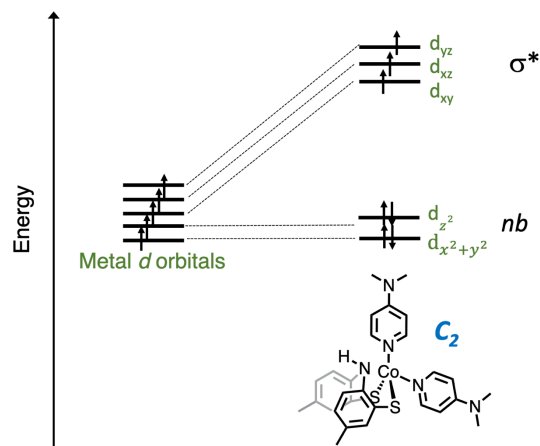
Figure 3.5. σ only frontier molecular orbital description of [SN(H)S]Co(dmap)₂.

The spin-state assignment of $S = 3/2$ was further corroborated by EPR spectroscopy. The spectrum exhibited a broad asymmetric signal with a g = 3.58 and no resolvable hyperfine interactions, which is suggestive of an $S = 3/2$ cobalt (II) complex. Similar spectra have been observed in a tetrahedral Co(II) phenylthiolate complex [Co(SPh)₄]²⁻ [37] and a *pseudo*-tetrahedral Co(II) hydroxide with tris(imidazole-2-ylidiene) ligand [PhB(*t*BIm)₃CoOH].[38] The former cobalt complex, [Co(SPh)₄]²⁻, exhibited a spectrum with a broad axial signal with g values at 2.0 and 5.3. A broad unresolved spectrum with a g = 3.58 could be the result of a similar electronic assignment. Broad spectra for tetrahedral high spin Co(II) complexes are expected due to a lack of uniformity among the distortion and conformations of the complexes in solution.[39,40]

3.3.2 H-atom or nitrene transfer

Recent literature[13,17,41–49] has set a precedent for the ability to isolate cobalt imido complexes with various auxiliary ligands in two, three, and four coordinate geometries. Due to the previous isolation of cobalt imido complexes with *pseudo*-tetrahedral geometries, the reaction of [SN(H)S]Co(dmap)₂ with *p*-tolylazide was carried out in an attempt to generate an isolable Co imido complex bearing a redox-active ligand. However, instead of the isolation of a cobalt imido

or iminyl, this reaction expelled *p*-toluidine. The transformation of an azide to an aniline requires i) the loss of N_2, ii) the transfer of two electrons, and iii) the transfer of two protons. The $[SN(H)S]Co(dmap)_2$ has the potential to store one electron and one proton in the ligand backbone with one caveat: the ligand must reorient to a planar geometry to access an electron from its π-system. This adds another step to the potential mechanism, where geometry reorganization that must occur along with or prior to electron transfer. It is also possible to access an electron from the cobalt ion by oxidizing to a Co(III) metal center.

The reactivity with $[SN(H)S]Co(dmap)_2$ and TEMPO• provides insight into the product of the reaction with *p*-tolylazide as the electronic absorption spectra for the products of both reactions are similar. The similarity of the absorption spectra from the *p*-tolylazide to *p*-toluidine and TEMPO• to TEMPOH transformations suggest that the $[SN(H)S]Co(dmap)_2$ supplies an H-atom to both reactions. Inasmuch, two oxidation-state possibilities could account for the diamagnetic cobalt product, a Co(II) with a singly-oxidized [SNS•] ligand radical where the two unpaired spins are anti-ferromagnetically coupled or a Co(III) with a fully reduced [SNS^{cat}] ligand The reaction product is expected to be four-coordinate with one [SNS] ligand and one dmap ligand based on the presence of free dmap in the ^{1}H NMR and GC-MS data. The energetic landscape for the four-coordinate [SNS]Co(dmap) was analyzed computationally. Upon analysis of the single unoccupied molecular orbital (SUMO) and the SUMO +1, it appears that the two unpaired electrons were sourced from metal-based d_{xz} and d_{yz} orbitals. From this analysis, the oxidation states of the diamagnetic cobalt complex best fit a Co(III) metal ion and a fully reduced [SNS^{cat}] ligand. While ligand field theory would suggest the Co(III) metal center would preferentially adopt an octahedral coordination environment over square planar, the π donation from the [SNS] sulfur

p orbitals and the π system of the aromatic backbone destabilizes the nonbonding d_{xz} and d_{yz} orbitals.

3.3.3 Mechanistic studies

From a mechanistic perspective, there are several key steps that effect the transformation of *p*-tolylazide to *p*-toluidine mediated by [SN(H)S]Co(dmap)$_2$. Such steps for this reaction include ligand dissociation, loss of N$_2$, geometry reorganization, and the transfer of two protons and two electrons or two H-atoms. When considering the kinetic measurements made in the presence of excess dmap ligand, the decrease in initial rate suggests that ligand dissociation is a rate-determining step. Furthermore, a KIE of ~1 indicates that the hydrogen transfer, either as a proton or as an H-atom, is fast.[50,51] From the kinetic analysis and computational results, insights into the mechanism of this reaction can be made. A putative mechanism is shown in **Scheme 3.5** showing the conversion of *p*-tolylazide into *p*-toluidine through metal-based oxidations and ligand deprotonations, an MS-EPT. Bridging nitrenes has been previously observed in late transition metal nitrenoid systems[12,52] and is hypothesized here based on the 2:1 stoichiometry determined from the Job plot analysis however, a mononuclear Co(III)-iminyl intermediate that performs an H-atom transfer from a second equivalent of [SN(H)S]Co(dmap)$_2$ followed by an intramolecular deprotonation cannot be excluded.

Scheme 3.5. Proposed Reaction Progression.
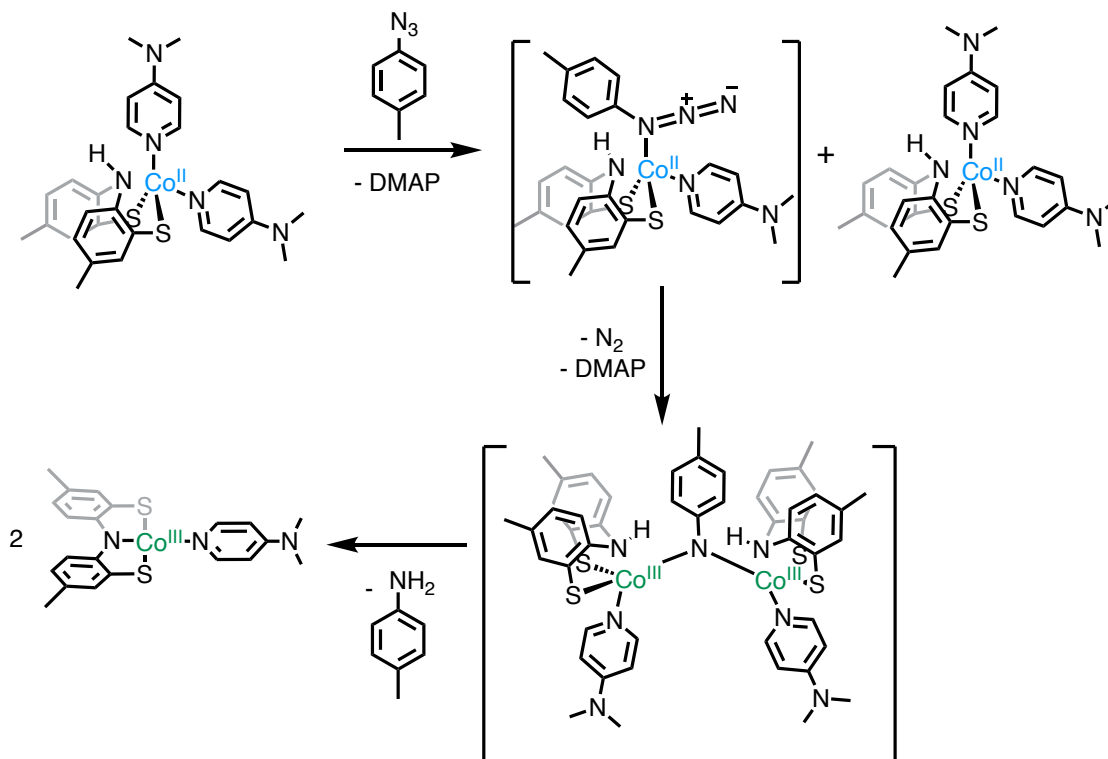
3.4 Conclusion

The synthesis, structure, and reactivity studies of a *pseudo*-tetrahedral cobalt (II) complex with redox and proton non-innocent [SN(H)S] ligand capable of transforming *p*-tolylazide into *p*-toluidine is reported. The reaction of [SN(H)S]Co(dmap)$_2$ with half an equivalent of *p*-tolylazide affords half an equivalent of *p*-toluidine as a result of the transfer of two protons and two electrons. Spectroscopic and GC-MS studies were used to determine the reaction stoichiometry and elucidate the identity of the organic products. The identity of the final cobalt complex as a four-coordinate square planar [SNS]Co(dmap) complex with a cobalt (III) metal center coordinated to a fully reduced [SNS] ligand was confirmed by reactivity studies with TEMPO• in corroboration with DFT studies. The protonation of the ligand backbone and its nonplanar geometry hinders its ability to perform electron transfer to the azide prior to deprotonation, and the electrons are therefore

sourced from two cobalt(II) ions. Kinetic studies provided insights into the mechanism of the azide transformation and suggest a slow dmap ligand dissociative rate-determining step followed by two electron transfers and two protons transfers facilitated by the metal and the protonated ligand, respectively.

3.5 Experimental

General Considerations. The compounds and reactions reported below show various levels of air- and moisture- sensitivity, therefore all manipulations were performed using standard Schlenk-line and glovebox techniques. Hydrocarbon and ethereal solvents were sparged with argon before being deoxygenated and dried by passage through Q5 and activated alumina columns, respectively. Halogenated solvents and triethylamine were sparged with argon and passed through two activated alumina columns. 4-dimethylaminopyridine and anhydrous $CoCl_2$ were used as received. TEMPO• was sublimed prior to use. The ligand $[SNS]H_3$[53] and p-tolylazide[54] were prepared from literature procedures.

Physical Methods. NMR spectra were collected at 298 K on a Bruker Avance 400 MHz or 600 MHz spectrometer in dry, degassed C_6D_6 or d_8-THF. ^1H NMR spectra were referenced to tetramethylsilane (TMS) using residual proteo impurities of the solvent (7.16 ppm or 3.58 ppm). All chemical shifts are reported in standard δ notation in parts per million. Perpendicular-mode X-band (9.352 GHz) EPR spectra were collected at 77 K using a Bruker EMX spectrometer equipped with ER041XG microwave bridge. The following spectrometer settings were used: attenuation = 20 dB, microwave power 1.997 mW, frequency = 9.352 GHz, modulation amplitude = 10.02 G, gain = 1.00 x 10^3, conversion time = 4.91 ms, time constant = 81.92 ms, sweep width 5500 G and resolution 1024 points. The spectra were simulated using EasySpin for MATLAB.

Electrospray ionization mass-spectrometry (ESI-MS) data were collected on a Waters LCT Premier mass spectrometer using dry, degassed MeCN or THF. Electronic absorption spectra were recorded using a Jasco V-670 absorption spectrometer or an Agilent Technologies Cary 60 UV-vis spectrometer in dry, degassed THF using a 1-cm path-length cells at ambient temperature (20-24 °C)

Crystallographic Methods. X-ray diffraction data were collected on single crystals mounted on glass fibers using a Bruker SMART APEX II diffractometer equipped with a CCD detector. Measurements were carried out using Mo K_α ($\lambda = 0.71073$ Å) radiation, which was wavelength selected with a single-crystal graphite monochromator. A full sphere of data was collected for each crystal structure. The SMART program package was used to determine unit-cell parameters and to collect data. The raw frame data were processed using SAINT[55] and SADABS[56] to yield the reflection data files. Subsequent calculations were carried out using the SHELXTL program suite.[57] There were no systematic absences nor any diffraction symmetry other than the Friedel condition. The centrosymmetric triclinic space group $P\bar{1}$ was assigned and later determined to be correct. Structures were solved by direct methods and refined on F^2 by full-matrix least-squares techniques to convergence. Analytical scattering factors for neutral atoms were used throughout the analyses.[58] Hydrogen atom H(1) was located from a difference-Fourier map and refined (x,y,z and U_{iso}). The remaining hydrogen atoms were included using a riding model. There was one molecule of tetrahydrofuran solvent present. The solvent was disordered and included using multiple components with partial site-occupancy-factors. ORTEP diagrams were generated using ORTEP-3 for Windows. [59]

Table 3.3. Crystal Data Collection and Refinement Parameters for [SN(H)S]Co(dmap)$_2$ •C$_4$H$_8$O

	[SN(H)S]Co(dmap)$_2$
empirical formula	C$_{28}$ H$_{33}$ Co N$_5$ S$_2$ •C$_4$H$_8$O
formula weight	634.75
crystal system	Triclinic
space group	$P\bar{1}$
T(K)	133(2)
a / Å	8.9423(12)
b / Å	12.0167(16)
c / Å	15.303(2)
α / deg	100.5189
β / deg	93.6133(16)
γ / deg	96.5710(16)
V / Å^3	1600.2(4)
Z	2
refl. collected	18300
indep. refl.	7566 [R(int) = 0.0280]
R1 ($I > 2\sigma$)^a	0.0397 (0.0538)
wR2 (all data)^b	0.0948 (0.1008)
GOF	1.041

Theoretical Calculations. All calculations were performed with *TURBOMOLE 7.3*[60] employing the nonempirical TPSS meta-generalized-gradient-approximation (meta-GGA) functional. For computational efficiency, initial geometry optimizations were performed using moderate split-valence plus polarization basis set (def2-SVP).[61] Structures were refined using basis sets of triple-ζ valence plus polarization (def2-TZVP) quality.[25,26] Crystal structures obtained from X-ray diffraction experiments were used as starting points for the geometry optimization; no molecular symmetry was imposed. Molecular geometries and orbital energies were evaluated self-consistently to tight convergence criteria (energy converged to 0.1 μHartree, maximum norm of the Cartesian gradient $\leq$10^{-4} a.u.). All images showing molecular orbitals and spin-density surfaces were created using Visual Molecular Dynamics (VMD) 1.9.3 software.[62]

Reactivity Studies. The reactivity profiles of [SN(H)S]Co(dmap)$_2$ with *p*-tolylazide and TEMPO•

were determined by monitoring changes in the electronic absorption spectrum from 350-900 nm.

For the Job Plot analysis, aliquots were removed from a THF stock solution of the metal complex

and a series of varying volumes of *p*-tolylazide were added using a volumetric syringe to make up

various stoichiometric ratios. These solutions were diluted to 5 mL and stirred for 4 days. Spectral

changes were monitored of each sample with a Jasco V-670 absorption spectrometer in 10 mm

quartz cuvettes at 298 K. The reactivity with TEMPO• was also monitored by ^{1}H NMR

spectroscopy where the reaction was set up in a 1:1 ratio of [SN(H)S]Co(dmap)$_2$ and TEMPO• in

C$_6$D$_6$ and the spectrum was obtained after approximately 30 minutes.
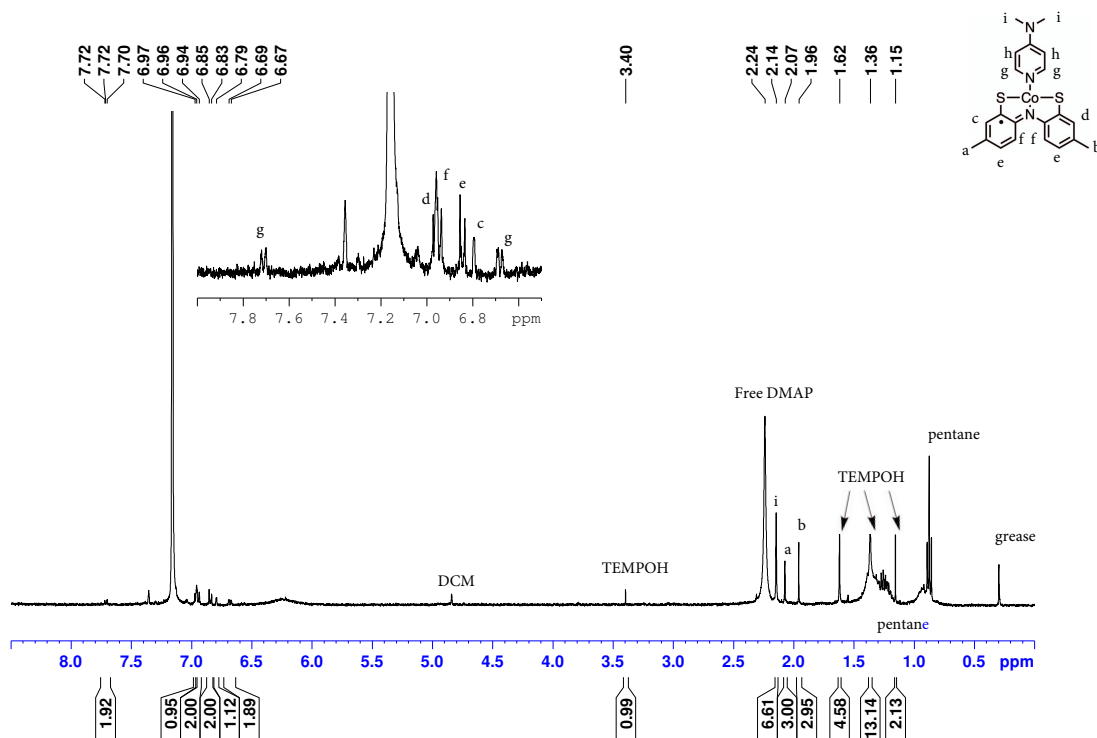
Figure 3.6. ^{1}H NMR spectrum of the reaction of [SN(H)S]Co(dmap)$_2$ and TEMPO• in C$_6$D$_6$ at 298 K.

Kinetic Studies. In a typical experiment, a solution of [SN(H)S]Co(dmap)$_2$ (100 µM) in dry, degassed THF in a 10-mm-path-length quartz cuvette was placed in a Cary 60 spectrometer in a nitrogen-filled glovebox. The sample was injected with a THF solution of *p*-tolylazide (1000 µM). The course of the reaction was followed by monitoring the change in absorbance at 548 nm. Additional experiments were conducted using [SN(D)S]Co(dmap)$_2$, obtained by stirred [SN(H)S]Co(dmap)$_2$in d$_4$-MeOD for 24 h then removing solvent *in vacuo*, and in the presence of excess dmap (1000 µM).

[SN(H)S]Co(dmap)$_2$: In a 20 mL scintillation vial under a nitrogen glovebox atmosphere, a solution of [SNS]H$_3$ (100 mg, 0.38 mmol, 1.0 equiv.) in THF (3 mL) was deprotonated using KH (31 mg, 0.78 mmol, 2 equiv.) to yield an immediate white precipitate and the evolution of gas (H$_2$).

Once the gas ceased, the white suspension was frozen. Concurrently, blue $CoCl_2$ (50 mg, 0.38 mmol, 1 equiv.) and white dmap (93 mg, 0.76 mmol, 2 equiv.) were stirred in THF (5 mL) for 2 hours then frozen. Upon thawing, the solutions were combined and an immediate color change from blue to brown was observed. The reaction stirred at room temperature for 2 days, then was filtered through Celite using a medium porous fritted funnel and washed with THF (30 mL). The filtrate volatiles were concentrated to 5 mL and powder was crashed out with pentane to afford a dark brown solid in a 48 % yield. X-ray quality crystals were obtained by slow diffusion of pentane into an THF solution of the complex at –36 °C. $C_{49}H_{56}N_8Co_2S_4$: C, 58.67; H, 5.63; N, 11.17. Found C, 58.69; H, 5.57; N, 1135. MS (ESI+) (THF) m/z: 603 (M$^+$ MeCN)$^+$, 726 (M + dmap + MeCN)$^+$.

3.6 References

1   D. O'Hagan, *Nat. Prod. Rep.*, 2000, **17**, 435–446.
2   J. Franzén, M. Marigo, D. Fielenbach, T. C. Wabnitz, A. Kjærsgaard and K. A. Jørgensen, *J. Am. Chem. Soc.*, 2005, **127**, 18296–18304.
3   J. T. Groves and T. Takahashi, *J. Am. Chem. Soc*, 1983, **105**, 2073–2074.
4   J. Du Bois, C. S. Tomooka, J. Hong and E. M. Carreira, *Acc. Chem. Res.*, 1997, **30**, 364–372.
5   R. A. Eikey and M. M. Abu-Omar, *Coord. Chem. Rev.*, 2003, 243, 83–124.
6   M. D. Fryzuk and C. D. Montgomery, *Coord. Chem. Rev.*, 1989, **95**, 1–40.
7   Z. K. Sweeney, J. L. Salsman, R. A. Andersen and R. G. Bergman, *Angew. Chemie - Int. Ed.*, 2000, **39**, 2339–2343.
8   S. A. Blum, P. J. Walsh and R. G. Bergman, *J. Am. Chem. Soc.*, 2003, **125**, 14276–14277.
9   S. C. Bart, E. Lobkovsky, E. Bill and P. J. Chirik, *J. Am. Chem. Soc.*, 2006, **128**, 5302–5303.
10   D. J. Mindiola and G. L. Hillhouse, *J. Am. Chem. Soc.*, 2001, **123**, 4623–4624.
11   E. Kogut, H. L. Wiencko, L. Zhang, D. E. Cordeau and T. H. Warren, *J. Am. Chem. Soc.*, 2005, **127**, 11248–11249.
12   S. Wiese, M. J. B. Aguila, E. Kogut and T. H. Warren, *Organometallics*, 2013, **32**, 2300–2308.
13   E. R. King, G. T. Sazama and T. A. Betley, *J. Am. Chem. Soc*, 2012, **134**, 17858–17861.
14   M. J. T. Wilding, D. A. Iovan, A. T. Wrobel, J. T. Lukens, S. N. Macmillan, K. M. Lancaster and T. A. Betley, *J. Am. Chem. Soc.*, 2017, **139**, 14757–14766.
15   K. M. Carsch, I. M. DiMucci, D. A. Iovan, A. Li, S. L. Zheng, C. J. Titus, S. J. Lee, K. D. Irwin, D. Nordlund, K. M. Lancaster and T. A. Betley, *Science*, 2019, **365**, 1138–1143.
16   Y. Baek, E. T. Hennessy and T. A. Betley, *J. Am. Chem. Soc*, 2019, **141**, 16944–16953.
17   Y. Baek and T. A. Betley, *J. Am. Chem. Soc.*, 2019, **141**, 7797–7806.
18   S. Bhattacharyya, *J. Chem. Soc. Dalt. Trans.*, 2000, 4677–4682.

19   S. Dey, M. E. Ahmed and A. Dey, *Inorg. Chem.*, 2018, **57**, 5939–5947.

20   P. J. Schebler, C. G. Riordan, I. A. Guzei and A. L. Rheingold, *Inorg. Chem.*, 1998, **37**, 4754–4755.

21   K. E. Rosenkoetter, M. K. Wojnar, B. J. Charette, J. W. Ziller and A. F. Heyduk, *Inorg. Chem.*, 2018, **57**, 9728–9737.

22   B. J. Charette and J. S. Ritch, *Inorg. Chem.*, 2016, **55**, 6344–6350.

23   A. Camerman, *Can. J. Chem.*, 1970, **48**, 179–181.

24   J. J. Warren, T. A. Tronic and J. M. Mayer, *Chem. Rev.*, 2010, **110**, 6961–7001.

25   J. Tao, J. P. Perdew, V. N. Staroverov and G. E. Scuseria, *Phys. Rev. Lett.*, 2003, **91**, 146401.

26   A. Schäfer, C. Huber and R. Ahlrichs, *J. Chem. Phys.*, 1994, **100**, 5829–5835.

27   B. J. Charette, J. W. Ziller and A. F. Heyduk, *Inorg. Chem.*, 2021, **60**, 1579–1589.

28   A. J. Canty, N. Chaichit, B. M. Gatehouse and A. Marker, *Acta Crystallogr. Sect. B*, 1978, **B34**, 3229–3233.

29   B. Valeria Ferretti, P. Gilli and V. Bertolasi, *Acta Crystallogr. Sect. C*, 1992, **C48**, 814–817.

30   R. L. Fanshaw, A. Mobinikhaledi, C. R. Clark and A. G. Blackman, *Inorganica Chim. Acta*, 2000, **307**, 27–32.

31   A. R. Funk, E. Goldberg, E. L. Chang, S. A. Trammell and D. A. Knight, *Dalton Trans.*, 2013, **42**, 15617–15624.

32   M. Sokolov, K. Umakoshi and Y. Sasaki, *Inorg. Chem.*, 2002, **41**, 6237–6243.

33   K. Wieghardt, M. Köppen, W. Swiridoff and J. Weiss, *J. Chem. Soc. Dalt. Trans.*, 1983, 1869–1872.

34   A. Bencini, A. Bianchi, M. Castelló, P. Dapporto, J. Faus, E. Garcia-España, M. Micheloni, P. Paoletti and P. Paoli13, *Inorg. Chem*, 1989, **28**, 99.

35   N. J. Lundin, I. G. Hamilton and A. G. Blackman, *Polyhedron*, 2004, **23**, 97–102.

36   D. G. Lonnon, D. C. Craig and S. B. Colbran, *J. Chem. Soc. Dalt. Trans.*, 2006, 3785–3797.

37   K. Fukui, H. Ohya-Nishiguchi and N. Hirota, *Bull. Chem. Soc. Jpn.*, 1991, **64**, 1205–1212.

38   M. K. Goetz, E. A. Hill, A. S. Filatov and J. S. Anderson, *J. Am. Chem. Soc*, 2018, **140**, 13176–13180.

39   D. M. Jenkins, A. J. Di Bilio, M. J. Allen, T. A. Betley and J. C. Peters, *J. Am. Chem. Soc.*, 2002, **124**, 15336–15350.

40   S. A. Cockle, S. Lindskog and E. Grell, *Biochem. J.*, 1974, **143**, 703–715.

41   D. T. Shay, G. P. A. Yap, L. N. Zakharov, A. L. Rheingold and K. H. Theopold, *Angew. Chemie - Int. Ed.*, 2005, **44**, 1508–1510.

42   L. Zhang, Y. Liu and L. Deng, *J. Am. Chem. Soc*, 2014, **136**, 23.

43   J. Du, L. Wang, M. Xie and L. Deng, *Angew. Chemie - Int. Ed.*, 2015, **54**, 12640–12644.

44   Y. Liu, J. Du and L. Deng, *Inorg. Chem.*, 2017, **56**, 8278–8286.

45   A. Reckziegel, C. Pietzonka, F. Kraus, G. Werncke and C. G. Werncke, *Angew. Chemie Int. Ed.*, 2020, **59**, 8527–8531.

46   D. M. Jenkins, T. A. Betley and J. C. Peters, *J. Am. Chem. Soc.*, 2002, **124**, 11238–11239.

47   X. Hu and K. Meyer, *J. Am. Chem. Soc.*, 2004, **126**, 16322–16323.

48   I. H. Wasbotten and A. Ghosh, *Inorg. Chem.*, 2007, **46**, 7890–7898.

49   R. E. Cowley, R. P. Bontchev, J. Sorrell, O. Sarracino, Y. Feng, H. Wang and J. M. Smith, *J. Am. Chem. Soc.*, 2007, **129**, 2424–2425.

50   R. Tyburski, T. Liu, S. D. Glover and L. Hammarström, *J. Am. Chem. Soc.*, 2021, **143**, 560–576.

51   S. J. Edwards, A. V Soudackov and S. Hammes-Schiffer, *J. Phys. Chem. A*, 2009, **113**, 2117–2126.

52   C. A. Laskowski and G. L. Hillhouse, *Organometallics*, 2009, **28**, 6114–6120.

53   D. W. Shaffer, G. Szigethy, J. W. Ziller and A. F. Heyduk, *Inorg. Chem.*, 2013, **52**, 2110–2118.

54   Z. C. Dai, Y. F. Chen, M. Zhang, S. K. Li, T. T. Yang, L. Shen, J. X. Wang, S. S. Qian, H. L. Zhu and Y. H. Ye, *Org. Biomol. Chem.*, 2015, **13**, 477–486.

55   *SAINT*, Bruker AXS Inc.: Madison, WI,2013.

56   G. M. Sheldrick, *SADABS*, Bruker AXS Inc.: Madison, WI,2014.

57   G. M. Sheldrick, *SHELXTL*, Bruker AXS Inc.: Madison, WI, 2014.

58   *International tables for crystallography. Vol. C: Mathematical, physical and chemical tables*, Kluwer Acad. Publ, Dordrecht, 3. ed., 2004.

59   L. J. Farrugia, *J. Appl. Crystallogr.*, 2012, **45**, 849–854.

60   F. Furche, R. Ahlrichs, C. Hättig, W. Klopper, M. Sierka and F. Weigend, *Wiley Interdiscip. Rev. Comput. Mol. Sci.*, 2014, **4**, 91–100.

61   A. Schäfer, H. Horn and R. Ahlrichs, *J. Chem. Phys.*, 1992, **97**, 2571–2577.

62   W. Humphrey, A. Dalke and K. Schulten, *J. Mol. Graph.*, 1996, **14**, 33–38.

Chapter 4

Exploring ligand-centered hydride and H-atom transfer

4.1 Introduction

It is well established that fundamentally important reactions such as CO_2 and N_2 reduction, water oxidation and H_2 production, and C–H bond functionalization are all transformations that depend on the management of proton and electron inventories. The transfer of one proton and one electron is nominally a hydrogen-atom ($H^\bullet$) transfer reaction (HAT); the transfer of one proton and two electrons is nominally a hydride (H^-) transfer reaction. These types of reactions are often mediated by organic molecules or transition metal complexes. In systems where the transfer of protons and electrons are correlated, the reactions are generally referred to as proton-coupled electron-transfer (PCET) processes.[1–8] Transition-metal based PCET reactions have been studied in detail, strengthening our understanding of the thermodynamic and kinetic factors that control these processes. With the ability to control these factors, stoichiometric and catalytic redox processes can be optimized for maximum yield and efficiency. For example, deliberate positioning of a pendent amine in the secondary coordination sphere of a nickel bis(diphosphine) complex has been shown to facilitate the reduction of O_2.[9] While considerable effort has been devoted to understanding PCET reactions in metal-hydride complexes, more recently, there has been interest in the development of ligand-based systems for PCET reactivity.[10–20] In a ligand-based PCET system, the reservoir for both the proton and the electron(s) is an organic ligand, and the coordination of a metal ion offers a mechanism for controlling the kinetic and thermodynamic parameters that govern the PCET reaction. For example, an organic molecule capable of mediating a PCET reaction would be expected to show an anodic shift in redox potential and an increase in acidity upon binding to a metal center. These changes tune the thermodynamic ability of the molecule to act as an $H^\bullet$ or H^- donor as demonstrated for phenylenediamine coordinated to Al(III).[21,22]

Chapter 2 presented the H-atom transfer ability of a series of complexes with the protonated redox-active $[SN(H)S]^{2-}$ ligand; however, proton storage on a redox-active ligand has been shown previously with the bis(3,5-di-tert-butyl-2-phenoxy)amine $[ON(H)O]^{2-}$ ligand. This ligand, when installed onto zirconium (IV) could effect the four-electron, two-proton reduction of O_2 to hydroxide.[23] The $[ON(H)O]^{2-}$ ligand is an attractive candidate for developing ligand-based PCET reactivity given the well-established redox activity of the ligand in its Lewis basic $[ONO^{cat}]^{3-}$ form. It is also likely that coordination of the $[ON(H)O]^{2-}$ ligand to a metal ion will engender significant acidity to the N–H unit. These two factors prime metal complexes of the $[ON(H)O]^{2-}$ ligand for facile $H^\bullet$ and H^- transfer reactivity.

This Chapter presents the $H^\bullet$ and H^- transfer reactivity of the $[ON(H)O]^{2-}$ ligand when coordinated to nickel. The parent complex, $[ON(H)O]Ni(PPh_3)$, has been prepared and fully characterized. Deprotonation of the parent complex affords the anion, $\{[ONO^{cat}]Ni(PPh_3)\}^{1-}$, which has been structurally characterized as a potassium salt. Acidity and redox potential measurements were used to determine bond dissociation free energy (BDFE) and hydricity (ΔG_{H-}) values for $[ON(H)O]Ni(PPh_3)$ and inspired the study of the corresponding $H^\bullet$ and H^- transfer reactions. The products of $H^\bullet$ and H^- transfer have both been independently prepared and fully characterized and highlight the novel electronic and structural properties that are often observed for transition metal complexes containing redox-active ligands.

4.2 Results

4.2.1 Synthesis and Characterization of K{[ONO^{cat}]Ni(PPh$_3$)} and [ON(H)O]Ni(PPh$_3$)

Square-planar nickel (II) complexes of the bis(3,5-di-*tert*-butyl-2-phenol)amine, $[ONO]H_3$ proligand were readily accessed by simple salt metathesis reactions. Stoichiometric deprotonation of the proligand with appropriate base, either triethylamine or KH, followed by salt metathesis

with NiCl$_2$(PPh$_3$)$_2$, afforded [ON(H)O]Ni(PPh$_3$) and K{[ONO^{cat}]Ni(PPh$_3$)}, respectively, as summarized in **Scheme 4.1**. These new diamagnetic complexes were characterized by ^{1}H NMR spectroscopy, which suggested square-planar four-coordinate geometries with a 1:1 correspondence between the [ONO] and PPh$_3$ ligand resonances. The ^{1}H NMR spectrum of [ON(H)O]Ni(PPh$_3$) included a singlet resonance at 6.19 ppm, assigned to the N–H proton of the [ON(H)O]$^{2-}$ ligand. The complexes were readily distinguished by ^{31}P{^{1}H} NMR spectroscopy with singlet resonances at 15.7 ppm for [ON(H)O]Ni(PPh$_3$) and at 20.5 ppm for K{[ONO^{cat}]Ni(PPh$_3$)}.

Scheme 4.1. **Synthesis of [ON(H)O]Ni(PPh$_3$) and K{[ONO^{cat}]Ni(PPh$_3$)}.**
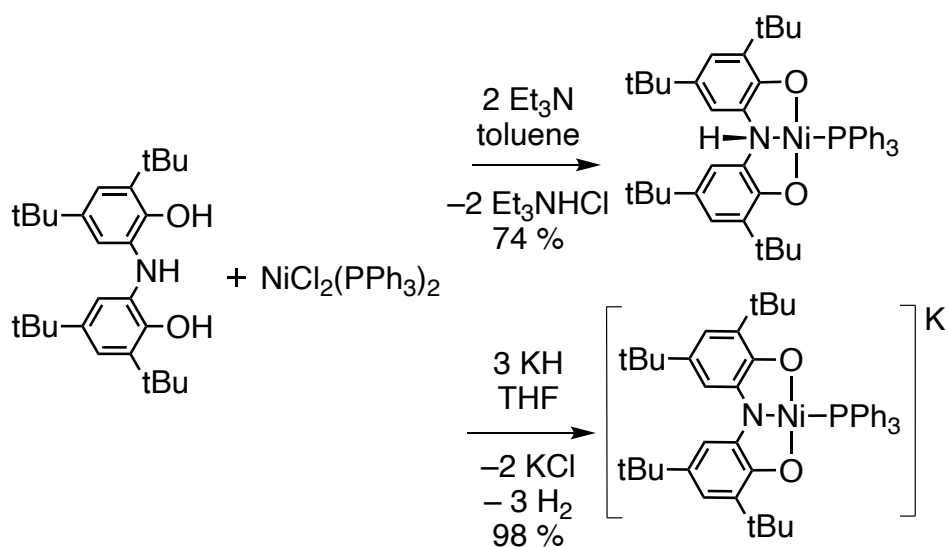
The molecular structures of [ON(H)O]Ni(PPh$_3$) and K{[ONO^{cat}]Ni(PPh$_3$)} were determined by single-crystal X-ray diffraction experiments, each showing four-coordinate, square-planar geometries at nickel. Orange prismatic crystals of [ON(H)O]Ni(PPh$_3$) suitable for diffraction studies were obtained by vapor diffusion of MeCN into a concentrated solution of the complex in Et$_2$O. Green, needle-shaped crystals of K{[ONO^{cat}]Ni(PPh$_3$)} were obtained upon storing a concentrated solution of the salt in MeCN in the presence of the potassium encapsulating

agent 2.2.2-cryptand at –36 °C. **Figures 4.1A** and **4.1B** show the molecular structures of [ON(H)O]Ni(PPh$_3$) and {[ONO^{cat}]Ni(PPh$_3$)}$^{1-}$, respectively, with uncoordinated solvents, counterions, and hydrogen atoms excluded for clarity. Selected bond metrics are reported in **Table 4.1.** Both complexes show square-planar coordination environments with τ_4 values close to zero.[24] The monoanionic {[ONO^{cat}]Ni(PPh$_3$)}$^{1-}$ complex has a calculated metrical oxidation state (MOS)[25] of –2.64, consistent with a reduced [ONO^{cat}]$^{3-}$ ligand coordinated to a nickel(II) metal center. The complexes {[ONO^{cat}]Ni(PPh$_3$)}$^{1-}$ and [ON(H)O]Ni(PPh$_3$) both exhibit typical O–C single bond lengths and delocalized C–C double bonds in the aromatic rings. The anion {[ONO^{cat}]Ni(PPh$_3$)}$^{1-}$ is related to [ON(H)O]Ni(PPh$_3$) by the addition of a proton onto the ligand nitrogen which causes both the M–N and N–C bond lengths to elongate. Additionally, installation of the proton results in a decrease in the bond angles around the [ONO] nitrogen atom. In [ON(H)O]Ni(PPh$_3$), the sum of the non-hydrogen bond angles around nitrogen is 332˚, consistent with sp^3 hybridization at the nitrogen atom.
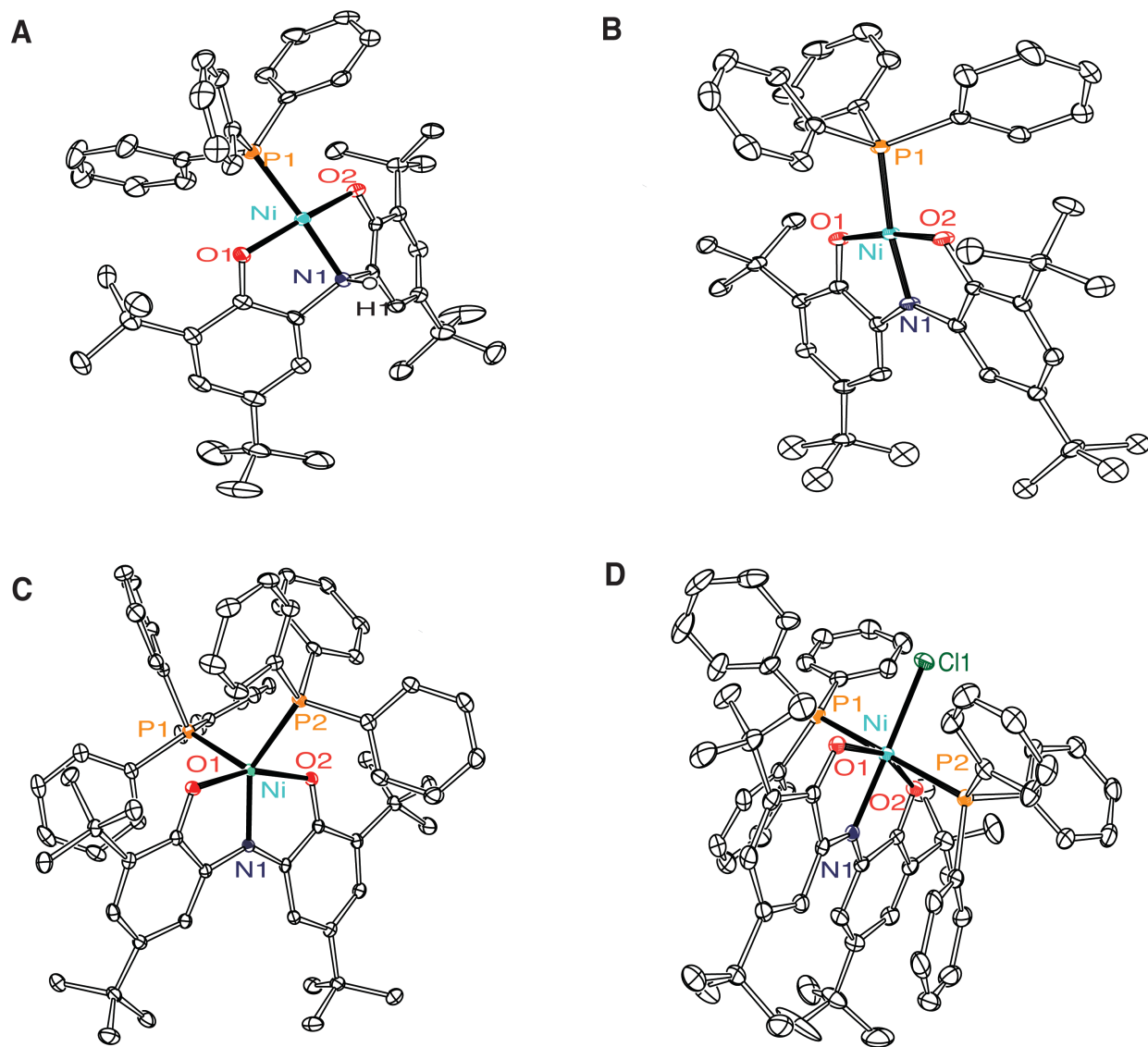
Figure 4.1. ORTEP diagrams of [ON(H)O]Ni(PPh$_3$) (**A**), {[ONO^{cat}]Ni(PPh$_3$)}$^{1-}$ (**B**), [ONO]Ni(PPh$_3$)$_2$ (**C**) and [ONO^q]NiCl(PPh$_3$)$_2$ (**D**) with thermal ellipsoids shown at 50% probability. Hydrogen atoms, K encapsulated with 2.2.2.-cryptand from B and solvent molecules (MeCN for A and B and Et$_2$O for D), have been omitted for clarity.

Table 4.1. Selected bond lengths (Å) and τ values from solid-state structures of [ON(H)O]Ni(PPh$_3$), {[ONO^{cat}]Ni(PPh$_3$)}$^{1-}$, [ONO]Ni(PPh$_3$)$_2$ and [ONO^q]NiCl(PPh$_3$)$_2$.

	[ON(H)O]Ni(PPh$_3$)	{[ONO^{cat}]Ni(PPh$_3$)}$^{1-}$	[ONO]Ni(PPh$_3$)$_2$	[ONO^q]NiCl(PPh$_3$)$_2$
		Bond Lengths (Å)		
Ni–O(1)	1.8583(18)	1.8517(10)	2.0206(11)	2.0596(14)
Ni–O(2)	1.8408(19)	1.8551(10)	2.0675(11)	2.0974(14)
Ni–N(1)	1.947(2)	1.8252(13)	1.9287 (13)	2.0120(17)
Ni–P(1)	2.2150(9)	2.2060(4)	2.3582(5)	2.5046(7)
Ni–P(2)	--	--	2.2898(5)	2.5045(7)
O(1)–C(1)	1.364(3)	1.3489(17)	1.3033(18)	1.276(2)
O(2)–C(8)	1.348(3)	1.3489(17)	1.3005(18)	1.270(2)
N(1)–C(6)	1.482(3)	1.3870(19)	1.378(2)	1.358(3)
N(1)–C(7)	1.477(3)	1.3845(19)	1.370(2)	1.344(3)
τ	0.13[a]	0.10[a]	0.30[b]	--
Calc. MOS	--	-2.64	-1.66	-1.00

[a]$\tau_4 = \dfrac{360°-(\alpha+\beta)}{360°-2\theta}$; [b]$\tau_5 = \dfrac{\beta-\alpha}{60°}$

In order to understand the relationship between the {[ONO^{cat}]Ni(PPh$_3$)}$^{1-}$ anion and [ON(H)O]Ni(PPh$_3$), the protonation reaction was subject to further investigation. The two complexes show different spectroscopic profiles in the 300-400 nm region of the UV-visible spectrum. Portion-wise addition of the weak acid 2,4,6-trimethylpyridinium (pK_a (MeCN) = 14.98)[26] to an acetonitrile solution of {[ONO^{cat}]Ni(PPh$_3$)}$^{1-}$ resulted in the disappearance of the charge transfer band at 363 nm (**Figure 4.2**). This titration data was used to determine a pK_a of 15.3 for the N–H proton of [ON(H)O]Ni(PPh$_3$).[27]
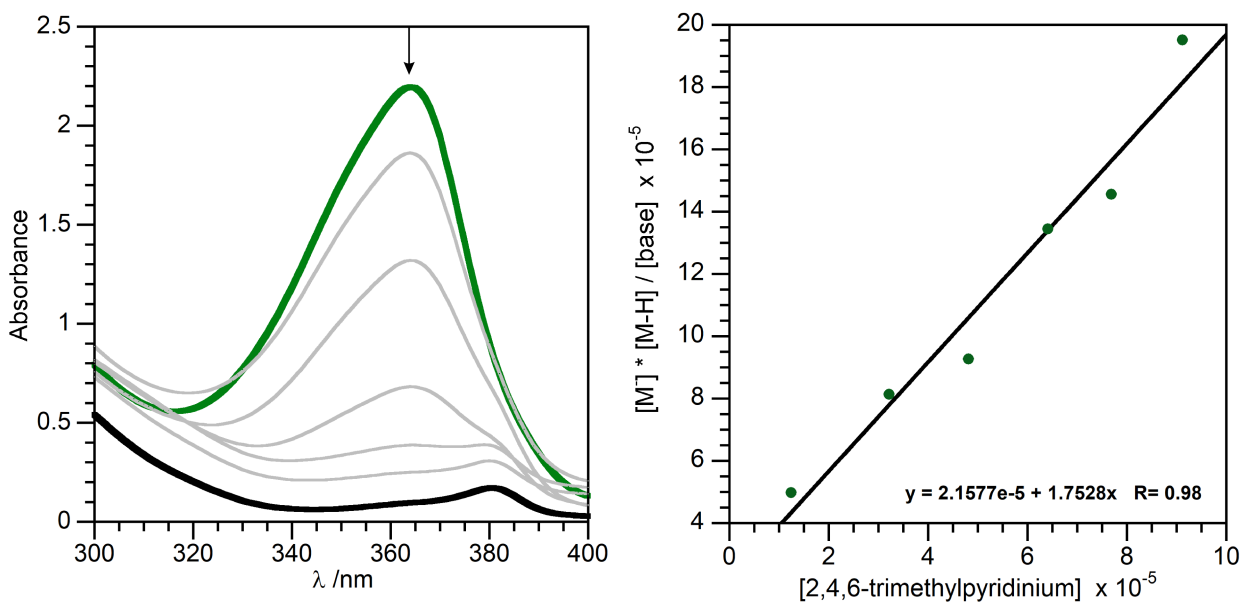
Figure 4.2. (Left) Electronic absorption titration of $\{[ONO^{cat}]Ni(PPh_3)\}^{1-}$ (green) with [2,4,6-collidinium][BF$_4$] affording [ON(H)O]Ni(PPh$_3$) (black) in MeCN. (Right) K$_{eq}$ determination plot using mass balance formulas.

With the well-established redox activity of the [ONO] ligand platform,[28] it also was of interest to probe the redox properties of the $\{[ONO^{cat}]Ni(PPh_3)\}^{1-}$ anion. Data were collected on acetonitrile solutions containing 1 mM analyte and 0.1 M [Bu$_4$N][PF$_6$] as the supporting electrolyte using a standard three-electrode configuration with a glassy carbon working electrode, a platinum wire counter electrode, and a silver wire pseudo-reference electrode. All potentials were referenced to the [Cp$_2$Fe]$^{+/0}$ redox couple using an internal standard added to the cell at the end of the data collection. **Figure 4.3** shows the cyclic voltammogram collected for the $\{[ONO^{cat}]Ni(PPh_3)\}^{1-}$ anion, showing two reversible one-electron oxidations ($i_{pa}/i_{pc} \cong 1$ and E$_a$-E$_c$ = 80 mV) at –0.95 V and –0.49 V and an irreversible reduction a –2.67 V
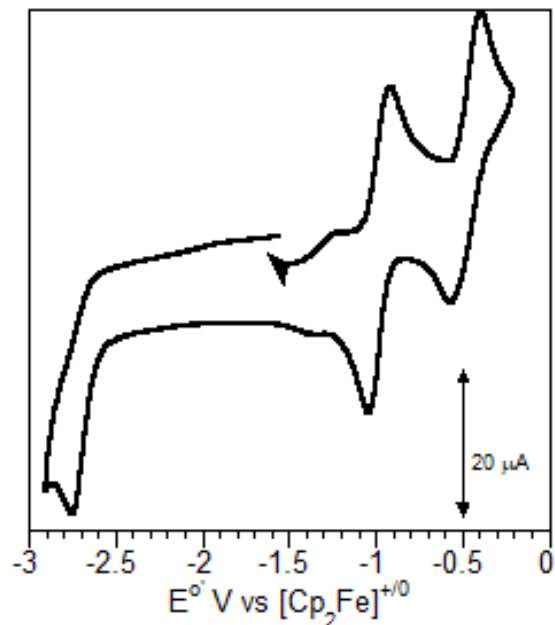
Figure 4.3. Cyclic voltammetry recorded with 1 mM analyte concentration {[ONO^{cat}]Ni(PPh$_3$)}$^{1-}$ with 0.1 M [NBu$_4$][PF$_6$] electrolyte in dry, degassed MeCN under a nitrogen atmosphere using a 3 mm glass carbon working electrode, Pt wire counter electrode and Ag$^{+/0}$ pseudo-reference electrode at room temperature with 200 mV sec-^{1} scan rates.

The pK_a of [ON(H)O]Ni(PPh$_3$) and the redox potentials of {[ONO^{cat}]Ni(PPh$_3$)}$^{1-}$ are state values that can be used to calculate the thermodynamic propensity of [ON(H)O]Ni(PPh$_3$) to serve as either an H$^\bullet$ or an H$^-$ transfer reagent. As shown in **Scheme 4.2**, the N–H pK_a and the first oxidation can be used in **Equation 1.3** to calculate the bond dissociation free energy (BDFE) of the N–H bond.[29,30] The BDFE for the N–H bond of [ON(H)O]Ni(PPh$_3$) was determined to be 54.0±1.5 kcal mol^{-1} in MeCN, using the established value of C$_g$ = 54.9 kcal mol^{-1}.[31]

Similarly, the hydricity of the N–H bond can be calculated using the N–H pK_a and both ligand-based oxidations, as shown in **Scheme 4.2**. **Equation 1.5** gives a hydricity (ΔG$_{H-}$)[20,32] of 67.5±2.0 kcal mol^{-1} for [ON(H)O]Ni(PPh$_3$) in MeCN using the literature value of 79.6 kcal mol^{-1} for ΔG$_{H+/H-}$.[20,33]

Scheme 4.2. Thermodynamic cycle relating pK_a, $E^{\circ\prime(0/-)}$ and $E^{\circ\prime(+/0)}$ to BDFE and ΔG_{H-} for [ON(H)O]Ni(PPh$_3$).
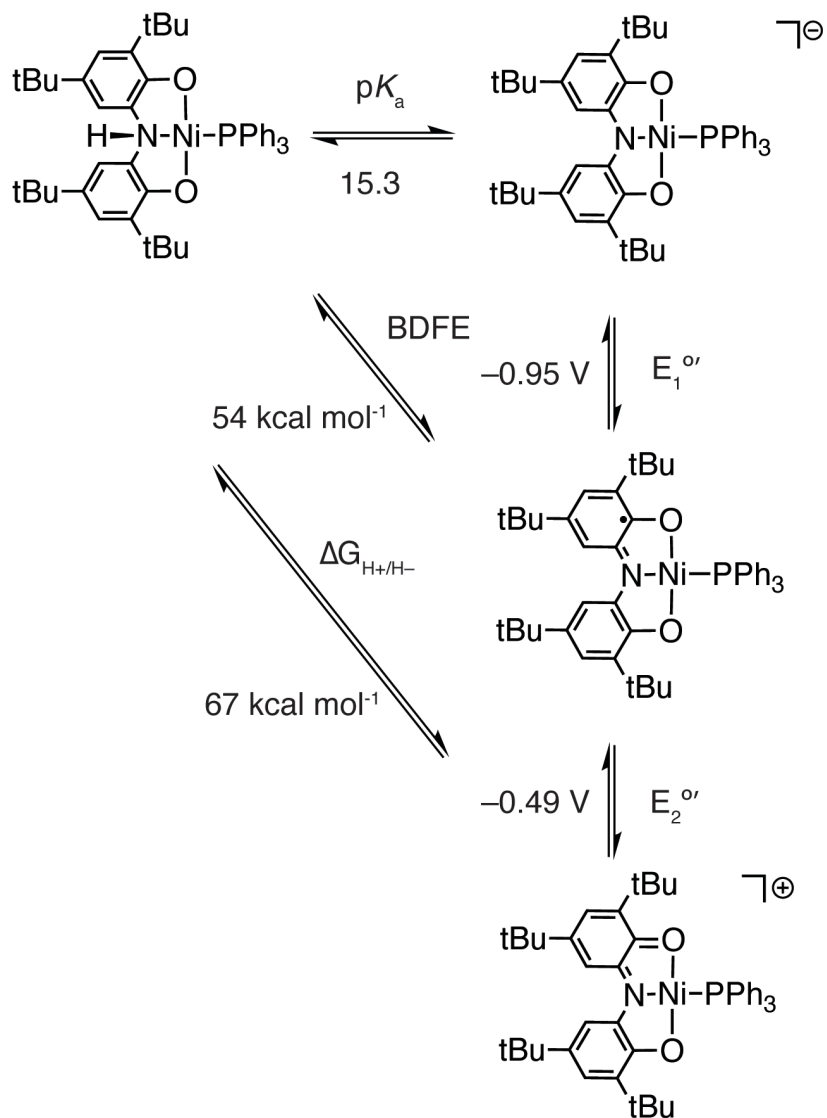
4.2.2 Hydrogen-Atom Transfer Studies.

Similar to the reactivity studies in Chapter 2, to confirm the ability of [ON(H)O]Ni(PPh$_3$) to function as a hydrogen-atom donor, its reactivity with the H$^\bullet$ acceptor TEMPO$^\bullet$ was examined. According to **Scheme 4.3**, [ON(H)O]Ni(PPh$_3$) was treated with one equivalent of TEMPO$^\bullet$ (TEMPO–H BDFE = 66.7 kcal mol^{-1} in MeCN).[31] The reaction proceeded rapidly at room temperature in the presence of one added equivalent of PPh$_3$. **Figure 4.4** shows ^{1}H NMR analysis

of the reaction products showed the formation of TEMPO–H along with paramagnetically-broadened signals in the aromatic region of the spectrum. When the reaction was monitored by UV-vis spectroscopy, the formation of a new nickel species was indicated by the growth of a transition around 600 nm.
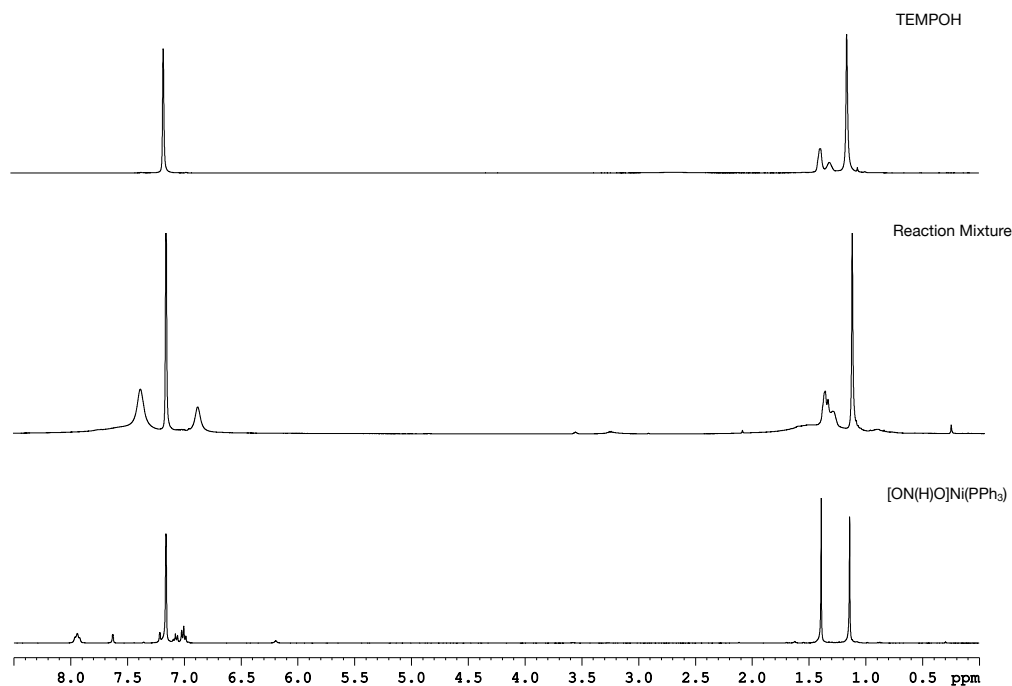
Figure 4.4. ^{1}H NMR spectrum of TEMPOH (top), the reaction of [ON(H)O]Ni(PPh$_3$) with TEMPO$^•$ (middle) and [ON(H)O]Ni(PPh$_3$) (bottom) in C$_6$D$_6$ at 298 K.

Scheme 4.3. Hydrogen-atom transfer reaction from [ON(H)O]Ni(PPh₃) to TEMPO•, synthesis of [ONO]Ni(PPh₃)₂ and equilibrium between [ONO]Ni(PPh₃)₂ and [ONO]Ni(PPh₃).
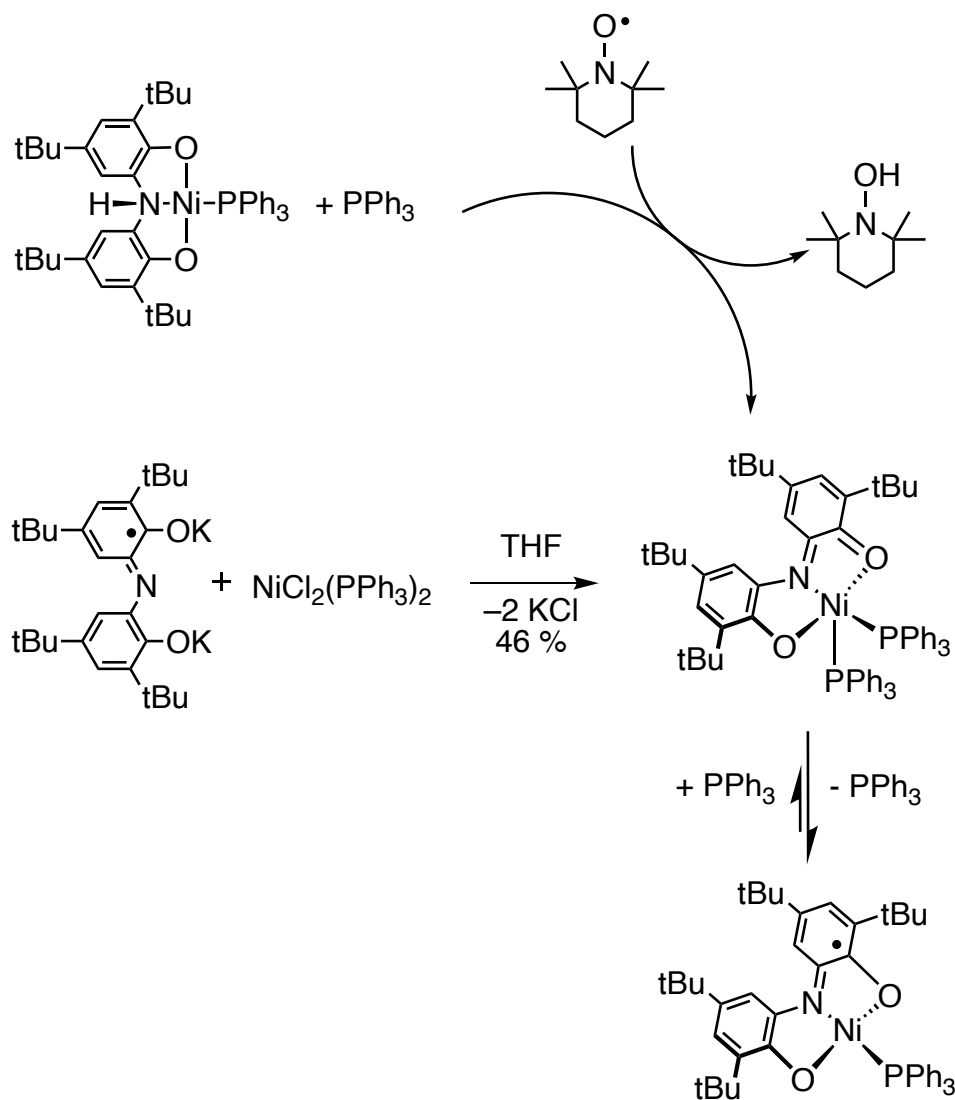
The success of the reaction between [ON(H)O]Ni(PPh₃) and TEMPO• spawned interest in pursuing an alternate synthetic route to the nickel-containing product. Salt metathesis of the singly-oxidized [ONO•]K₂ ligand[34] with NiCl₂(PPh₃)₂ afforded a deep blue reaction mixture. The ¹H NMR spectrum of the product in C₆D₆ showed the same paramagnetically-broadened aromatic resonances observed for the product of the reaction between [ON(H)O]Ni(PPh₃) and TEMPO•.

Single crystals of this reaction product were obtained from a concentrated solution in MeCN at –36 °C. X-ray diffraction studies revealed a five-coordinate, *pseudo*-square-pyramidal nickel complex, [ONO]Ni(PPh$_3$)$_2$, illustrated in **Figure 4.1C.** Selected bond measurements are given in **Table 4.1**. In comparing the structure of [ONO]Ni(PPh$_3$)$_2$ to the {[ONO^{cat}]Ni(PPh$_3$)}$^{1-}$ anion, the N–C and O–C bond distances contract by 0.05 and 0.01 Å, respectively, whereas the metal-heteroatom bond distances elongate by at least 0.1 Å. These changes are all consistent with oxidation of the [ONO] ligand platform.[35] As shown in **Table 4.1**, the calculated MOS value for [ONO]Ni(PPh$_3$)$_2$ is –1.66, which lies in between values expected for [ONO•]$^{2-}$ and [ONO^q]$^{1-}$.

X-band EPR spectroscopy was used to probe the electronic structure and solution behavior of [ONO]Ni(PPh$_3$)$_2$. At 298 K, a benzene solution of [ONO]Ni(PPh$_3$)$_2$ showed a sharp isotropic signal at g = 2.03, consistent with an S = ½ spin system localized on the [ONO] ligand (**Figure 4.5A**). Upon cooling this sample to 77 K, the signal shifted to g = 2.16 and broadened considerably, showing evidence of hyperfine coupling to two different phosphorous atoms with A$_{iso}$(^{31}P) = 50 and 10 MHz (**Figure 4.5B**). One explanation for this behavior would be a dynamic equilibrium between a four-coordinate [ONO•]Ni^{II}(PPh$_3$) complex with a ligand-localized radical (g = 2.03) that is dominant at 298 K and a five-coordinate [ONO^q]Ni^{I}(PPh$_3$)$_2$ complex with a metal-localized radical (g = 2.16) that is dominant at 77 K. This hypothesis was further supported by simulation of the room- and low-temperature EPR spectra. The room-temperature spectrum was best simulated with a 95% contribution from the g = 2.03 species and a 5% contribution from the g = 2.16 species. The low-temperature spectrum was best simulated by a 1% contribution from the g = 2.03 species and a 99% contribution from the g = 2.16 species. To probe further the putative equilibrium between four- and five-coordinate nickel complexes, the room-temperature EPR spectrum of [ONO]Ni(PPh$_3$)$_2$ (33 mM concentration) was obtained in the presence of 100-fold

excess of PPh$_3$. **Figure 4.5C** shows the resulting EPR spectrum, which shows components both at

$g = 2$ .03 and at $g = 2.16$. The data was best simulated with a 10 % contribution from the $g = 2.03$

species and 90 % contribution from the $g = 2.16$ species, suggesting that $K_{eq} \cong 400$ for the

equilibrium between five-coordinate [ONO]Ni(PPh$_3$)$_2$ and four-coordinate [ONO]Ni(PPh$_3$) at 298

K in benzene (**Scheme 4.3**).
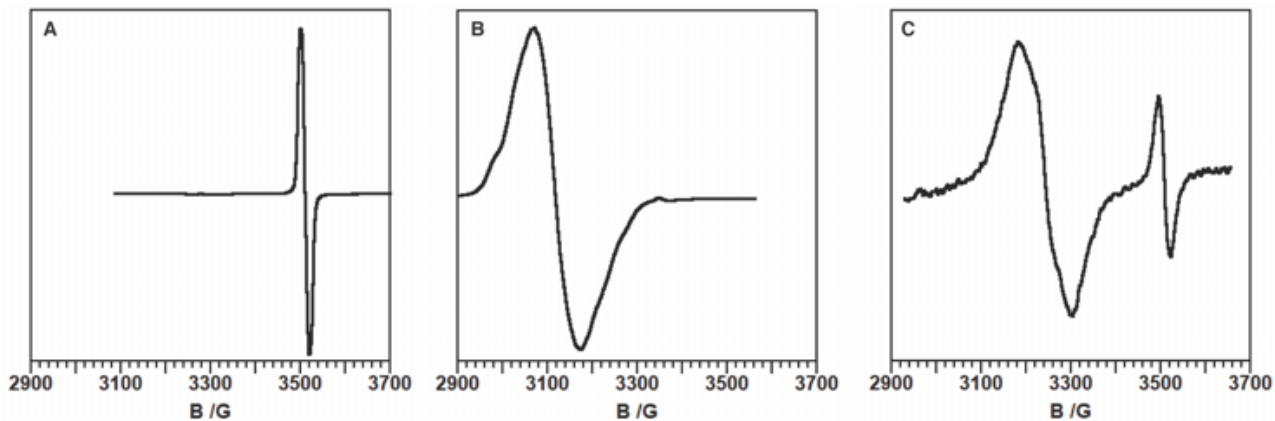
Figure 4.5. X-band EPR spectrum of [ONO]Ni(PPh$_3$)x where x = 1 at 298 K (A) and x = 2 at 77
K (B) and an equilibrium measurement at 298 K in the presence of 100 equivalents of PPh$_3$ (C).

Cyclic voltammetry was used to further assess the solution behavior of [ONO]Ni(PPh$_3$)$_2$.

Figure 4.6 shows the cyclic voltammograms for [ONO]Ni(PPh$_3$)$_2$ in the absence (solid line) and

the presence (dotted line) of excess PPh$_3$. Consistent with the cyclic voltammetry data for

{[ONO^{cat}]Ni(PPh$_3$)}$^{1-}$ presented in **Figure 4.3**, the CV of [ONO]Ni(PPh$_3$)$_2$ without added PPh$_3$

shows a reversible oxidation at –0.51 V, a reversible reduction at –0.95 V, and an irreversible

reduction at –2.65 V. In the presence of added PPh$_3$, the oxidative process shifts by 140 mV to –

0.37 V, consistent with the five-coordinate [ONO]Ni(PPh$_3$)$_2$ complex becoming the dominant

species in solution. The reversible reduction shifts by only 10 mV, consistent with a fast

equilibrium between the four- and five-coordinate species on the electrochemical time scale.

Finally, the irreversible reduction shifts by only 30 mV in the presence of excess PPh$_3$, indicating

that a second PPh$_3$ does not coordinate to the {[ONO^{cat}]Ni(PPh$_3$)}$^{1-}$ anion.
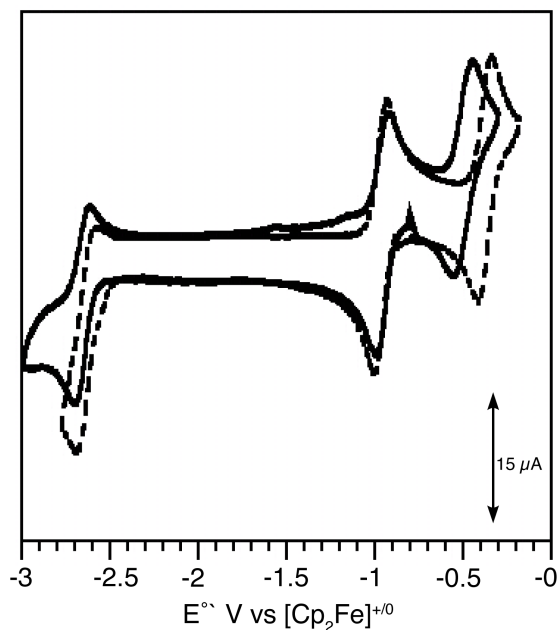
Figure 4.6. Cyclic voltammetry recorded with 1 mM analyte concentration [ONO]Ni(PPh$_3$) (solid line) and 100 mM PPh$_3$ (dotted line), with 0.1 M [NBu$_4$][PF$_6$] electrolyte in dry, degassed MeCN under a nitrogen atmosphere using a 3 mm glass carbon working electrode, Pt wire counter electrode and Ag$^{+/0}$ pseudo-reference electrode at room temperature with 200 mV sec^{-1} scan rates.

To further probe the electronic structures of five-coordinate [ONO]Ni(PPh$_3$)$_2$ and four-coordinate [ONO]Ni(PPh$_3$), density functional theory computations were carried out to investigate these $S = \frac{1}{2}$ nickel complexes. Gas-phase, spin unrestricted, DFT computations were carried out at the TPSS/ def2-TZVP level of theory. The solid-state structure of [ONO]Ni(PPh$_3$)$_2$ was used as the starting point for geometry optimization for the five-coordinate complex; whereas, the solid-state structure of the {[ONO^{cat}]Ni(PPh$_3$)}$^{1-}$ anion was used as the starting point for geometry optimization of the putative four coordinate complex. For the five-coordinate complex, the metal-heteroatom bond distances were within 0.03 Å, and intra-ligand O–C, N–C, and C–C bond distances were within 0.01 Å of the solid-state structure values.

The spin density values for each complex are reported in **Table 4.2,** and spin-density plots for both complexes are shown in **Figure 4.7**. In the four-coordinate complex, the spin-density plot resembles the redox-active π* orbital of the [ONO] ligand. Accordingly, the nickel center only

accounts for 6.7% of the total spin density in the four-coordinate complex, suggesting that this species is best described as a nickel(II) complex with a radical semi-quinonate ligand [ONO•]Ni^{II}(PPh$_3$). In contrast, in the five-coordinate complex, 85.6% of the spin density resides on the nickel center, and the spin-density plot resembles a nickel-based d orbital. Accordingly, the five-coordinate complex is best described as a nickel(I) complex with a fully-oxidized quinonate ligand, [ONO^q]Ni^I(PPh$_3$)$_2$.

Table 4.2. Spin-density for [ONO]Ni(PPh$_3$)$_x$ complexes where x = 1 or 2.
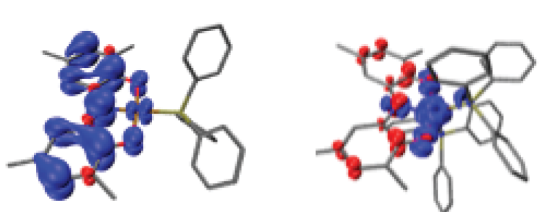
	[ONO•]Ni^{II}(PPh$_3$)	[ONO^q]Ni^I(PPh$_3$)$_2$
Ni	6.7	85.6
O	9.3	8.5
N	29.2	1.2
C	54.8	0.0
P	0.0	5.9

[ONO·]Ni^{II}(PPh$_3$)   [ONO^q]Ni^I(PPh$_3$)$_2$

Figure 4.7. Spin Density plots for four-coordinate [ONO•]Ni(PPh$_3$) (left) and five-coordinate [ONO^q]Ni(PPh$_3$)$_2$ (right) with isovalues 0.0015.

4.2.3 Hydride Transfer Studies.

Given the hydricity value of 67.5 kcal mol^{-1} calculated for [ON(H)O]Ni(PPh$_3$), the ability of this complex to serve as a hydride donor was probed. Treatment of [ON(H)O]Ni(PPh$_3$) with triphenylcarbenium (trityl) triflate (ΔG_{H^-} = 99 kcal mol^{-1} in MeCN)[36] in C$_6$D$_6$ led to the formation of triphenylmethane along with a paramagnetic species, as determined by ^{1}H NMR spectroscopy (**Figure 4.8**). This reaction was monitored by UV-vis spectroscopy, where the growth of low-energy features around 700-900 nm, as typically reported for metal complexes of the [ONO^q]$^{1-}$ ligand, were observed.[37,38] This reaction, as shown in **Scheme 4.4**, was best performed in the presence of one equivalent of PPh$_3$.
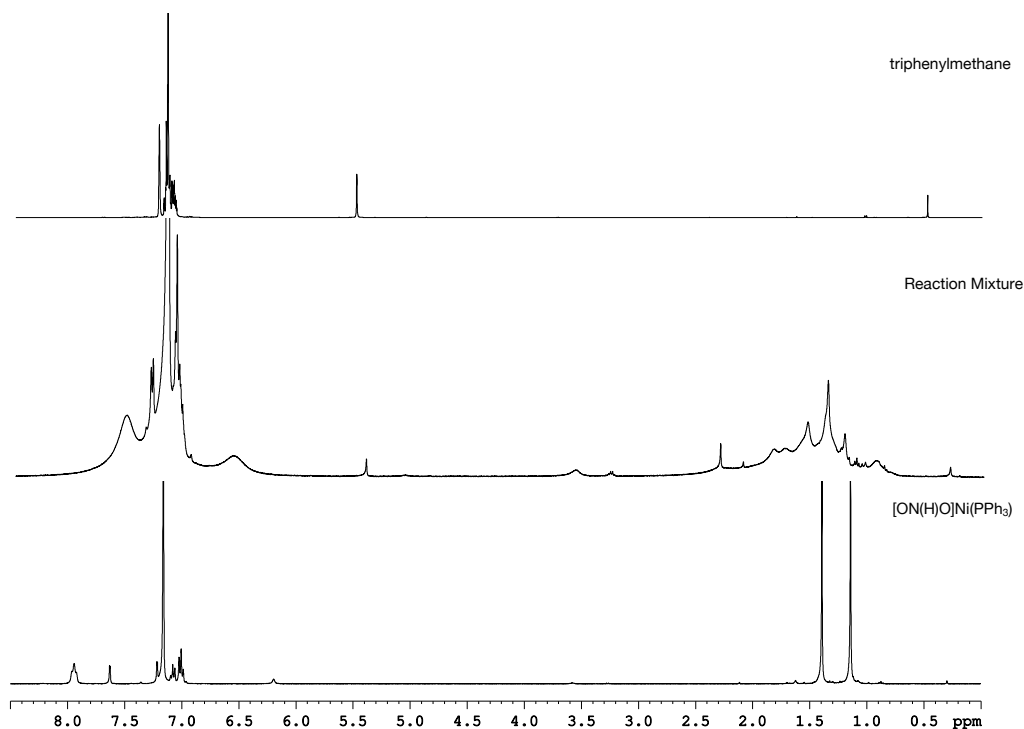
Figure 4.8. ^{1}H NMR Spectrum of triphenyl methane (top), the reaction of [ON(H)O]Ni(PPh$_3$) with trityl triflate (middle) and [ON(H)O]Ni(PPh$_3$) (bottom) in C$_6$D$_6$ at 298 K.

Scheme 4.4. Hydride transfer reaction from [ON(H)O]Ni(PPh₃) to trityl cation and synthesis of [ONO^q]NiX(PPh₃)₂.
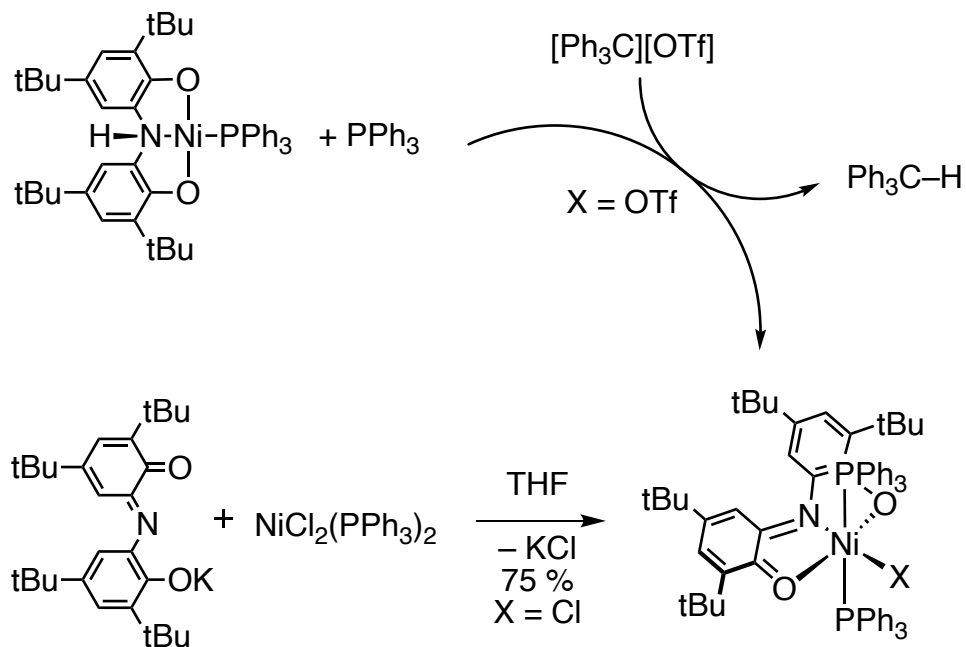
An independent synthetic route to a nickel complex analogous to the product of hydride transfer was sought. The reaction of [ONO^q]K[39] with NiCl$_2$(PPh$_3$)$_2$ in THF afforded a green solution from which a new, paramagnetic nickel product was isolated. Evans' method analysis of the product gave a solution-state magnetic moment (μ_{eff}) of 2.65 μ_B, consistent with an $S = 1$ ground state. Green prismatic crystals of the product were obtained from a concentrated Et$_2$O solution cooled to –36 °C. **Figure 4.1D** shows the structure of [ONO^q]NiCl(PPh$_3$)$_2$, featuring a six-coordinate, trigonal anti-prismatic geometry around the nickel ion. Selected bond distances are reported in **Table 4.1**. Notably, the complex is characterized by short O–C and N–C bond distances, and accordingly, the calculated MOS of the [ONO] ligand is –1.00. The [ONO] ligand maintains a meridional coordination mode with a single chloride located trans to the [ONO] nitrogen, which leaves the two PPh$_3$ ligands trans to one another. All metal-ligand bond distances are over 2 Å, with the Ni–P distances over 2.5 Å. Based on the available data, the complex is postulated to be a high-spin nickel(II) complex, [ONO^q]NiCl(PPh$_3$)$_2$. This proposed electronic structure was further supported by spin-unrestricted gas-phase DFT calculations carried out at the TPSS/ def2-TZVP level of theory. Geometry optimization calculations were carried out starting from the single-crystal X-ray structure and are consistent with structural data. Metal-ligand and intra-ligand bond distances all fall within 0.02 Å and 0.01 Å, respectively, of the solid-state structure. The six-coordinate [ONO^q]NiCl(PPh$_3$)$_2$ complex was described by an $S = 1$, open-shell Kohn-Sham DFT solution with one unpaired electron in d_{z^2} and the other in $d_{x^2-y^2}$. Additionally, the UV-visible spectrum of [ONO^q]NiCl(PPh$_3$)$_2$ is similar to the UV-vis spectrum obtained for the reaction between [ON(H)O]Ni(PPh$_3$) and trityl triflate (**Scheme 4.4**), suggesting that the product of the hydride transfer reaction is [ONO^q]Ni(OTf)(PPh$_3$)$_2$.

4.4 Discussion

The new nickel(II) complex, [ON(H)O]Ni(PPh$_3$), was shown to be capable of serving as both a proton, H$^\bullet$, and H$^-$ donor. Upon coordination to the Lewis-acidic nickel center, the [ON(H)O]$^{2-}$ ligand becomes a reasonable Bronsted acid as the nitrogen takes on ammonium-type character. The acidity of this ligand, coupled with the well-established redox activity of the corresponding [ONO^{cat}]$^{3-}$ form, afford the thermodynamic capacity for [ON(H)O]Ni(PPh$_3$) to serve as an H$^\bullet$ or a H$^-$ donor. BDFE values are commonly used to benchmark the ability of a reagent to donate H$^\bullet$, and the calculated BDFE value of 54 ± 1.5 kcal mol^{-1} for [ON(H)O]Ni(PPh$_3$) is comparable to Group 8 metal carbonyl hydrides.[31,40] Recently, the group reported an analogous [SN(H)S]Ni(PPh$_3$) complex.[41] While this related complex was also capable of serving as an H$^\bullet$ donor, the measured BDFE value was nearly 10 kcal mol^{-1} higher, owing to a nearly 350 mV cathodic shift in the ligand-centered redox potential, highlighting the importance of the ligand-based redox properties to the hydrogen atom transfer reactivity.

In addition to enhanced H$^\bullet$ donor ability, the highly-reducing nature of the [ONO^{cat}]$^{3-}$ ligand enables the [ON(H)O]$^{1-}$ ligand to serve as a H$^-$ donor when coordinated to nickel. The calculated hydricity ($\Delta G^o_{H^-}$) of [ON(H)O]Ni(PPh$_3$) is 67.2 kcal mol^{-1}, which is comparable to the hydricities of a variety of transition metal-hydride complexes, including nickel hydrides with diphosphine ligands that have been employed in proton reduction schemes.[42,43] Recently, a cobalt phenylazopyridine complex was reported that could participate in ligand-centered H$^\bullet$ and H$^-$ transfer reactions; however, in that complex, the attenuated redox properties resulted in significantly higher BDFE and hydricity values, which decreased the donor ability of the cobalt phenylazopyridine complex.[44] These results suggest that further research into ligand-based strategies for H$^\bullet$ and H$^-$ transfer reactions as the tunability of such systems promises the possibility

of designing donors and acceptors with thermodynamic selectivity for a particular reaction. It has been shown in Chapter 2 that for the [SN(H)S]M(PPh$_3$) series, through changing the metal from Pt to Ni, the BDFE of the N–H bond can be lowered by 10 kcal mol^{-1}. By altering the donor atoms from the soft sulfur atoms to harder donors such as oxygen, the analogous [ON(H)O]Ni(PPh$_3$) can lower the BDFE of the N–H bond by an additional 10 kcal mol^{-1}. Therefore, by exploring two simple modifications, a range of 20 kcal mol^{-1} from 54 -73 kcal mol^{-1} has been introduced for these systems.

In addition to the ligand-centered H$^{\bullet}$ and H$^-$ transfer reactivity, the oxidized nickel products, [ONO]Ni(PPh$_3$)$_n$ (n = 1,2) and [ONO^q]NiX(PPh$_3$)$_2$ highlight the interesting electronic structure properties inherent to transition metal complexes containing redox-active ligands. The H$^{\bullet}$ transfer product exists as an equilibrium mixture of four- and five-coordinate complexes in solution. The four-coordinate complex, which is the expected product of H$^{\bullet}$ abstraction from four-coordinate [ON(H)O]Ni(PPh$_3$) in the absence of added PPh$_3$, is best described as a square-planar nickel(II) complex with an [ONO$^{\bullet}$]$^{2-}$ ligand. In the presence of excess PPh$_3$, another ligand binds to the nickel center to give the crystallographically-characterized, five-coordinate complex. Based on EPR and DFT results, this five-coordinate complex is described as predominantly [ONO^q]Ni^I(PPh$_3$)$_2$, with an oxidized [ONO^q]$^{1-}$ ligand and a reduced nickel(I) metal. It is, however, counterintuitive that the binding of a fifth Lewis base to the metal center, which should increase electron density at the metal center, induces an intramolecular electron transfer that reduces the metal and oxidizes the ligand.

Similarly, the product of H$^-$ transfer afforded a surprising example of a high-spin, six-coordinate nickel(II) complex. Formally this nickel complex violates the 18-electron rule; however, the solution magnetic moment, the unusually long metal-ligand bond distances, and the

spin-unrestricted computations are all consistent with this assignment.[45–47] **Figure 4.9** shows the frontier molecular orbitals depiction of the $S = 1$ spin state for the $[ONO^q]Ni^{II}Cl(PPh_3)_2$ complex. The other plausible electronic structure alternatives would be $[ONO^\bullet]Ni^{III}Cl(PPh_3)_2$ and $[ONO^{cat}]Ni^{IV}Cl(PPh_3)_2$. In both of these alternatives, shorter metal-ligand bond lengths would be expected due to the increased charge on the nickel center. Similarly, both of these alternatives would likely conform to $S = 0$ spin states owing to spin pairing between ligand- and metal-localized electrons in $[ONO^\bullet]Ni^{III}Cl(PPh_3)_2$ and to a closed-shell d^6 electron configuration in $[ONO^{cat}]Ni^{IV}Cl(PPh_3)_2$.
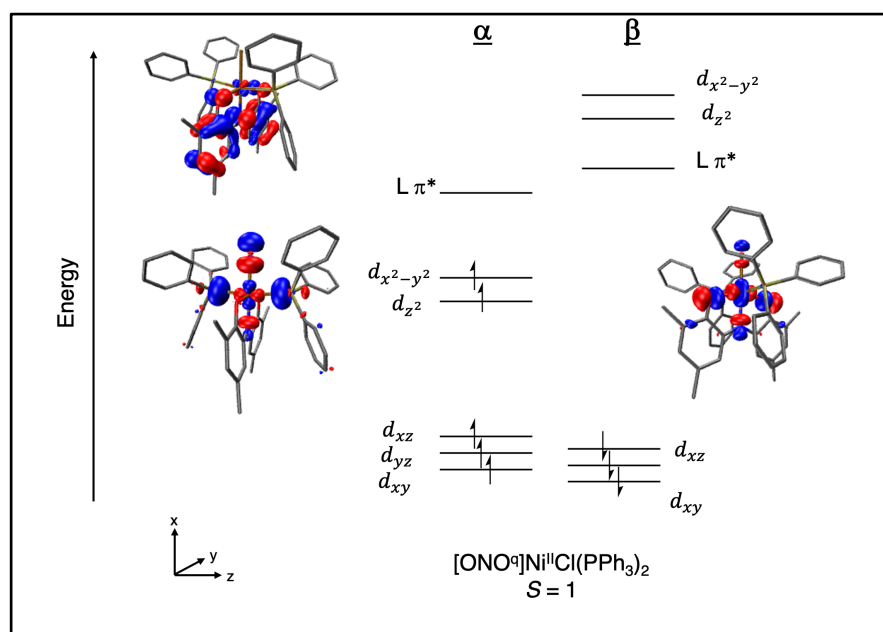
Figure 4.9. Qualitative MO diagram for $[ONO^q]NiCl(PPh_3)_2$ as derived from a spin-unrestricted DFT calculation.

4.5 Conclusion

The preparation and characterization of a new nickel(II) platform bearing a protonated redox-active $[ON(H)O]^{2-}$ ligand is reported. This complex was subject to deprotonation with base to afford the monoanionic $\{[ONO^{cat}]Ni(PPh_3)\}^{1-}$ complex. Additionally, the ability of the protonated species to serve as an H-atom and hydride transfer reagent was probed by reactivity

studies with TEMPO• and trityl cation in the presence of excess PPh$_3$. The H-atom transfer reaction resulted in a five-coordinate [ONO]Ni(PPh$_3$)$_2$ complex, which was synthesized independently and studied for metal-ligand valence tautomerization. The product of the hydride transfer reaction suggested the fully oxidized [ONO^q] ligand can support a nickel (II) in an octahedral environment. This complex was also prepared independently, and its spin state was confirmed to be $S = 1$ through spectroscopic and computational methods. The results of this work set the precedent for the [ON(H)O] ligand to serve as a proton, H-atom, and hydride donor, and further work into employing its use for small molecule activation and substrate reactivity will be pursued.

4.6 Experimental

General Procedures. The compounds and reactions reported below show various levels of air- and moisture- sensitivity; therefore all manipulations were performed using standard Schlenk-line and glovebox techniques. Hydrocarbon and ethereal solvents were sparged with argon before being deoxygenated and dried by passage through Q5 and activated alumina columns, respectively. Halogenated solvents were sparged with argon and passed through two activated alumina columns. Triphenylphosphine and triphenylcarbenium triflate were used as received, and potassium hydride was obtained in mineral oil and washed with pentane prior to use. TEMPO radical was sublimed prior to use. Triethylamine and 2,4,6-collidine were distilled and freeze pump-thawed thrice. The ligands [ONO]H$_3$,[48] [ONO•]K$_2$,[34] [ONO^q]K,[39] and metal precursor NiCl$_2$(PPh$_3$)$_2$[49] were prepared from literature procedures.

Physical Methods. NMR spectra were collected at 298 K on a Bruker Avance 400 MHz or 600 MHz spectrometer in dry, degassed C$_6$D$_6$ or CD$_3$CN. ^{1}H NMR spectra were referenced to tetramethylsilane (TMS) using residual proteo impurities of the solvent (7.16 ppm or 1.93 ppm) and ^{31}P{^{1}H} NMR spectra were referenced with an external standard of phosphoric acid (H$_3$PO$_4$,

85%, 0.00 ppm). All chemical shifts are reported in standard δ notation in parts per million.

Perpendicular-mode X-band EPR spectra were collected at room temperature (9.85 GHz) or 77 K (9.43 GHz) using a Bruker EMX spectrometer equipped with ER041XG microwave bridge. The following spectrometer settings were used: attenuation = 20 dB, microwave power 2.153 mW, frequency = 9.85 or 9.43 GHz, modulation amplitude = 4.00 G, gain = 1.00 x 10^3, conversion time = 4.00 ms, time constant = 0.01 ms, sweep width 5800 G and resolution 15000 points. The spectra were simulated using EasySpin for MATLAB. Electrospray ionization mass-spectrometry (ESI-MS) data were collected on a Waters LCT Premier mass spectrometer using dry, degassed MeOH or C_6H_6. Electronic absorption spectra were recorded using a Jasco V-670 absorption spectrometer in dry, degassed MeCN using a 1-cm path-length cells at ambient temperature (20-24 °C).
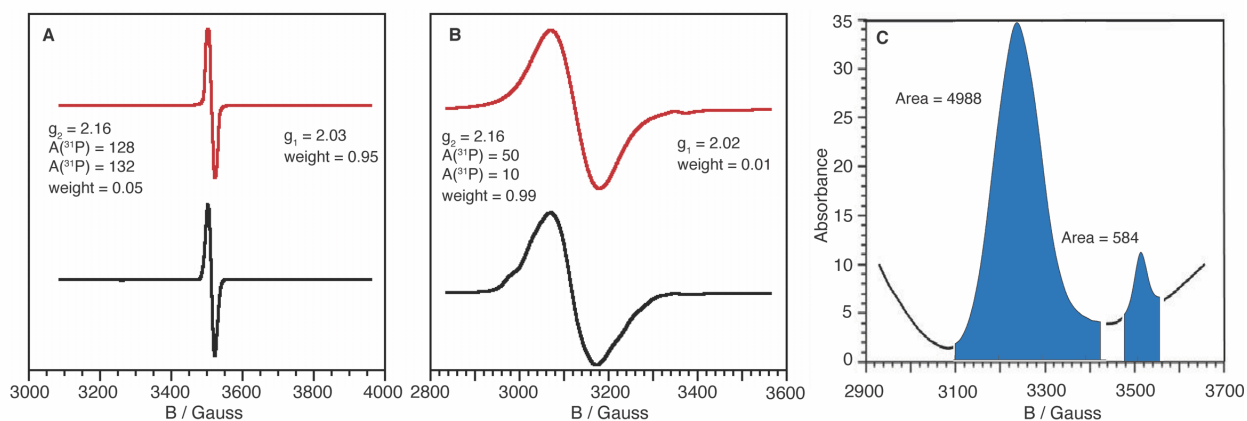
Figure 4.10. X-band EPR spectra (black) and simulation (red) of [ONO•]Ni(PPh$_3$) (A) at 298 K and [ONO^q]Ni(PPh$_3$)$_2$ (B) at 77 K. (C) Areas from integration of EPR spectra from reaction of [ONO•]Ni(PPh$_3$) with 100 equivalents of PPh$_3$ at 298 K.

Electrochemical Methods. Electrochemical experiments were performed on a Gamry series G300 potentiostat/galvanostat/ZRA (Gamry Instruments, Warminster, PA) using a 3.0 mm glassy carbon working electrode, a platinum wire auxiliary electrode and a silver wire pseudo reference electrode. Electrochemical experiments were performed at ambient temperature (20-24 °C) in a nitrogen filled glovebox. Sample concentrations were 1.0 mM in analyte in MeCN containing 0.1

M [NBu$_4$][PF$_6$] as the supporting electrolyte. All potentials are referenced to [Cp$_2$Fe]$^{+/0}$ using ferrocene as an internal standard.[50] Ferrocene were purified by sublimation under reduced pressure and tetrabutylammonium hexafluorophosphate was recrystallized thrice from ethanol and dried under vacuum.

Crystallographic Methods. X-ray diffraction data were collected at low temperature on single crystals covered in Paratone and mounted on glass fibers. Data were acquired using a Bruker SMART APEX II[51] diffractometer equipped with a CCD detector. Measurements were carried out using Mo K$_\alpha$ (λ = 0.71073 Å) radiation, which was wavelength selected with a single-crystal graphite monochromator. A full sphere of data was collected for each crystal structure. The SMART program package was used to determine unit-cell parameters and to collect data. The raw frame data were processed using SAINT[52] and SADABS[53] to yield the reflection data files. Subsequent calculations were carried out using the SHELXTL program suite[54]. Structures were solved by direct methods and refined on F^2 by full-matrix least-squares techniques to convergence. Analytical scattering factors[55] for neutral atoms were used throughout the analyses. Hydrogen atoms, though visible in the difference Fourier map, were generated at calculated positions and their positions refined using the riding model. For [ONO^q]NiCl(PPh$_3$)$_2$, one molecule was located in a general position and one was located on a two-fold rotation axis (Z = 12). There were two molecules of diethyl ether solvent present. One of the solvent molecules was disordered about an inversion center. It was necessary to employ geometric (DFIX) and thermal (SIMU) restraints to refine the disordered solvent molecule. ORTEP diagrams were generated.

Table 4.8. X-ray Diffraction data collection and refinement parameters for [ONO]Ni(PPh₃)₂, K(2.2.2-cryptand){[ONOᶜᵃᵗ]Ni(PPh₃)}, [ON(H)O]Ni(PPh₃) and [ONOᑫ]NiCl(PPh₃)₂.

	[ONO]Ni(PPh₃)₂ • (CH₃CN)	K(2.2.2.-crypt){[ONOᶜᵃᵗ]Ni(PPh₃)}	[ON(H)O]Ni(PPh₃)	[ONOᑫ]NiCl(PPh₃)₂ • (C₄H₁₀O)
empirical formula	C_{64} H_{70} N_1 Ni O_2 P_2 • CH_3CN	C_{64} H_{91} K N_3 Ni O_8 P	C_{46} H_{56} N Ni O_2P	C_{64} H_{70} Cl N Ni O_2 P_2 • $C_4H_{10}O$
formula weight	1046.91	1159.17	744.59	1115.43
crystal system	Monoclinic	Orthorhombic	Triclinic	Monoclinic
space group	$P2_1/c$	$Pbca$	$P\bar{1}$	$C2/c$
T(K)	88(2)	133(2)	88(2)	133(2)
a / Å	23.0043(10)	22.0373(18)	13.826(2)	38.546(5)
b / Å	13.7264(6)	23.1668(19)	17.630(3)	19.817(3)
c / Å	18.3598(8)	24.0515(19)	27.389(5)	24.323(3)
α / deg	90	90	106.093(3)	90
β / deg	100.4739(6)	90	90.149(3)	100.0803(1)
γ / deg	90	90	105.698(3)	90
V / Å³	5700.8(4)	12279.1(17)	6153.5(18)	18293(4)
Z	4	8	6	12
refl. collected	68430	143958	76245	99206
indep. refl.	13571 [R(int) = 0.0514]	15492 [R(int) = 0.0596]	25190 [R(int) = 0.0833]	18709 [R(int) = 0.0695]
R1 ($I > 2\sigma$)[a]	0.0355 (0.0574)	0.0366 (0.056)	0.0535 (0.1019)	0.0433 (0.0598)
wR2 (all data)[b]	0.0717 (0.0791)	0.0812 (0.0896)	0.1011 (0.1147)	0.1046(0.1151)
GOF	1.004	1.032	1.003	1.015

[a]R1 = Σ||F₀|–|F𝒸||/Σ|F₀|; [b]wR2 = [Σ[w(F₀²–F𝒸²)²]/Σ[w(F₀²)²]]^½

Theoretical Calculations. All calculations were performed with TURBOMOLE 7.3.1[56] using the non-empirical TPSS meta-generalized-gradient-approximation (meta-GGA) functional. For computational efficiency, initial geometry optimizations were performed using moderate split-valence plus polarization basis sets (def2-SVP) and then refined using bases sets of triple-valence plus polarizations (def2-TZVP) quality.[57] Atomic coordinates from the solid-state structures obtained from X-ray diffraction experiments were used as starting points for the geometry optimization no molecular symmetry was imposed. Molecular geometries and orbital energies were evaluated self-consistently to tight convergence criteria (energy converged to 0.1 µHartree; maximum norm of the Cartesian gradient <10⁻⁴ au). Molecular orbital images were rendered using Visual Molecular Dynamics (VMD 1.9.3) software.[58]

p*K*ₐ Measurements. The p*K*ₐ value was determined by spectrophotometric titration following published methods.[27] Aliquots (200µL) were removed from a MeCN stock solution of metal

complex and a series of varying volumes of 2,4,6-trimethylpyridine were added using a volumetric syringe and these solutions were diluted to 5 mL. Spectra changes were monitored between samples with a Jasco V-670 absorption spectrometer in 10 mm quartz cuvettes.

Synthesis of [ONO]Ni(PPh₃)₂. In a 20 mL scintillation vial in a nitrogen glovebox atmosphere, a solution of [ONO·]K₂ (262 mg, 0.52 mmol, 1.0 equiv.) in THF (10 mL) was added to a solution of purple NiCl₂(PPh₃)₂ (343 mg, 0.52 mmol, 1.0 equiv.) in THF (5 mL). The dark blue solution was stirred at room temperature for 1 day, then was filtered through Celite using a medium porous fritted funnel and washed with THF (30 mL). The filtrate volatiles were concentrated to 5 mL then layered with 10 mL MeCN and placed in the freezer overnight to afford blue needle-like crystals in 46 % (241 mg) yield. X-ray quality crystals were obtained by a concentrated solution of the complex in MeCN at –36 °C. Anal. Calcd. $C_{64}H_{70}NNiO_2P_2$•KCl: C, 71.15; H, 6.53; N, 1.30. Found C, 71.33; H, 6.54; N, 1.14. MS (ESI⁺) (C_6H_6) m/z: 743.3 (MH⁺).

Synthesis of K{[ONOᶜᵃᵗ]Ni(PPh₃)}. In a 100 mL round bottom flask in a nitrogen glovebox atmosphere, a solution of [ONO]H₃ (650 mg, 1.53 mmol, 1.0 equiv.) in THF (20 mL) was deprotonated using KH (183 mg, 4.58 mmol, 3.0 equiv.) to yield an immediate white precipitate and the evolution of gas (H₂). Once the gas ceased, the purple solution was frozen. Concurrently, purple NiCl₂(PPh₃)₂ (1000 mg, 1.53 mmol, 1.0 equiv.) was dissolved THF (20 mL) then frozen. Upon thawing, the solutions were combined and an immediate color change to deep blue/purple was observed. The reaction stirred at room temperature for 1 day, when the green solution was filtered through Celite using a medium porous fritted funnel and washed with 50 mL THF. The filtrate volatiles were concentrated to 5 mL and precipitated with 50 mL of pentane. The green solid was isolated in a 98 % (1.29 g) yield. Suitable crystals for diffraction were obtained from a concentrated solution of analyte with 2.2.2.-cryptand in MeCN at –36 °C. Anal. Calcd.

$C_{46}H_{55}NNiO_2P$(2.2.2-cryptand)•KCl: C, 62.31; H, 7.43; N, 3.41. Found C, 62.16; H, 7.34; N, 3.46. ^{1}H NMR (CD$_3$CN, 400 MHz) δ/ppm : 7.91 (br, 6H, aryl-H), 7.40 (br, 9H, aryl-H), 7.30 (br, 2H, aryl-H), 6.21 (br, 2H, aryl-H), 1.31 (s, 18H, -C(CH$_3$), 0.97(s, 18H, - C(CH$_3$)$_3$. ^{31}P{^{1}H} NMR (162 MHz, C$_6$D$_6$) δ/ppm: 20.5. λ_{max} / nm (ε/ M^{-1}cm^{-1}): 360 (26500). MS (ESI$^+$) (C$_6$H$_6$) m/z: 743.3 (MH$^+$).
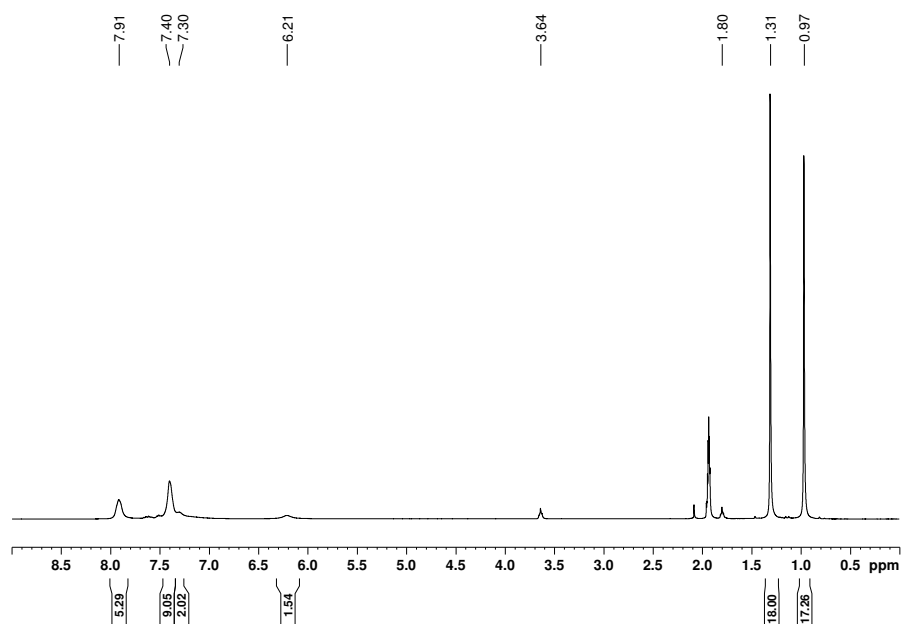
Figure 4.11. ^{1}H NMR Spectrum K{[ONO^{cat}]Ni(PPh$_3$)} in CD$_3$CN at 298 K.
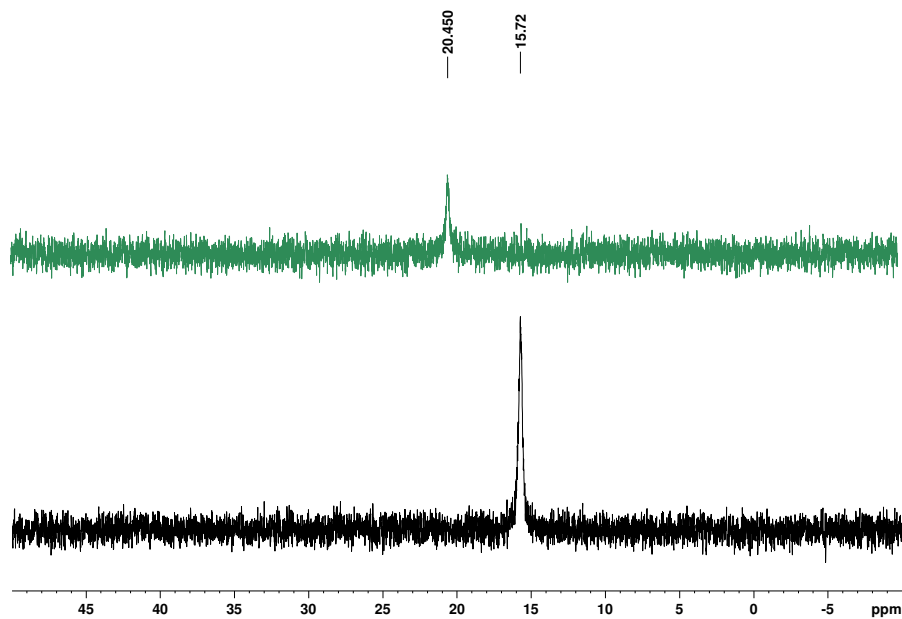
Figure 4.12. ^{31}P{^{1}H} NMR spectra of K{[ONO^{cat}]Ni(PPh$_3$)} (green) and [ON(H)O]Ni(PPh$_3$) (black) in C$_6$D$_6$ at 298 K.

Synthesis of [ON(H)O]Ni(PPh₃). In a 20 mL scintillation vial in a nitrogen glovebox atmosphere, a solution of [ONO]H₃ (508 mg, 1.20 mmol, 1.0 equiv.) in toluene (5 mL) was deprotonated using Et₃N (333 μL, 2.40 mmol, 2.0 equiv.) then frozen in cold well. Concurrently, purple NiCl₂(PPh₃)₂ (782 mg, 1.20 mmol, 1.0 equiv.) was dissolved in toluene (10 mL) then frozen. Upon thawing, the solutions were combined and an immediate color change to dark purple then dark blue was observed. The reaction stirred at room temperature for 1 day, then was filtered through Celite using a medium porous fritted funnel and washed with toluene (30 mL). The filtrate volatiles were removed and the blue solid was re-dissolved in 10 mL MeCN and placed in the freezer overnight to afford a green solid. The solid was collected in a 74 % (566 mg) yield. Suitable crystals for diffraction were grown from vapor diffusion of a concentration solution of analyte in Et₂O into MeCN. Anal. Calcd. $C_{46}H_{56}NNiO_2P \cdot KCl$: C, 67.45; H, 6.89; N, 1.71. Found C, 67.19; H, 6.75; N, 1.69. ^1H NMR (C_6D_6, 400 MHz) δ/ppm : 7.91-7.86 (t, 6H, J = 9.49 Hz, aryl-H), 7.58-7.57 (d, 2H, J = 1.64 Hz, aryl-H), 7.16 (d, 2H, J = 2.00 Hz, aryl-H), 7.02-7.01 (d, 3H, J = 7.40 Hz, aryl-H), 6.97-6.93 (t, 6H, J = 7.68 Hz, aryl-H), 6.14 (s, 1H, N–H), 1.34 (s, 18H, -C(CH₃)₃, 1.09 (s, 18H, - C(CH₃). $^{31}P\{^1H\}$ NMR (162 MHz, C_6D_6) δ/ppm: 15.6. UV-vis (C_6H_6) λ_{max} / nm (ε/ $M^{-1}cm^{-1}$): 380 (1400). MS (ESI⁺) (THF) m/z: 743.3 (M⁺).
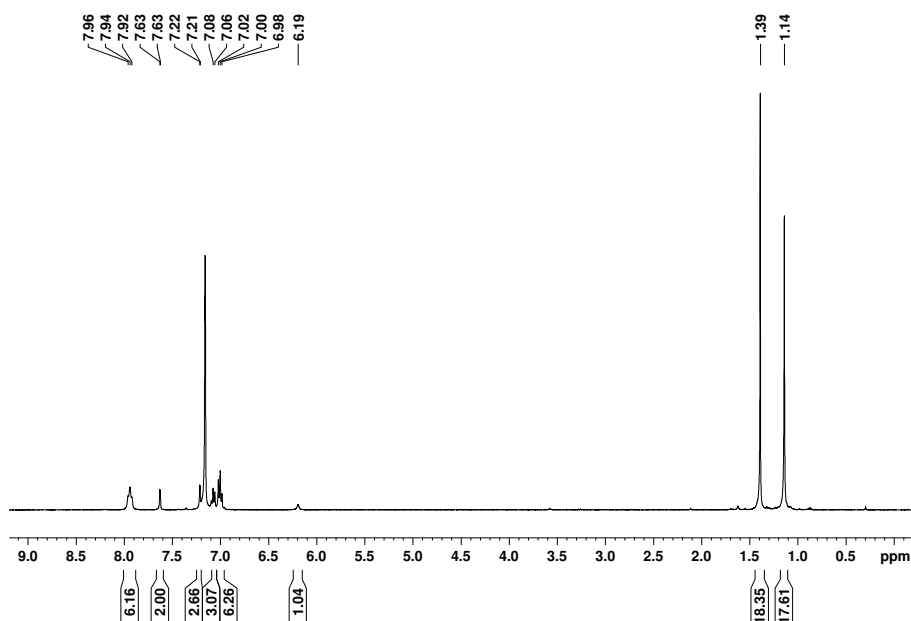
Figure 4.13. ^{1}H NMR Spectrum [ON(H)O]Ni(PPh$_3$) in C$_6$D$_6$ at 298 K.

Synthesis of [ONO^q]NiCl(PPh$_3$)$_2$. In a 250 mL round bottom flask in a nitrogen glovebox atmosphere, a solution of black [ONO^q]K (608 mg, 1.53 mmol, 1.0 equiv.) in THF (50 mL) was added to a purple NiCl$_2$(PPh$_3$)$_2$ (854 mg, 1.53 mmol, 1.0 equiv.) suspension in THF (50 mL). The reaction stirred at room temperature for 3 hours, then was filtered through Celite using a medium porous fritted funnel. The filtrate volatiles were removed, re-dissolved in minimal THF and co-evaporated with pentane to afford a green solid. The solid was collected in a 75 % (1.19 mg) yield. X-ray quality crystals were obtained from a concentrated solution of analyte Et$_2$O at –36°C. μ_{eff}: 2.65 μ_B (298 K). Anal. Cald. C$_{64}$H$_{70}$ClNNiO$_2$P$_2$: C, 73.82; H, 6.78; N, 1.35. Found C, 73.85; H, 6.49; N, 1.17. UV-vis (MeCN) λ_{max} / nm (ε/ M^{-1}cm^{-1}): 380 (3600), 430 (2300), 595 (1200), 755 (4300), 815 (4400). MS (ESI+) (MeOH) m/z: 1037.5 (M+).

4.7 References

1   Roth, J. P.; Yoder, J. C.; Won, T.-J.; Mayer, J. M. *Science* **2001**, *294*, 2524–2526.
2   Dhuri, S. N.; Lee, Y.-M.; Seo, M. S.; Cho, J.; Narulkar, D. D.; Fukuzumi, S.; Nam, W. *Dalton Trans.* **2015**, *44*, 7634–7642.
3   Mayer, J. M. *Acc. Chem. Res.* **2011**, *44*, 36–46.
4   Hu, Y.; Norton, J. R. *J. Am. Chem. Soc.* **2014**, *136*, 5938–5948.
5   Gardner, K. A.; Mayer, J. M. *Science* **1995**, *269*, 1849–1851.
6   Thammavongsy, Z.; Mercer, I. P.; Yang, J. Y. *Chem. Commun.* **2019**, *55*, 10342–10358.
7   Cukier, R. I.; Nocera, D. G. *Annu. Rev. Phys. Chem.* **1998**, *49*, 337–369.
8   Hammes-Schiffer, S. *J. Am. Chem. Soc.* **2015**, *137*, 8860–8871.
9   Yang, J. Y.; Bullock, R. M.; Dougherty, W. G.; Kassel, W. S.; Twamley, B.; Dubois, D. L.; Rakowski Dubois, M. *Dalton Trans.* **2010**, *39*, 3001–3010.
10 Raugei, S.; Chen, S.; Ho, M.-H.; Ginovska-Pangovska, B.; Rousseau, R. J.; Dupuis, M.; DuBois, D. L.; Bullock, R. M. *Chem. – A Eur. J.* **2012**, *18*, 6493–6506.
11 Cappellani, E. P.; Drouin, S. D.; Jia, G.; Maltby, P. A.; Morris, R. H.; Schweitzer, C. T. *J. Am. Chem. Soc.* **1994**, *116*, 3375–3388.
12 Henthorn, J. T.; Lin, S.; Agapie, T. *J. Am. Chem. Soc.* **2015**, *137*, 1458–1464.
13 Curtis, C. J.; Miedaner, A.; Raebiger, J. W.; DuBois, D. L. *Organometallics* **2004**, *23*, 511–516.
14 Rountree, E. S.; Dempsey, J. L. *Inorg. Chem.* **2016**, *55*, 5079–5087.
15 Curtis, C. J.; Miedaner, A.; Ellis, W. W.; DuBois, D. L. *J. Am. Chem. Soc.* **2002**, *124*, 1918–1925.
16 Ellis, W. W.; Miedaner, A.; Curtis, C. J.; Gibson, D. H.; DuBois, D. L. *J. Am. Chem. Soc.* **2002**, *124*, 1926–1932.
17 Kumar, N.; Camaioni, D. M.; Dupuis, M.; Raugei, S.; Appel, A. M. *Dalton Trans.* **2014**, *43*, 11803–11806.
18 Bourrez, M.; Steinmetz, R.; Ott, S.; Gloaguen, F.; Hammarström, L. *Nat. Chem.* **2015**, *7*, 140–145.
19 Milsmann, C.; Semproni, S. P.; Chirik, P. J. *J. Am. Chem. Soc.* **2014**, *136*, 12099–12107.
20 Wiedner, E. S.; Chambers, M. B.; Pitman, C. L.; Bullock, R. M.; Miller, A. J. M.; Appel, A. M. *Chem. Rev.* **2016**, *116*, 8655–8692.
21 Berben, L. A. *Chem. – A Eur. J.* **2015**, *21*, 2734–2742.
22 Thompson, E. J.; Berben, L. A. *Angew. Chemie Int. Ed.* **2015**, *54*, 11642–11646.
23 Lu, F.; Zarkesh, R. A.; Heyduk, A. F. A *Eur. J. Inorg. Chem.* **2012**, *3*, 467–470.
24 Yang, L.; Powell, D. R.; Houser, R. P. *Dalton Trans.* **2007**, *9*, 955–964.
25 Brown, S. N. *Inorg. Chem.* **2012**, *51*, 1251–1260.
26 Kolomeitsev, A. A.; Koppel, I. A.; Rodima, T.; Barten, J.; Lork, E.; Röschenthaler, G.-V.; Kaljurand, I.; Kütt, A.; Koppel, I.; Mäemets, V.; Leito, I. *J. Am. Chem. Soc.* **2005**, *127*, 17656–17666.
27 Albers, A.; Demeshko, S.; Dechert, S.; Saouma, C. T.; Mayer, J. M.; Meyer, F. *J. Am. Chem. Soc.* **2014**, *136*, 3946–3954.
28 Phalguni, C.; Hess, M.; Hildenbrand, K.; Bill, E.; Thomas, W.; Wieghardt, K. *Inorg. Chem.* **1999**, *38*, 2781–2790.
29 Bordwell, F. G.; Cheng, J. P.; Harrelson, J. A. *J. Am. Chem. Soc.* **1988**, *110*, 1229–1231.
30 Tilset, M.; Parker, V. D. S. *J. Am. Chem. Soc.* **1989**, *111*, 6711–6717.
31 Warren, J. J.; Tronic, T. A.; Mayer, J. M. *Chem. Rev.* **2010**, *110*, 6961–7001.

32   Berning, D. E.; Noll, B. C.; DuBois, D. L. *J. Am. Chem. Soc.* **1999**, *121*, 11432–11447.

33   Sasayama, A. F.; Kubiak, C. P.; Waldie, K. M.; Ostericher, A. L.; Reineke, M. H. *ACS Catal.* **2018**, *8*, 1313–1324.

34   Wong, J. L.; Higgins, R. F.; Bhowmick, I.; Cao, D. X.; Szigethy, G.; Ziller, J. W.; Shores, M. P.; Heyduk, A. F. *Chem. Sci.* **2016**, *7*, 1594–1599.

35   McGarvey, B. R.; Ozarowski, A.; Tian, Z.; Tuck, D. G. *Can. J. Chem.* **1995**, *73*, 1213–1222.

36   Matsubara, Y.; Fujita, E.; Doherty, M. D.; Muckerman, J. T.; Creutz, C. *J. Am. Chem. Soc.* **2012**, *134*, 15743–15757.

37   Hollas, A. M.; Ziller, J. W.; Heyduk, A. F. *Polyhedron* **2018**, *143*, 111–117.

38   Hananouchi, S.; Krull, B. T.; Ziller, J. W.; Furche, F.; Heyduk, A. F. *Dalton Trans.* **2014**, *43*, 17991–18000.

39   Szigethy, G.; Shaffer, D. W.; Heyduk, A. F. *Inorg. Chem.* **2012**, *51*, 12606–12618.

40   Moore, E. J.; Sullivan, J. M.; Norton, J. R. *J. Am. Chem. Soc.* **1986**, *108*, 2257–2263.

41   Rosenkoetter, K. E.; Wojnar, M. K.; Charette, B. J.; Ziller, J. W.; Heyduk, A. F. *Inorg. Chem.* **2018**, *57*, 9728–9737.

42   Yang, J. Y.; Bullock, R. M.; Shaw, W. J.; Twamley, B.; Fraze, K.; DuBois, M. R.; DuBois, D. L. *J. Am. Chem. Soc.* **2009**, *131*, 5935–5945.

43   Berning, D. E.; Miedaner, A.; Curtis, C. J.; Noll, B. C.; Rakowski DuBois, M. C.; DuBois, D. L. *Organometallics* **2001**, *20*, 1832–1839.

44   McLoughlin, E. A.; Waldie, K. M.; Ramakrishnan, S.; Waymouth, R. M. *J. Am. Chem. Soc.* **2018**, *140*, 13233–13241.

45   Han, Z.; Shen, L.; Brennessel, W. W.; Holland, P. L.; Eisenberg, R. *J. Am. Chem. Soc.* **2013**, *135*, 14659–14669.

46   Rosenfield, S. G.; Berends, H. P.; Gelmini, L.; Stephan, D. W.; Mascharak, P. K. *Inorg. Chem.* **1987**, *26*, 2792–2797.

47   Lee, S. E.; Nasirian, A.; Kim, Y. E.; Fard, P. T.; Kim, Y.; Jeong, B.; Kim, S.-J.; Baeg, J.-O.; Kim, J. *J. Am. Chem. Soc.* **2020**, *142*, 19142–19149.

48   Zarkesh, R. A.; Ziller, J. W.; Heyduk, A. F. *Angew. Chemie Int. Ed.* **2008**, *47*, 4715–4718.

49   Busby, R.; Hursthouse, M. B.; Jarrett, P. S.; Lehmann, C. W.; Malik, K. M. A.; Phillips, C. *J. Chem. Soc. Dalt. Trans.* **1993**, 3767–3770.

50   Connelly, N. G.; Geiger, W. E. *Chem. Rev.* **1996**, *96*, 877–910.

51   APEX2. 2014.11-0. Bruker, AXS, Inc.: Madison, WI 2014.

52   SAINT. SAX Area-Detector Integration Program,. 7.34a. Bruker, AXS, Inc.: Madison, WI 2013.

53   Sheldrick, G. M. SADABS. *SADABS*. 2014/4. Bruker, AXS, Inc.: Madison, WI 2014.

54   Sheldrick, G. M. SHELXTL. Bruker, AXS, Inc.: Madison, WI 2014.

55   *International Tables for Crystallography. Vol. C: Mathematical, Physical and Chemical Tables*, 3. ed.; Kluwer Acad. Publ: Dordrecht, 2004.

56   Furche, F.; Ahlrichs, R.; Hättig, C.; Klopper, W.; Sierka, M.; Weigend, F. Turbomole. *Wiley Interdiscip. Rev. Comput. Mol. Sci.* **2014**, *4*, 91–100.

57   Schäfer, A.; Huber, C.; Ahlrichs, R. *J. Chem. Phys.* **1994**, *100*, 5829–5835.

58   Humphrey, W.; Dalke, A.; Schulten, K. *J. Mol. Graph.* **1996**, *14*, 33–38.

Chapter 5

Investigations into a redox-active ligand facilitated nickel-imido complex and its catalytic

nitrene transfer to isocyanide

5.1 Introduction

Group transfer in late first-row transition metal complexes continues to garner attention with a growing number of examples with cobalt, nickel, and copper.[1–10] Nitrogen or N–group transfer is typically thought to occur as a result of a transition-metal-nitrogen multiple bond stabilized by the π-donor interactions from the nitrogen lone pairs and vacant metal d orbitals. Late first-row transition metals such as nickel are often considered too electron-dense to accept electron density and are more often used for reductive chemistry. Late transition metal nitrenoid complexes are advantageous to catalyze new C–N and N–H bond-forming reactions over their early transition metal alternatives due to the less polarized nature of the metal-ligand multiple bond and more electrophilic nitrene unit.[2] It is therefore of interest to design systems with late first-row transition metals with empty d orbitals with the correct symmetry and energy to accept electron density from the nitrogen p orbitals through π bonding.

Several strategies have been employed to set the foundation for controlled N–group transfer reactivity with late transition metals. One such approach is to invoke low coordinate geometries that deliberately position empty d orbitals with the correct symmetry for π bonding.[2,6,11] Another strategy that has been considered recently is to incorporate weak field ligands to invoke intersystem crossing to a high or intermediate spin state.[5,12–15] Despite these two strategies, it is generally assumed that complexes with square planar geometries (most commonly d^8 metals) are not able to accommodate metal-ligand multiple bonds due to their filled d_{xz} and d_{yz} orbitals.[16] One exemption to this is the square planar $Os^{IV}(NAr)_2(PMe_2Ph)_2$ complex, which has a total of 20 valence electrons (including nitrogen lone pairs), 2 of which remain nonbonding in the NAr ligand's π system.[17] A lesser-explored approach is to incorporate redox-active ligands into a

system with a late transition metal such as nickel to stabilize the metal-ligand multiple bond and facilitate nitrene transfer reactivity.[1,18]

It is well established that redox-active ligands can be introduced to a transition metal complex and facilitate otherwise inaccessible reactivity. Several proof-of-concept reactions demonstrated the ability of redox-active ligands to serve as electrons donors with d^0 metals. An example is the zirconium complex with a tris(amido) catecholate ligand that was able to facilitate catalytic nitrene transfer with electrons sourced from the ligand.[19,20] The incorporation of redox-active ligands into complexes with transition metals with $d > 0$ have also gained significant attention; however, elucidating the electronic configurations becomes more challenging. A less common use of complexes with redox-active ligands is to exploit the empty π system in a fully oxidized ligand as an electron acceptor[21] and, through the correct symmetry, alleviate the electron density from the metal and facilitate nitrene transfer.

This Chapter presents the reactivity studies with the monoanionic $\{[ONO^{cat}]Ni(PPh_3)\}^{1-}$ complex presented in Chapter 4 and its pyridine analogue $\{[ONO^{cat}]Ni(py)\}^{1-}$. The main focus of the work was to capture a nickel-imido or iminyl complex from the reaction of $K\{[ONO^{cat}]Ni(py)\}$ with p-tolylazide. While a well-defined nickel nitrenoid complex was not isolated, it is hypothesized that a transient nickel imido complex is plausible due to the observed two-electron nitrogen-atom transfer reaction, where a carbodiimide was generated from p-tolylazide and *tert*-butylisocyanide.

5.2 Results
5.2.1 Exchange reactions and synthesis of $K\{[ONO^{cat}]Ni(py)\}$

Chapter 4 presented a nickel complex with a fully reduced [ONO] ligand and triphenylphosphine, $K\{[ONO^{cat}]Ni(PPh_3)\}$. This complex was analyzed by cyclic voltammetry to assess its propensity to serve as an electron reservoir. The voltammetric data, referenced to the

[FeCp$_2$]$^{+/0}$ redox couple, indicated that the complex could undergo two reversible oxidations at modest potentials of –0.97 and –0.49 V in MeCN. With this assessment, it was hypothesized that the K{[ONO^{cat}]Ni(PPh$_3$)} complex would be suitable to react with azides to yield a nickel-imido with the two electrons provided from the [ONO] backbone while
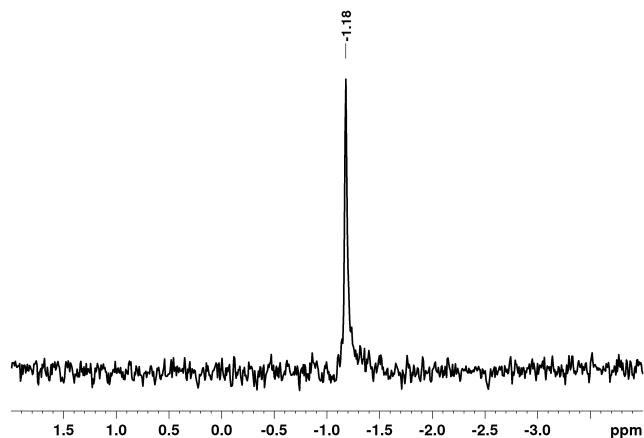
Figure 5.1. ^{31}P{^{1}H} NMR spectrum of Ph$_3$P=N–tolyl.

maintaining the +2 oxidation state of the nickel center. Initial reactivity studies were performed by treating K{[ONO^{cat}]Ni(PPh$_3$)} with *p*-tolylazide in the presence of excess pyridine. ^{1}H and ^{31}P{^{1}H} NMR analysis of this reaction demonstrated the conversion of the azide to phosphinimide by the growth of a characteristic Ph$_3$P=N-tolyl signal at –1.18 ppm, shown in **Figure 5.1**.[3] During this reaction, the loss of the auxiliary ligand PPh$_3$ would leave an open coordination site at the nickel center for the pyridine to coordinate. As predicted, a new red K{[ONO^{cat}]Ni(py)} complex was identified by ^{1}H NMR spectroscopy as a result of the loss of PPh$_3$ from the initial complex. The formation of this new pyridine analogue, K{[ONO^{cat}]Ni(py)}, probed the examination into access to this new species through various other routes. From here, the green K{[ONO^{cat}]Ni(PPh$_3$)} complex was subject to ligand exchange studies with pyridine, and the solution changed to red without the presence of azide. This color change suggested that the PPh$_3$ ligand could be displaced simply by pyridine without the need for the formation of phosphinimide. This reaction, shown in **Scheme 5.1**, was not reversible with up to 100 equivalents of PPh$_3$.

Scheme 5.1. Ligand displacement reaction of K{[ONO^{cat}]Ni(PPh$_3$)} with pyridine
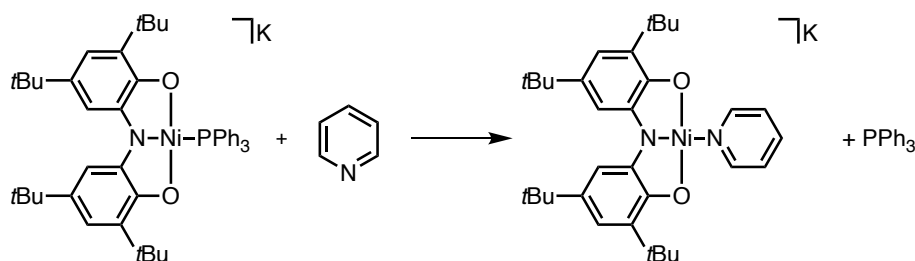
To identify the nickel coordination environment in this new species, single-crystal X-ray diffraction studies were performed. The red K{[ONO^{cat}]Ni(py)} complex was isolated and single crystals, suitable for X-ray diffraction studies, were obtained in a concentrated Et$_2$O solution at –36 ˚C. Alternatively, the K{[ONO^{cat}]Ni(py)} complex can be obtained from similar synthetic routes as the phosphine derivative through ligand deprotonation with three equivalents of KH followed by salt metathesis with NiCl$_2$(py)$_2$. Unique single crystals were obtained from this reaction from concentrated solutions of K{[ONO^{cat}]Ni(py)} in MeCN in the presence of potassium chelating agent 2.2.2. cryptand. The structure of the anion {[ONO^{cat}]Ni(py)}$^{1-}$, with potassium ion and solvent molecules removed for clarity, is shown in **Figure 5.2** with pertinent bond distances reported in **Table 5.1**. There exist minor differences between the cryptand bound structure and the structure obtained without chelating agent. The increase in the O–C bond distances in the unbound structure results from the close proximity of the potassium ion to the oxygen atom. The slight deviations in τ_4 values can also be
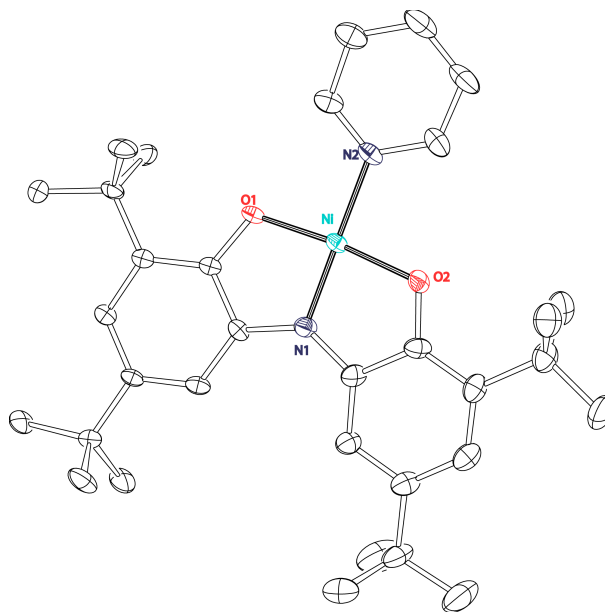
Figure 5.2. Solid-state structure of K{[ONO^{cat}]Ni(py)} with thermal ellipsoids set at 50 % probability. Hydrogen atoms, potassium counter ion, and solvent molecules (Et$_2$O and pyridine) are omitted for clarity.

122

attributed to the lack of encapsulation of the potassium. In the unbound structure, the potassium is positioned in between two $\{[ONO]Ni(py)\}^{1-}$ units with electrostatic interactions with the nickel and oxygens as well as to an ether solvent molecule. The second potassium is positioned in close proximity to an aromatic ring of the [ONO] backbone and a free pyridine molecule. The coordination environment about the nickel center in both structures is square planar with τ_4[22] values between 0.06 and 0.08. Metal–heteroatom bond distances are typical for a nickel (II) metal center with Ni–O and Ni–N bonds.[23–26] Intra-ligand bond distances O–C, N–C, and C–C, are all consistent with a fully reduced [ONO] ligand.[27–30] The oxidation state of the fully reduced ligand is confirmed from the calculated MOS[31] value of –2.7.

Table 5.1. Selected bond distances (Å) from solid-state structures of K{[ONO^{cat}]Ni(py)} and K(2.2.2.-crypt){[ONO^{cat}]Ni(py)}.

	K{[ONO^{cat}]Ni(py)}	K(2.2.2.-crypt){[ONO^{cat}]Ni(py)}
	Bond Lengths (Å)	
Ni–O(1)	1.84226(12)	1.84060(10)
Ni–O(2)	1.84852(14)	1.84314(10)
Ni–N(1)	1.81861(13)	1.81987(7)
Ni–N(2)	1.92404(14)	1.92076(8)
Ni–O(3)	--	--
O(1)–C(1)	1.37007(12)	1.35029(5)
O(2)–C(8)	1.35246(8)	1.34493(5)
N(1)–C(6)	1.38969(9)	1.39521(7)
N(1)–C(7)	1.38150(12)	1.38585(6)
τ_4	0.075	0.056
Calc. MOS	-2.73	-2.75

5.2.2 Electrochemistry of K{[ONO^{cat}]Ni(py)}

With the well-behaved electrochemistry of the K{[ONO^{cat}]Ni(PPh$_3$)} complex described in Chapter 4, it was of interest to investigate the redox properties of the analogous K{[ONO^{cat}]Ni(py)} complex. Data were collected on acetonitrile solutions containing 1 mM analyte and 0.1 M [Bu$_4$N][PF$_6$] as the supporting electrolyte using a standard three-electrode configuration with a glassy carbon working electrode, a platinum wire counter electrode, and a silver wire pseudo-reference electrode. All potentials were referenced to the [Cp$_2$Fe]$^{+/0}$ redox couple using an internal standard added to the cell at the end of the data collection. **Figure 5.3** shows the cyclic voltammogram collected for K{[ONO^{cat}]Ni(py)}, showing three reversible one-electron oxidations ($i_{pa}/i_{pc} \cong 1$ and E$_a$-E$_c$ = 80 mV) at –0.92 V, –0.43 V, and 0.64 V. After consulting the previously characterization {[ONO^{cat}]Ni(PPh$_3$)}$^{1-}$ complex described in Chapter 4, the first two oxidations are assigned as ligand-centered processes, [ONO]$^{2-/3-}$ and [ONO]$^{1-/2-}$; whereas the third at 0.64 V is assigned as a nickel-centered process, Ni$^{III/II}$.
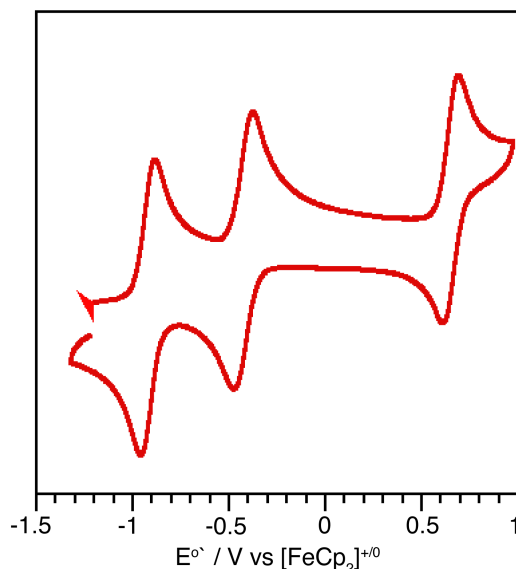
Figure 5.3. Cyclic voltammetry recorded with 1 mM analyte concentration K{[ONO^{cat}]Ni(py)} with 0.1 M [NBu$_4$][PF$_6$] electrolyte in dry, degassed MeCN under a nitrogen atmosphere using a 3 mm glass carbon working electrode, Pt wire counter electrode and Ag$^{+/0}$ pseudo-reference electrode at room temperature with 200 mV sec^{-1} scan rates. Open circuit potential is indicated by an arrowhead.

5.2.3 Attempted isolation of nickel-imido complex with [ONO] redox-active ligand

With insights gleaned from the electrochemistry and the initial reactivity studies with K{[ONO^{cat}]Ni(PPh$_3$)} and K{[ONO^{cat}]Ni(py)}, it was of interest to explore the potency of the latter complex toward nitrene transfer. Since it has been shown that the reaction of K{[ONO^{cat}]Ni(PPh$_3$)} with *p*-tolylazide results in the expulsion of phosphinimide, for stoichiometric simplicity, K{[ONO^{cat}]Ni(py)} was used for all further reactivity. The reaction of *p*-tolylazide with K{[ONO^{cat}]Ni(py)} resulted in a deep blue solution with broad signals in the ^{1}H NMR spectrum. Due to the inability to identify the product of this reaction by ^{1}H NMR spectroscopy, a Job plot analysis was performed to determine the mole fraction of the nickel complex relative to the azide. From the results of the Job plot analysis shown in **Figure 5.4**, the reaction of K{[ONO^{cat}]Ni(py)} with *p*-tolylazide requires two equivalents of nickel complex. Monitoring this reaction by UV-vis spectroscopy revealed the appearance of a transition around 580 nm, reminiscent of the singly oxidized [ONO•] metal complex in Chapter 4. Such complexes have characteristic π-π* transitions ~600 nm, while fully oxidized complexes exhibit more complex spectra with features appearing at lower energies < 700 nm.[29] From this observation, it was hypothesized that the product of this reaction includes a singly oxidized [ONO•] ligand.
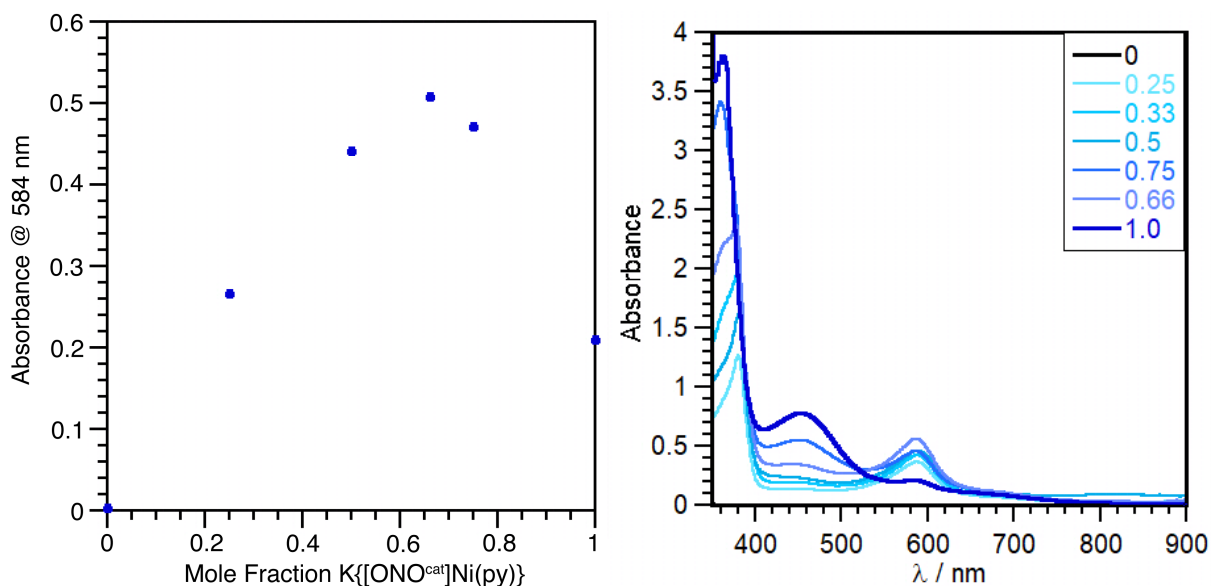
Figure 5.4. Job plot of K{[ONO^{cat}]Ni(py)} and *p*-tolylazide in benzene at room temperature. Absorbance plot with varying concentrations of K{[ONO^{cat}]Ni(py)} and *p*-tolylazide in benzene at room temperature.

The broad NMR spectrum of the reaction of *p*-tolylazide with K{[ONO^{cat}]Ni(py)} prompted the investigation into the paramagnetic nature of this putative product by X-band electron paramagnetic resonance (EPR) spectroscopy. The EPR spectrum, shown in **Figure 5.5**, of the blue reaction mixture was obtained in toluene at 77 K and was simulated with two species of equal weighting. The first species features a rhombic signal with g values at 2.03, 2.01, and 1.98 and ^{14}N hyperfine interactions with A(^{14}N) = 55, 11, and 51 MHz, consistent with a ligand-based radical. The second species is best described as a rhombic signal with g values at 2.26, 2.20, and 2.08 and ^{14}N hyperfine interactions at A (^{14}N) = 0, 156, and 211 MHz. This system is reminiscent of the nickel-based radical, similar to those observed in Chapter 4.

g_{21} = 2.26
A (^{14}N) = 0
g_{22} = 2.20
A (^{14}N) = 156
g_{23} = 2.08
A (^{14}N) = 211

g_{11} = 2.03
A (^{14}N) = 55
g_{12} = 2.01
A (^{14}N) = 11
g_{13} = 1.98
A (^{14}N) = 51
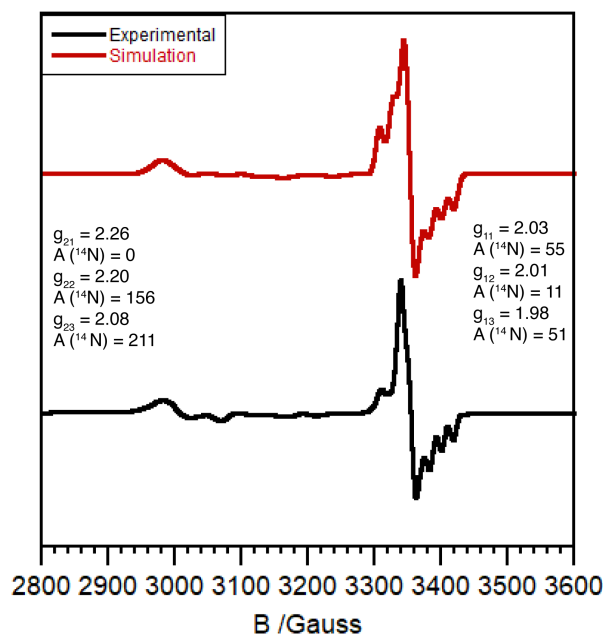
Figure 5.5. X-band EPR spectrum of the reaction mixture of *p*-tolylazide and K{[ONO^{cat}]Ni(py)} in toluene at 77 K with experimental spectrum shown in black and simulation in red.

5.2.4 Catalytic activity with *p*-tolylazide and CN^{t}Bu

The isolation of the product from the reaction of K{[ONO^{cat}]Ni(py)} and *p*-tolylazide remained challenging; therefore, to make inferences about a transient nickel-imido complex, reactivity studies with CN^{t}Bu were conducted. The dropwise addition of a K{[ONO^{cat}]Ni(py)} (10 mol %) solution to a benzene solution of *p*-tolylazide and CN^{t}Bu at room temperature resulted in the slow conversion to the carbodiimide shown in **Scheme 5.2**. The product of this reaction was monitored by GC-MS, and over the course of 11 days, a decrease of *p*-tolylazide and an increase in carbodiimide product was observed. However, the 10% catalyst loading was limiting and only resulted in a 10% conversion of product, which suggested that this reaction was not catalytic. Another option is that a side-product or decomposition pathway was dominating the reaction, preventing catalytic turnover. Appendix A describes the investigation into potential side-products formed during this reaction and shows that trace tetrahydrofuran (THF) and water result in the formation of *p*-toluidine and K{[ONO•]Ni(OH)}.

127

Scheme 5.2. Catalytic reaction of *p*-tolylazide and CN^tBu with 10 mol % K{[ONO^cat]Ni(py)}.
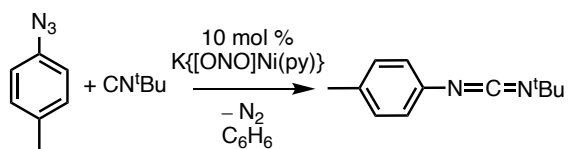
The lack of catalytic turnover was thought to be caused by either presence of residual solvent or by the formation of a stable K{[ONO^cat]Ni(CN^tBu)$_x$} complex. Lyophilization with benzene and excessive drying of K{[ONO^cat]Ni(py)} removed all traces of THF, and this material was then subject to the same reaction conditions. To assess the presence of THF and with the clear spectroscopic handles present in the methyl region, ^{1}H NMR spectroscopy was used to determined percent conversion with an internal standard of 10% hexamethylbenzene. With 10% catalytic loading of K{[ONO^cat]Ni(py)}, the reaction of *p*-tolylazide with CN^tBu resulted in the formation of carbodiimide in a 27 % yield over the course of 20 hours. This reaction was also conducted at 60 ˚C, where a yield of 70 % was observed after 20 hours. No further reactivity was observed for this reaction after 20 hours. Various other arylazides were used to determine a substrate scope with a range of Hammett constants. **Table 5.2** reports the percent carbodiimide formation with 10 % catalyst loading at 60 ˚C after 20 hours with *p*-tolylazide, phenylazide, 4-MeO-phenylazide, and 4-CF$_3$-phenylazide. The *para*-substituted azides produced greater amounts of carbodiimide compared to the phenylazide (43 ± 4 %) increasing from *p*-tolylazide (69 ± 2 %) < 4-MeO-phenylazide (83 ± 1 %) < 4-CF$_3$-phenylazide (84 ± 9 %). All reactions were performed in duplicate, and control reactions of isocyanide and aryl azide with no catalyst showed no carbodiimide formation after 20 hours at 60 ˚C.

Table 5.2. Carbodiimde Formation from organoazides and isocyanides catalyzed by K{[ONO^{cat}]Ni(py)}.

Azide	% carbodiimide 60 °C 20 h	TON
p-tolyl-N$_3$	69 ± 2	6.9
phenyl-N$_3$	43 ± 4	4.3
4-MeO-phenyl-N$_3$	83 ± 1	8.3
4-CF$_3$-phenyl-N$_3$[a]	84 ± 9	8.4

[a] complete after 5 hours

Several other azides, both alkyl and aromatic were used instead of *p*-tolylazide to assess the steric and electronic properties required to optimize or stabilize a nickel-imido intermediate. No reaction was observed with bulky aromatic azides such as mesitylazide and *m*-terphenylazide or alkyl azide,
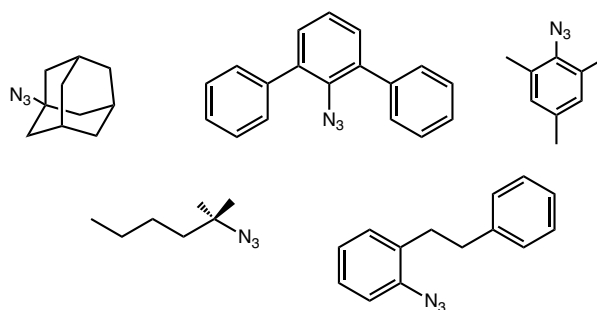
Figure 5.6. Various azides used in unsuccessful reactivity with K{[ONO^{cat}]Ni(py)}

adamantylazide, shown in **Figure 5.6**. C–H amination has recently been observed with late-transition metal imido/iminyl complexes as a result of intramolecular H-atom abstraction. The strategic placement of linear alkyl moieties would provide the reactive equivalents for a nickel-imnyl to abstract an H-atom affording a nickel anilido species. Unfortunately, using 2-azido-2-methylhexane and 1-azido-2-phenethylbenzene with K{{ONO^{cat}}Ni(L)} (L = PPh$_3$, py) in benzene did not result in any new N-heterocycles.

To help give insight into a potential catalyst poison, the order of addition of this reaction was varied to where the CN^{t}Bu was added to the catalyst first and allowed to react for 7 hours.

This allowed for the formation of K{{ONO^{cat}]Ni(CN^{t}Bu)$_x$} (x= 1 or 2), which was identified by the peak at 1.10 ppm in the ^{1}H NMR spectrum. Post isocyanide addition, three equivalents of *p*-tolylazide were added and monitored by ^{1}H NMR after 20 hours. At room temperature, only 6% carbodiimide was recorded; however, when the reaction was heated to 60 ˚C, the reaction yield increased to 72 %. H-atom donor 9,10-dihyroanthracene (9,10-DHA) (BDE 76 kcal mol^{-1})[32] was added to the initial reaction to provide a source of H-atom in attempts to locate a diverted pathway. After 20 hours at room temperature with 9,10-DHA, the reaction yield showed no depreciable change from the reaction without DHA.

5.2.5 Synthesis of potential catalytic poisons

With the low conversion of nitrene transfer products at room temperature discussed in Section 5.2.4, it would be informative to isolate potential intermediates that would potentially poison the catalytic reaction or result in an off-cycle pathway. **Scheme 5.3** shows the familiar synthetic approach, deprotonation followed by salt metathesis, employed in attempts to synthesize a nickel isocyanide complex, K{[ONO^{cat}]Ni(CN^{t}Bu)}. The reaction proceeded as expected with the evolution of H$_2$ gas upon ligand deprotonation with KH followed by a color change to green upon the addition of metal synthon NiCl$_2$(CN^{t}Bu)$_2$. ^{1}H NMR analysis in acetonitrile-d_3 revealed the expected two aromatic signals integrating to 4 protons for the [ONO] backbone, the 2 singlets from the 18 protons of the *tert*-butyl groups on the [ONO] backbone and two unique singlets at 1.54 and 1.41 ppm, integrating to 9 protons each, suggesting two bound CN^{t}Bu ligands. As with many of the K{[ONO^{cat}]Ni(L)} anions, the NMR spectrum in benzene-d_6 lost definition in the aromatic region but maintained distinctive singlets in the alkyl region at 1.36, 1.10, 0.87, and 0.85 ppm for the *tert*-butyl groups, two from two bound CN^{t}Bu ligands and two from the [ONO] ligand. Without crystallographic evidence, solution-state NMR analysis is the primary identifier of

coordination geometry, which until a single crystal can be obtained, the putative complex is described as a five-coordinate K{[ONO^{cat}]Ni(CN^{t}Bu)$_2$} complex.

Scheme 5.3. Synthesis of K{[ONO^{cat}]Ni(CN^{t}Bu)$_2$}.
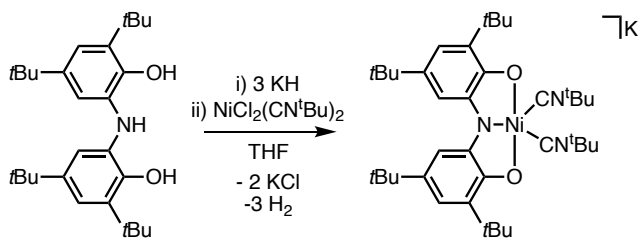
5.2. Analogous Reactivity with K{[SNS^{cat}]Ni(PPh$_3$)}

The limiting factor for the analogous [SNS] system to do nitrene transfer reactivity is its access to only one electron in the ligand backbone. Since the above sections suggest a putative nickel imido and spectroscopic data indicate the involvement of a singly oxidized [ONO•] ligand, similar reactivity studies were carried out on the K{[SNS^{cat}]Ni(PPh$_3$)} complex discussed in Chapter 2. **Scheme 5.4** shows attempts to isolate the pyridine complex, K{[SNS^{cat}]Ni(py)}, through both synthetic routes, ligand exchange, and salt metathesis. ^{1}H NMR analysis of both reactions resulted in identical spectroscopic signatures suggesting the product of both reactions was a K$_2${[SNS]$_2$Ni$_2$•THF} dimer instead of the desired K{[SNS^{cat}]Ni(py) complex. Despite the inability to access the pyridine system, reactivity with azides was attempted to no avail, with no changes in the ^{1}H NMR spectra. No further reactivity was attempted thereafter.

Scheme 5.4. Attempted synthesis of K{[SNS^{cat}]Ni(py)}.
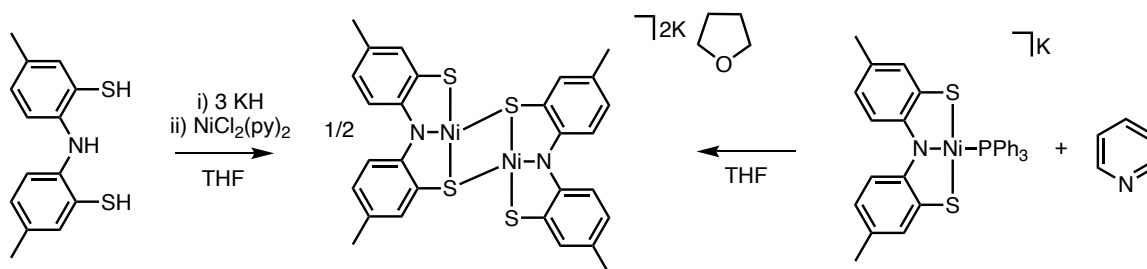
5.3 Discussion

The reactivity of the fully reduced K{[ONO^{cat}]Ni(PPh$_3$)} complex was examined for ligand displacement and oxidative group transfer. There are many factors that should be considered when discussing transition metal complex stability and their ability to undergo ligand displacement. It is often most helpful to consider the size and energetic matching of ligand and metal. The parent {[ONO^{cat}]Ni(PPh$_3$)}$^{1-}$ complex has 16 valence electrons, a stable electron count for a d^8 square planar complex, with strong σ donor PPh$_3$ ligand, and therefore upon initial inspection, would not be expected to undergo ligand displacement with pyridine. However, when in the presence of pyridine, the PPh$_3$ dissociates, affording the new K{[ONO^{cat}]Ni(py)} complex. Hard-soft acid-base theory (HSAB)[33] suggests that pyridine is considered a better match for the nickel (II) metal ion as hard nitrogen donors are more well suited for the hard/intermediate nickel (II) ion compared to the larger, softer PPh$_3$. When considering the bond enthalpies (ΔH) for the Ni–PPh$_3$ and Ni–py interactions using Drago's E–C equation[34], the displacement of PPh$_3$ by pyridine is not surprising.

$$-\Delta H = E_A E_B + C_A C_B \tag{5.1}$$

Using reported C_a and E_a values for a nickel cation[35] and C_b and E_b for pyridine[34] and PPh$_3$[36], the calculated ΔΔH$_{formation}$ for the K{[ONO^{cat}]Ni(py)} complex is expected to be –16 kcal mol^{-1}, suggesting a significant preference of the pyridine ligand over PPh$_3$.

For stoichiometric simplicity and the absence of by-products such as phosphinimides in solution, $K\{[ONO^{cat}]Ni(py)\}$ was used to probe this platform's ability to undergo oxidative nitrene transfer through the reducing equivalents stored in the redox-active ligand backbone. The reaction of $K\{[ONO^{cat}]Ni(py)\}$ with p-tolylazide was predicted to undergo a two-electron oxidation and afford a nickel imido with a fully oxidized [ONO] ligand, $\{[ONO^q]Ni(N\text{-}tolyl)\}^{1-}$. Since the parent $K\{[ONO^{cat}]Ni(py)\}$ complex is diamagnetic and the presumed imido complex would be the result of two-electron oxidation, it was predicted that this complex would also be diamagnetic. This was not the case, as the resulting deep blue product was paramagnetic, and displayed two sets of rhombic signals ($g_{11} = 2.03$, $g_{12} = 2.01$, $g_{13} = 1.98$; $g_{21} = 2.26$, $g_{22} = 2.20$, $g_{23} = 2.08$) with ^{14}N hyperfine interactions. The first species is reminiscent of an [ONO•] semiquinonate complex with similar spectroscopic features to [ONO•]Ni(NEt$_3$) (reported in Appendix A). The second species displays similar g values as the Ni centered radical discussed in Chapter 4, as well as other Ni^I complexes.[37–39] Previously reported nickel-imides displayed similar spectroscopic features to the second species with g values around 2.20, 2.10, and 1.95 and hyperfine splitting constants of $A(^{14}N) = \sim20$ G.[40,41] The hyperfine splitting constants in the second species are much larger, 156 G and 211 G, suggesting substantial nitrogen involvement in the singly occupied molecular orbital of this species. Job plot analysis also complicated the initial hypothesis as the reaction showed to proceed in a 2:1 nickel complex to azide ratio. The combination of these two results led to the belief that a putative nickel imido ($\{[ONO^q]Ni(N\text{-}tolyl)\}^{1-}$) complex is transient and undergoes single-electron transfer from a second equivalent of $K\{[ONO^{cat}]Ni(py)\}$. The products of this reaction are still speculative and will need to be corroborated by X-ray crystallography. Attempts to obtain a single crystal of this product are still in progress. While the isolation of a nickel imido

complex remained elusive, its transient nature could be inferred by observing a nitrene transfer product such as carbodiimide.

The isolation of nickel imidos has been made possible with the use of strategic geometric and electronic manipulation,[11,42–44] and stoichiometric reactivity have been observed with isocyanides, carbon monoxide, and styrene.[2,45,46] There have been fewer examples, however, of catalytic carbodiimide formation mediated through nickel catalysts. Recently the Warren group[41] have reported a ß-diketiminato nickel imide capable of performing nitrene transfer with isocyanides in addition to the Hillhouse group[47] who used dinuclear N-heterocyclic carbenes to perform similar reactivity. From this limited precedent, the catalytic reaction of *p*-tolylazide and CN^{t}Bu was examined with the K{[ONO^{cat}]Ni(py)} complex. The initial results reported a low conversion of ~10 %, which suggested decomposition or competing reactions hindered catalysis.

The potential decomposition pathway involving solvent interference[45,48] could be overcome by removing trace THF from the parent complex. After excessive drying, the parent {[ONO^{cat}]Ni(py)}$^{1-}$ complex was subject in catalytic amounts to *p*-tolylazide and CN^{t}Bu. ^{1}H NMR analysis showed a 27 % conversion after 20 hours at room temperature with a significant increase to 70 % at 60 ˚C. Similar conversions with other *para*-substituted phenylazides were observed at 60 ˚C. There was a substantial decrease in carbodiimide conversion with the unsubstituted phenylazide and no conversion with bulky aromatic and alkyl azides. Previous reports of a copper nitrene complex bearing an aromatic triplet nitrene undergoes C–C radical coupling at the *para* position on the aryl moiety, and *para*-substituted aryl azides were used in this case to prevent such reactivity. Further investigations into a similar type of mechanism will be investigated for the system reported herein.[10]

When varying the order of addition of reactants to the catalyst, some mechanistic insights could be obtained. The addition of CN^{t}Bu to the K{[ONO^{cat}]Ni(py)} complex resulted in a color change from red to black and the appearance of a singlet peak in the ^{1}H NMR spectrum at 1.10 ppm, similar to that obtained from the spectrum of {[ONO^{cat}]Ni(CN^{t}Bu)$_2$}$^{1-}$. Adding 3 equivalents of *p*-tolylazide to this mixture resulted in ~5% conversion after 20 hours. From here, it is thought that {[ONO^{cat}]Ni(CN^{t}Bu)$_2$}$^{1-}$ does react with the *p*-tolylazide just at a sluggish rate. Therefore, it is thought that if any {[ONO^{cat}]Ni(CN^{t}Bu)$_2$}$^{1-}$ is formed in solution , catalysis is sluggish at room temperature, but this can be overcome by heating the reaction to 60 ˚C. Adding H-atom donor 9,10-DHA to the reaction mixture did not result in a decrease in product formation, suggesting it is the formation of {[ONO^{cat}]Ni(CN^{t}Bu)$_2$}$^{1-}$ and its slow reactivity with *p*-tolylazide that limits catalytic turnover. **Scheme 5.5** shows a potential mechanism of the catalytic conversion of carbodiimide over {[ONO^{cat}]Ni(py)}$^{1-}$ through a transient nickel imido.

Scheme 5.5. Potential mechanism for the formation of carbodiimide from organoazides and isocyanides with 10 mol % K{[ONO^cat]Ni(py)}.
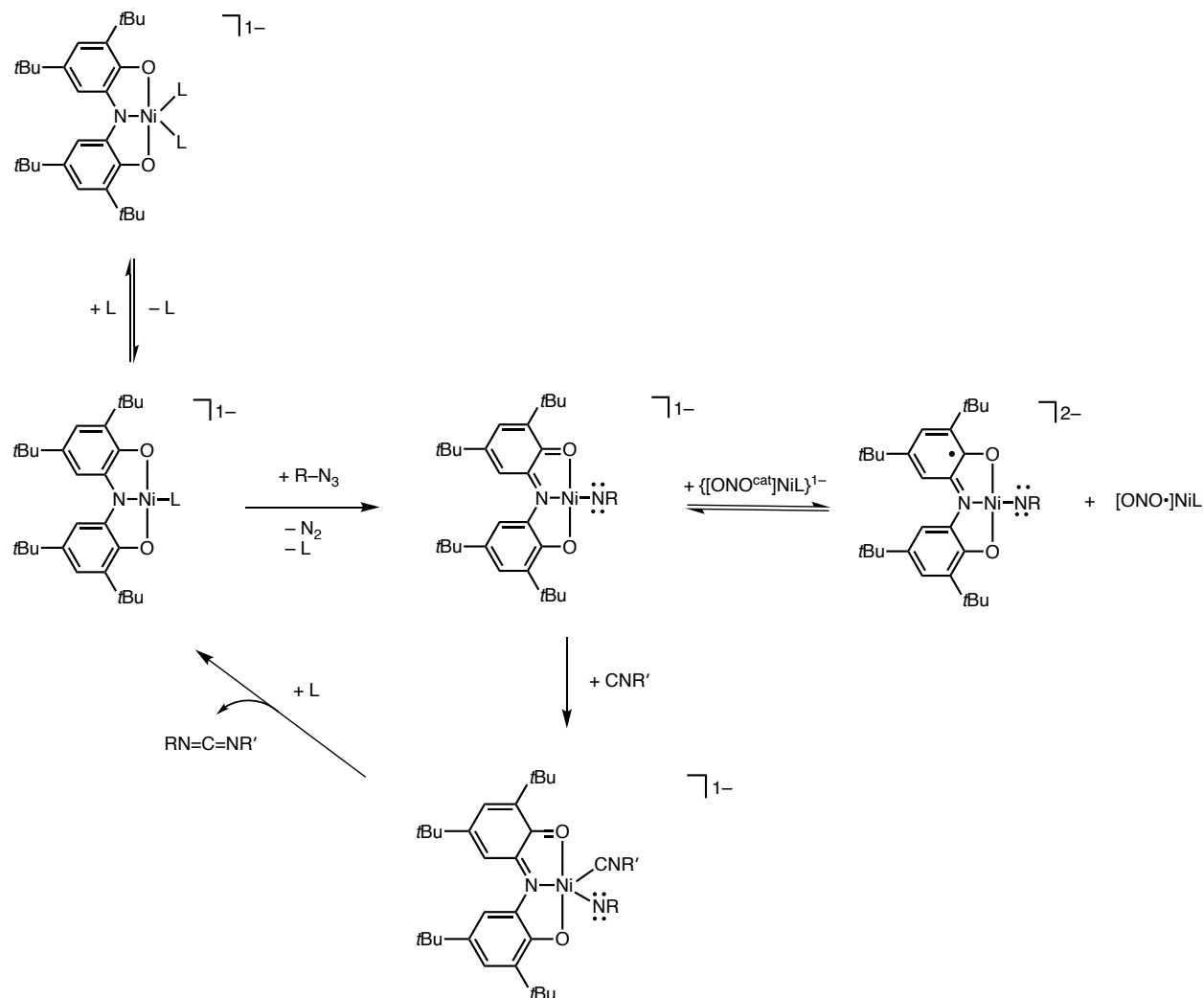
The ability of a nickel (II) square planar complex to support a metal-ligand multiple bond is unlikely due to the filled metal *d* orbitals. The evidence presented in this Chapter suggests that the {[ONO^cat]Ni(py)}^{1−} complex can facilitate nitrene transfer which would involve a transient nickel imido. In this system, the HOMO involved in reactivity is the π* of the redox-active [ONO] ligand. This orbital, while mainly ligand-based, does possess some metal character from a d_{yz} orbital. This metal orbital is of the correct symmetry to accept the π electrons from the "imido," and while the metal-based orbital is filled, as the ligand becomes oxidized, it is able to relieve the

electron density on the metal center. Further studies to confirm the electronic assignment of reaction intermediates will be pursued by current lab members.

5.4 Conclusion

Reactivity of the previously isolated $\{[ONO^{cat}]Ni(PPh_3)\}^{1-}$ complex was investigated. Ligand displacement with nitrogen-based donors showed the nickel (II) center's preference towards hard nitrogen donors compared to PPh_3. Electrochemistry of the fully reduced $\{[ONO^{cat}]Ni(L)\}^{1-}$ complex show the complexes' ability to store two electrons in the ligand framework. Harnessing those two electrons was then probed by exploring catalytic nitrene transfer with azides and isocyanides. When in the absence of residual THF, the catalytic conversion, facilitated by $\{[ONO^{cat}]Ni(py)\}^{1-}$, with *p*-tolylazide and CN^tBu at room temperature was ~30 % which increased to 70 % at 60 ˚C. Potential catalytic poisons include THF and water in the reaction mixtures as well as the formation of a stable intermediate $\{[ONO^{cat}]Ni(CN^tBu)_2\}^{1-}$. This work presents the ability of redox-active ligands to alleviate electron density at a metal center and invoke new, otherwise forbidden, reactivity in late transition metal group transfer.

5.5 Experimental

General Considerations. The compounds and reactions reported below show various levels of air- and moisture- sensitivity; therefore, all manipulations were performed using standard Schlenk-line and glovebox techniques. Hydrocarbon and ethereal solvents were sparged with argon before being deoxygenated and dried by passage through Q5 and activated alumina columns, respectively. Halogenated solvents and triethylamine were sparged with argon and passed through two activated alumina columns. Potassium hydride was obtained in mineral oil and washed with pentane prior to use. Pyridine was dried over KOH, distilled, freeze pump-thawed, and stored over sieves. *Tert*-butylisocyanide was distilled and freeze pump-thawed thrice and stored over sieves. Terphenyl

azide,[49] 2-azido-12-methylhexane[50], 1-azido-2-phenethylbenzene,[51] $NiCl_2(py)_2$[52] $NiCl_2(CN^tBu)_2$[53] and arylazides[54] were prepared from literature procedures.

Physical Methods. NMR spectra were collected at 298 K on a Bruker Avance 400 MHz or 600 MHz spectrometer in dry, degassed C_6D_6, or CD_3CN. ^1H NMR spectra were referenced to tetramethylsilane (TMS) using residual proteo impurities of the solvent (7.16 ppm or 1.93 ppm) and $^{31}P\{^1H\}$ NMR spectra were referenced with an external standard of phosphoric acid (H_3PO_4, 85%, 0.00 ppm). All chemical shifts are reported in standard δ notation in parts per million. Perpendicular-mode X-band (9.352 GHz) EPR spectra were collected at 77 K using a Bruker EMX spectrometer equipped with ER041XG microwave bridge. The following spectrometer settings were used: attenuation = 20 dB, microwave power 1.997 mW, frequency = 9.352 GHz, modulation amplitude = 10.02 G, gain = 1.00 x 10^3, conversion time = 4.91 ms, time constant = 81.92 ms, sweep width 5500 G and resolution 1024 points. The spectra were simulated using EasySpin for MATLAB. Electrospray ionization mass-spectrometry (ESI-MS) data were collected on a Waters LCT Premier mass spectrometer using dry, degassed MeCN or THF. Electronic absorption spectra were recorded using a Jasco V-670 absorption spectrometer in dry, degassed MeCN using a 1-cm path-length cells at ambient temperature (20-24 °C).

Electrochemical Methods. Electrochemical experiments were performed on a Gamry series G300 potentiostat/galvanostat/ZRA (Gamry Instruments, Warminster, PA) using a 3.0 mm glassy carbon working electrode, a platinum wire auxiliary electrode and a silver wire pseudo reference electrode. Electrochemical experiments were performed at ambient temperature (20-24 °C) in a nitrogen filled glovebox. Sample concentrations were 1.0 mM in analyte in MeCN containing 100 mM [NBu_4][PF_6] as the supporting electrolyte. All potentials are referenced to $[Cp_2Fe]^{+/0}$ using ferrocene as an internal standard.[55] Ferrocene were purified by sublimation under reduced pressure

and tetrabutylammonium hexafluorophosphate was recrystallized thrice from ethanol and dried under vacuum.

Crystallographic Methods. X-ray diffraction data were collected at low temperature on single crystals covered in Paratone and mounted on glass fibers. Data were acquired using a Bruker SMART APEX II diffractometer equipped with a CCD detector. Measurements were carried out using Mo K_α ($\lambda = 0.71073$ Å) radiation, which was wavelength selected with a single-crystal graphite monochromator. A full sphere of data was collected for each crystal structure. The SMART program package was used to determine unit-cell parameters and to collect data. The raw frame data were processed using SAINT[56] and SADABS[57] to yield the reflection data files. Subsequent calculations were carried out using the SHELXTL[58] program suite. Structures were solved by direct methods and refined on F^2 by full-matrix least-squares techniques to convergence. Analytical scattering factors for neutral atoms were used throughout the analyses.[59] Hydrogen atoms, though visible in the difference Fourier map, were generated at calculated positions and their positions refined using the riding model. ORTEP diagrams were generated using ORTEP-3[60] for Windows.

General Reaction Procedure for Reactivity Studies: In a typical experiment, to a solution of nickel complex K[{ONO}Ni(L)] (L = PPh$_3$ or pyridine) in C$_6$D$_6$, stoichiometric amounts of a C$_6$D$_6$ solution of substrate were added. The reactions were monitored by ^{1}H NMR, GC-MS and UV-vis spectroscopy.

Synthesis of K{[ONO^{cat}]Ni(py)} In a scintillation vial in a nitrogen filled glovebox, a solution of [ONO]H$_3$ (590 mg, 1.39 mmol, 1.0 equiv.) in THF (10 mL) was deprotonated using KH (167 mg, 4.16 mmol, 3.0 equiv.) to yield an immediate white precipitate and the evolution of gas (H$_2$). Once the gas ceased, light green NiCl$_2$(py)$_2$ (399 mg, 1.39 mmol, 1.0 equiv.) dissolved THF (5 mL) then

was added to the purple solution and an immediate color change to red was observed. The reaction stirred at room temperature for 1 day, when the red solution was filtered through Celite using a medium porous fritted funnel and washed with 10 mL THF. The filtrate volatiles were concentrated to 5 mL and precipitated with 30 mL of pentane. The red solid was lyophilized with benzene and dried for 2 days on vacuum line. The dark green solid was isolated in a 92 % (768 g) yield. Suitable crystals for diffraction were obtained from a concentrated solution of analyte with 2.2.2.-cryptand in MeCN at –36 °C. ^{1}H NMR (CD$_3$CN, 400 MHz) δ/ppm: 8.70 (br, 2H, aryl-H), 7.76 (br, 1H, aryl-H), 7.29 (br, 2H, aryl-H), 7.08 (br, 2H, aryl-H), 6.21 (br, 2H, aryl-H), 1.35 (s, 18H, -C(CH_3)$_3$, 1.29 (s, 18H, -C(CH$_3$)$_3$). λ$_{max}$ / nm (ε/ M^{-1}cm^{-1}): 346 (6000), 454 (1100). MS (ESI$^-$) (C$_6$H$_6$) m/z: 560.3 (MH$^+$).
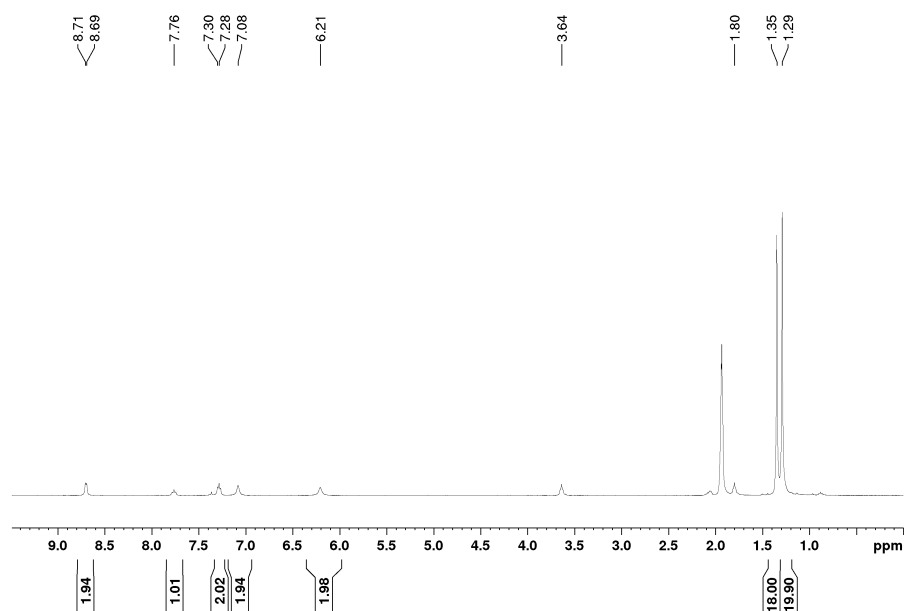
Figure 5.7. ^{1}H NMR spectrum of K{[ONO^{cat}]Ni(py)} in d$_3$-ACN at room temperature.

Synthesis of K{[ONO^{cat}]Ni(CN^{t}Bu)$_2$} In a scintillation vial in a nitrogen filled glovebox, a solution of [ONO]H$_3$ (104 mg, 244 μmol, 1.0 equiv.) in THF (10 mL) was deprotonated using KH (39 mg, 733 μmol, 3.0 equiv.) to yield an immediate white precipitate and the evolution of gas

(H$_2$). Concurrently, dark green NiCl$_2$(CN^{t}Bu)$_2$ (72 mg, 244 μmol, 1.0 equiv.) was dissolved THF

(5 mL) then frozen. Once the gas evolution ceased, the two solutions were combined and an

immediate color change to brown was observed. The reaction stirred at room temperature for 4

hours, when the brown solution was filtered through Celite using a medium porous fritted funnel

and washed with 10 mL THF. The filtrate volatiles were concentrated to 5 mL and precipitated

with 30 mL of pentane to afford a brown solid. ^{1}H NMR (CD$_3$CN, 400 MHz) δ/ppm : 7.18 (s, 2H,

aryl-H), 6.26 (s, 2H, aryl-H), 1.54 (s, 9H, -C(CH_3), 1.41 (s, 9H, -C(CH_3), 1.29 (s, 18H, -C(CH_3),

127 (s, 21H, -C(CH_3). λ$_{max}$ / nm (ε/ M^{-1}cm^{-1}): 362 (17300), 605 (1100), 829 (1300). MS (ESI$^-$)

(C$_6$H$_6$) m/z: 564.3 ({[ONO]Ni(CN^{t}Bu)}$^-$).
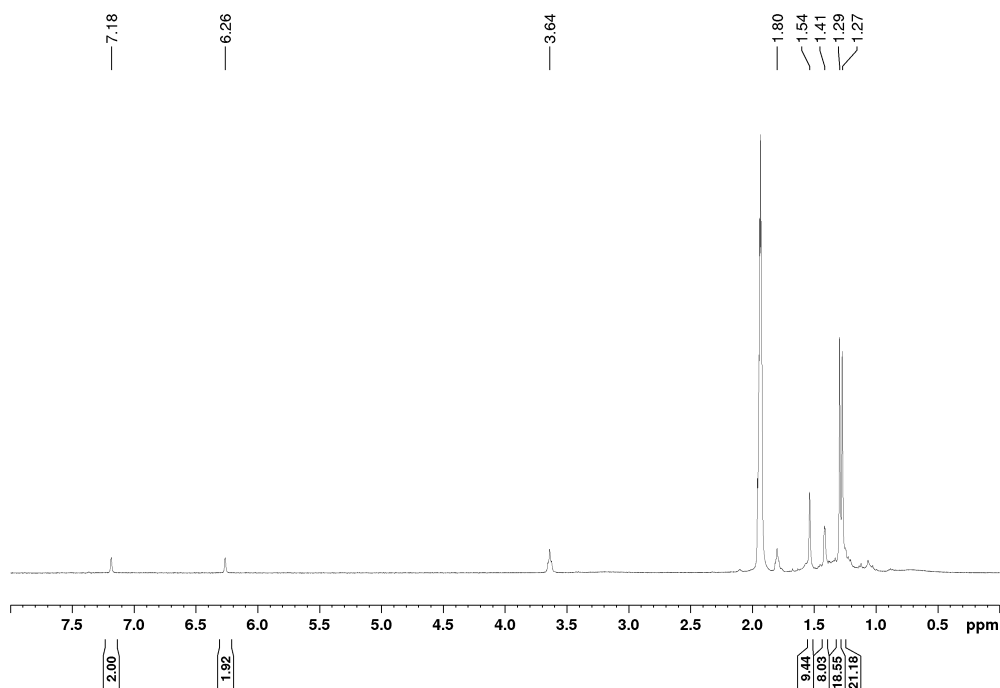

Figure 5.8. ^{1}H NMR spectrum of K{[ONO^{cat}]Ni(CN^{t}Bu)$_2$} in d$_3$-ACN at room temperature.

Attempted Synthesis of K{[SNS^{cat}]Ni(py)} In a scintillation vial in a nitrogen glovebox

atmosphere, a solution of [SNS]H$_3$ (100 mg, 383 μmol, 1.0 equiv.) in THF (5 mL) was

deprotonated using KH (46 mg, 1.15 mmol, 3.0 equiv.) to yield an immediate white precipitate and the evolution of gas (H_2). Once the gas ceased, green $NiCl_2(py)_2$ (110 mg, 383 µmol, 1.0 equiv.) was dissolved THF (5 mL) and added to the yellow solution. The reaction stirred at room temperature for 1 hour, when the green solution was filtered through Celite using a medium porous fritted funnel and washed with 10 mL THF. The filtrate volatiles were concentrated to 2 mL and precipitated with 30 mL of pentane. The purple solid was isolated in a 30 % (81 mg) yield. ^{1}H NMR (CD_3CN, 400 MHz) δ/ppm : 7.24 (d, J = 8 MHz, 2H, aryl-H), 7.05 (d, J = 8 MHz, 2H, aryl-H), 6.84 (dd, J = 8 MHz, 4H, aryl-H), 6.58 (d, J = 12 MHz, 2H, aryl-H), 6.35 (d, J = 12 MHz, 2H, aryl-H), 3.64 (q, 4H, THF), 2.15 (s, 6H, -CH$_3$), 2.12 (s, 6H, -CH$_3$), 1.80 (4H, THF). MS (ESI$^+$) (THF) m/z: 703.8 (M+THF).
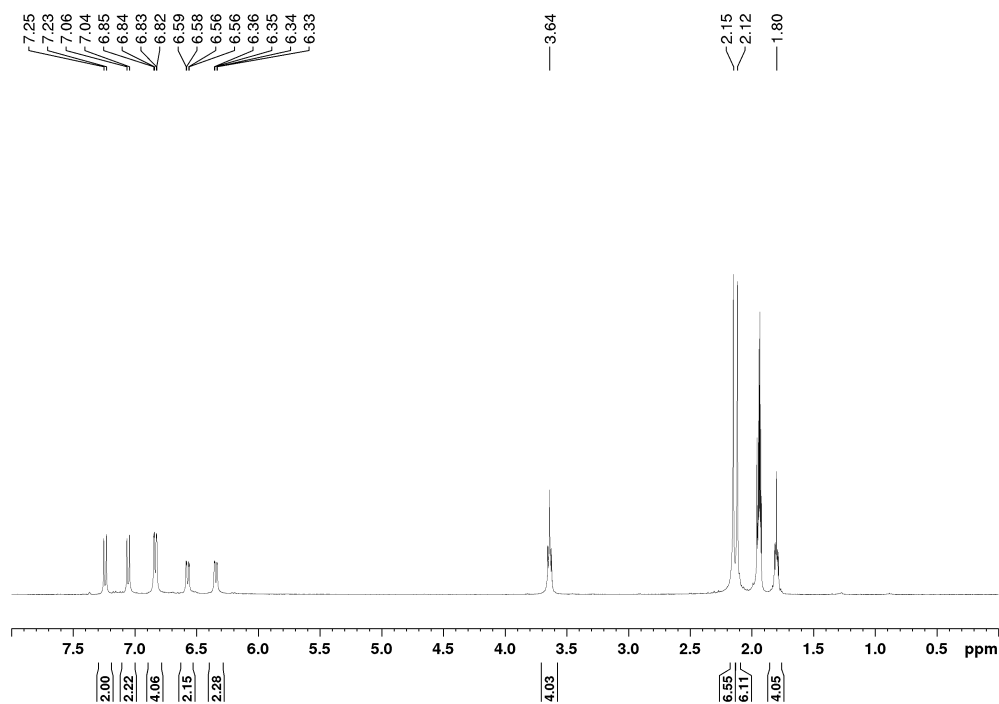

Figure 5.9. ^{1}H NMR spectrum of K$_2$\{[SNS]$_2$Ni$_2$•THF\} recorded in d$_3$-ACN at room temperature.

142

5. 6 References

1   N. P. Van Leest, M. A. Tepaske, J.-P. H. Oudsen, B. Venderbosch, N. R. Rietdijk, M. A. Siegler, M. Tromp, J. Ivar Van Der Vlugt and B. De Bruin, *J. Am. Chem. Soc*, 2020, **142**, 52.

2   E. Kogut, H. L. Wiencko, L. Zhang, D. E. Cordeau and T. H. Warren, *J. Am. Chem. Soc.*, 2005, **127**, 11248–11249.

3   C. E. MacBeth, J. C. Thomas, T. A. Betley and J. C. Peters, *Inorg. Chem.*, 2004, **43**, 4645–4662.

4   D. M. Jenkins, T. A. Betley and J. C. Peters, *J. Am. Chem. Soc.*, 2002, **124**, 11238–11239.

5   E. R. King, G. T. Sazama and T. A. Betley, *J. Am. Chem. Soc*, 2012, **134**, 17858–17861.

6   J. Du, L. Wang, M. Xie and L. Deng, *Angew. Chemie - Int. Ed.*, 2015, **54**, 12640–12644.

7   L. Nurdin, D. M. Spasyuk, W. E. Piers and L. Maron, *Inorg. Chem.*, 2017, **56**, 4157–4168.

8   E. A. LaPierre, M. L. Clapson, W. E. Piers, L. Maron, D. M. Spasyuk and C. Gendy, *Inorg. Chem.*, 2018, **57**, 495–506.

9   V. Bagchi, P. Paraskevopoulou, P. Das, L. Chi, Q. Wang, A. Choudhury, J. S. Mathieson, L. Cronin, D. B. Pardue, T. R. Cundari, G. Mitrikas, Y. Sanakis and P. Stavropoulos, *J. Am. Chem. Soc.*, 2014, **136**, 11362–11381.

10 K. M. Carsch, I. M. DiMucci, D. A. Iovan, A. Li, S. L. Zheng, C. J. Titus, S. J. Lee, K. D. Irwin, D. Nordlund, K. M. Lancaster and T. A. Betley, *Science*, 2019, **365**, 1138–1143.

11 D. J. Mindiola and G. L. Hillhouse, *J. Am. Chem. Soc.*, 2001, **123**, 4623–4624.

12 D. T. Shay, G. P. A. Yap, L. N. Zakharov, A. L. Rheingold and K. H. Theopold, *Angew. Chemie - Int. Ed.*, 2005, **44**, 1508–1510.

13 D. T. Shay, G. P. A. Yap, L. N. Zakharov, A. L. Rheingold and K. H. Theopold, *Angew. Chemie Int. Ed.*, 2006, **45**, 7870–7870.

14 Y. Baek, E. T. Hennessy and T. A. Betley, *J. Am. Chem. Soc*, 2019, **141**, 16944–16953.

15 Y. Baek and T. A. Betley, *J. Am. Chem. Soc.*, 2019, **141**, 7797–7806.

16 Z. Lin and M. B. Hall, *Coord. Chem. Rev.*, 1993, **123**, 149–167.

17 M. H. Schofield, T. P. Kee, J. T. Anhaus, R. R. Schrock, K. H. Johnson and W. M. Davis, *Inorg. Chem.*, 1991, **30**, 3595–3604.

18 D. L. J. Broere, B. de Bruin, J. N. H. Reek, M. Lutz, S. Dechert and J. I. van der Vlugt, *J. Am. Chem. Soc.*, 2014, **136**, 11574–11577.

19 A. I. Nguyen, R. A. Zarkesh, D. C. Lacy, M. K. Thorson and A. F. Heyduk, *Chem. Sci.*, 2011, **2**, 166–189.

20 A. F. Heyduk, R. A. Zarkesh and A. I. Nguyen, *Inorg. Chem.*, 2011, **50**, 9849–9863.

21 M. R. Haneline and A. F. Heyduk, *J. Am. Chem. Soc.*, 2006, **128**, 8410–8411.

22 L. Yang, D. R. Powell and R. P. Houser, *Dalton Trans.*, 2007, 955–964.

23 A. Kochem, G. Gellon, O. Jarjayes, C. Philouze, A. Du Moulinet D'Hardemare, M. Van Gastel and F. Thomas, *Dalton Trans.*, 2015, **44**, 12743–12756.

24 A. V. Piskunov, K. I. Pashanova, A. S. Bogomyakov, I. V. Smolyaninov and G. K. Fukin, *Polyhedron*, 2020, **186**, 114610.

25 A. J. McNeece, K. A. Jesse, J. Xie, A. S. Filatov and J. S. Anderson, *J. Am. Chem. Soc*, 2020, **07**, 33.

26 B. H. Northrop, Y.-R. Zheng, K.-W. Chi and P. J. Stang, *Acc. Chem. Res.*, 2009, **42**, 1554–1563.

27 A. M. Hollas, J. W. Ziller and A. F. Heyduk, *Polyhedron*, 2018, **143**, 111–117.

28   F. Lu, R. A. Zarkesh and A. F. Heyduk, *Eur. J. Inorg. Chem.*, 2012, 467–470.

29   S. Hananouchi, B. T. Krull, J. W. Ziller, F. Furche and A. F. Heyduk, *Dalton Trans.*, 2014, **43**, 17991.

30   J. L. Wong, R. F. Higgins, I. Bhowmick, D. X. Cao, G. Szigethy, J. W. Ziller, M. P. Shores and A. F. Heyduk, *Chem. Sci.*, 2016, **7**, 1594–1599.

31   S. N. Brown, *Inorg. Chem.*, 2012, **51**, 1251–1260.

32   K. Ray, K. Warm, A. Paskin, U. Kuhlmann, E. Bill, M. Swart, M. Haumann, H. Dau and P. Hildebrandt, *Angew. Chemie Int. Ed.*, 2020, **60**, 2–7.

33   R. G. Pearson, *J. Am. Chem. Soc.*, 1963, **85**, 3533–3539.

34   R. S. Drago, *J. Chem. Ed.*, 1974, **51**, 300-307.

35   R. S. Drago, N. Wong, D. C. Ferris, *J. Am. Chem. Soc.*, 1991, **113**, 1970-1977.

36   R. S. Drago, S. Joerg, *J. Am. Chem. Soc.*, 1996, **118**, 2654-2663.

37   M. Valente, C. Freire and B. De Castro, *J. Chem. Soc. - Dalt. Trans.*, 1998, 1557–1562.

38   V. V Saraev, F. K. Shmidt, G. M. Larin and V. G. Lipovich, *Bull. Acad. Sci. USSR Div. Chem. Sci.*, 1974, **23**, 203–204.

39   Q. Dong, X. J. Yang, S. Gong, Q. Luo, Q. S. Li, J. H. Su, Y. Zhao and B. Wu, *Chem. - A Eur. J.*, 2013, **19**, 15240–15247.

40   Y. Dong, J. T. Lukens, R. M. Clarke, S. L. Zheng, K. M. Lancaster and T. A. Betley, *Chem. Sci.*, 2020, **11**, 1260–1268.

41   S. Wiese, M. J. B. Aguila, E. Kogut and T. H. Warren, *Organometallics*, 2013, **32**, 2300–2308.

42   V. M. Iluc, A. J. M. Miller, J. S. Anderson, M. J. Monreal, M. P. Mehn and G. L. Hillhouse, *J. Am. Chem. Soc.*, 2011, **133**, 13055–13063.

43   R. Waterman and G. L. Hillhouse, *J. Am. Chem. Soc.*, 2008, **130**, 12628–12629.

44   S. Wiese, J. L. McAfee, D. R. Pahls, C. L. McMullin, T. R. Cundari and T. H. Warren, *J. Am. Chem. Soc.*, 2012, **134**, 10114–10121.

45   D. J. Mindiola and G. L. Hillhouse, *Chem. Commun.*, 2002, 1840–1841.

46   C. Yao, X. Wang and K. W. Huang, *Chem. Commun.*, 2018, **54**, 3940–3943.

47   C. A. Laskowski and G. L. Hillhouse, *Organometallics*, 2009, **28**, 6114–6120.

48   H. X. Wang, L. Wu, B. Zheng, L. Du, W. P. To, C. H. Ko, D. L. Phillips and C. M. Che, *Angew. Chemie - Int. Ed.*, 2020, **60**, 4796–4803.

49   J. Gavenonis and T. D. Tilley, *Organometallics*, 2002, **21**, 5549–5563.

50   A. Hassner, R. Fibiger and D. Andisik, *J. Org. Chem.*, 1984, **49**, 4237–4244.

51   I. T. Alt, C. Guttroff and B. Plietker, *Angew. Chemie - Int. Ed.*, 2017, **56**, 10582–10586.

52   E. A. Standley, S. J. Smith, P. Müller and T. F. Jamison, *Organometallics*, 2014, **33**, 2012–2018.

53   T. J. Deming and B. M. Novak, *J. Am. Chem. Soc.*, 1993, **115**, 9101–9111.

54   Z. C. Dai, Y. F. Chen, M. Zhang, S. K. Li, T. T. Yang, L. Shen, J. X. Wang, S. S. Qian, H. L. Zhu and Y. H. Ye, *Org. Biomol. Chem.*, 2015, **13**, 477–486.

55   N. G. Connelly and W. E. Geiger, *Chem. Rev.*, 1996, **96**, 877–910.

56   *SAINT*, Bruker AXS Inc.: Madison, WI, 2013.

57   G. M. Sheldrick, *SADABS*, Bruker AXS Inc.: Madison, WI, 2014.

58   G. M. Sheldrick, *SHELXTL*, Bruker AXS Inc.: Madison, WI, 2014.

59   *International tables for crystallography. Vol. C: Mathematical, physical and chemical tables*, Kluwer Acad. Publ, Dordrecht, 3. ed., 2004.

60   L. J. Farrugia, *J. Appl. Crystallogr.*, 2012, **45**, 849–854.

Appendix A

Investigations into diverted pathways hindering the catalytic reaction of *p*-tolylazide and

**CN^{t}Bu with K{[ONO^{cat}]Ni(py)}**

A.1 Introduction

Nickel nitrenoid complexes are scarce in literature. Of those few reported examples, their isolation and electronic characterization have been made possible due to strategic electronic and geometric manipulation of the ligand field. The putative nickel imido complex discussed in **Chapter 5** was subject to reactivity studies to make inferences regarding the electronic assignment of the complex since its isolation remained challenging. The reaction of p-tolylazide and CN^{t}Bu with nickel catalyst, K{[ONO^{cat}]Ni(py)} revealed the formation of the nitrene transfer product, carbodiimide, however in stoichiometric yields with no catalytic turnover. Investigations into potential diverted pathways and side products formed in this reaction would give insight into the electronic assignment of the putative nickel imido and suggest routes to increased catalytic activity.

A.2 Results and Discussion

To deconstruct the electronic assignment of the putative nickel imido K{[ONO^q]Ni(N-tolyl)} species, the complex was subject to further reactivity. First, the blue solution of K{[ONO^q]Ni(N-tolyl)} was exposed to two equivalents of PPh$_3$. This reaction, shown in **Scheme A.1**, was expected to expel phosphinimide along with the previously characterized K{[ONO^{cat}]Ni(PPh$_3$)}.

Scheme A.1. Reaction of putative K{[ONO^q]Ni(N-tolyl)} and PPh$_3$.
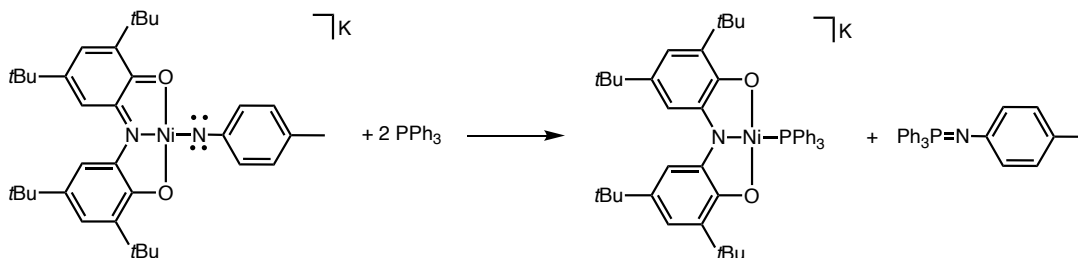
Both products of this reaction have been previously characterized by $^{31}P\{^1H\}$ NMR spectroscopy with peaks around -1.1 and 20 ppm, respectively. Monitoring this reaction by multinuclear NMR, both ^1H and $^{31}P\{^1H\}$ (**Figure A.1**), revealed the expected products; however, when integrated against an internal standard of hexamethylbenzene, only 10 % conversion was obtained after 24 h with no change after an additional 24 h. The limited conversion was reminiscent of the 10 % conversion or stoichiometric reactivity observed from the initial catalytic conditions reported in Section 5.2.4.
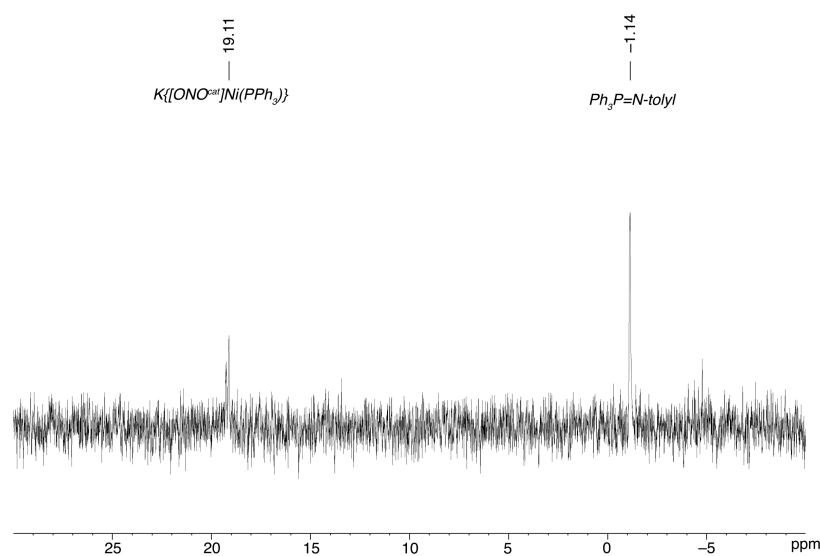

Figure A.1. $^{31}P\{^1H\}$NMR spectrum of the reaction of K{[ONO^q]Ni(N-tolyl)} and 2 PPh$_3$.

Concurrently, a crystal setup of the putative K{[ONO^q]Ni(N-tolyl)} complex with potassium encapsulating agent 2.2.2.-cryptand in cold Et$_2$O at –36 ˚C yielded a blue prismatic crystal suitable for diffraction. The X-ray diffraction data of this crystal revealed a singly oxidized [ONO•] ligand and a hydroxide bound to a nickel metal center with formula K(2.2.2.-cryptand){[ONO•]Ni(OH)}. It is thought that the hydroxide is sourced from trace H$_2$O introduced from the 2.2.2. cryptand. **Figure A.2** shows the structure of K(2.2.2.-cryptand){[ONO•]Ni(OH)} with relevant bond metrics reported in **Table A.1**. The τ_4 value of 0.08 revealed a square-planar geometry about the metal center and intra-ligand O–C and N–C bond distances suggest a singly

oxidized [ONO•] ligand bound to a nickel (II) metal which is further corroborated by a MOS value

of –2.15. The mother liquor from the crystal setup described above was reduced in volume and

analyzed by ^{1}H NMR, and GC-MS and both methods revealed the formation of *p*-toluidine. The

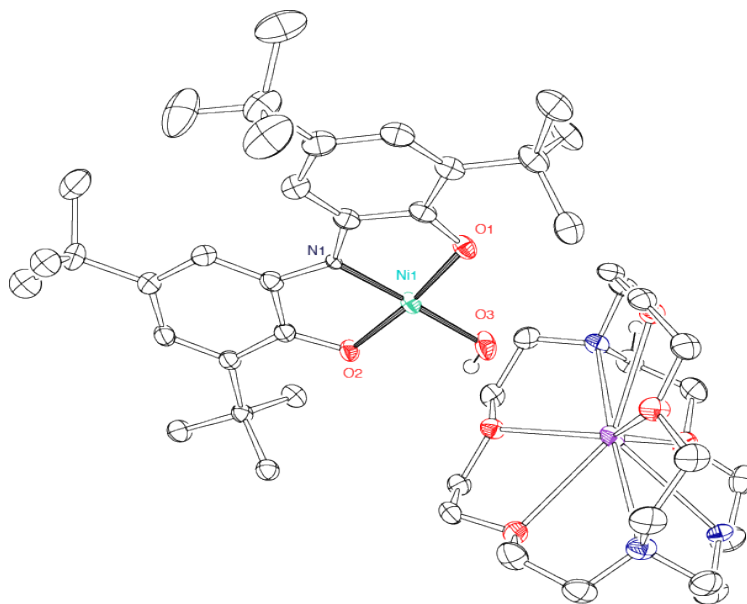formation of *p*-toluidine led to the investigation of potential anilido [ONO]-nickel complexes.

Figure A.2. Solid-state structure of K(2.2.2.-crypt){[ONO•]Ni(OH)} with thermal ellipsoids set at 50 % probability. Hydrogen atoms and solvent molecules (Et$_2$O) are omitted for clarity.

Table A.1. Selected bond distances (Å) from solid-state structures of K(2.2.2.-crypt){[ONO$^{\bullet}$]Ni(OH)} and K$_2$(2.2.2.-crypt)$_2$ [ONO^{cat}]Ni(OH).

	K(2.2.2.-crypt){[ONO$^{\bullet}$]Ni(OH)}	K$_2$(2.2.2.-crypt)$_2$ [ONO^{cat}]Ni(OH)
Ni–O(1)	1.88091(13)	1.86294(7)
Ni–O(2)	1.86230(13)	1.87566(7)
Ni–N(1)	1.81536(10)	1.81554(7)
Ni–N(2)	--	--
Ni–O(3)	1.80738(10)	1.89294(7)
O(1)–C(1)	1.32291(9)	1.34426(5)
O(2)–C(8)	1.32795(7)	1.34150(4)
N(1)–C(6)	1.37964(9)	1.39469(4)
N(1)–C(7)	1.38373(10)	1.38262(6)
τ_4	0.077	0.090
Calc. MOS	-2.15	-2.70

While isolation and characterization of a nickel imido remained challenging, another route was considered. It has been established that the auxiliary ligand, PPh$_3$, can be easily displaced by various other ligands, including pyridine. To obtain a potential reactive anilido intermediate, an exchange reaction with K{[ONO^{cat}]Ni(PPh$_3$)}, shown in **Scheme A.2** was pursued with 2,6-diisopropylanilido. The 2,6-diisopropylaniline was deprotonated using KH and was then subject to addition of a THF solution of green, K{[ONO^{cat}]Ni(PPh$_3$)}. The yellow solution of 2,6-diisopropylanilido turned purple upon addition of K[{ONO^{cat}]Ni(PPh$_3$). After 18 hours, both reactions were reduced to dryness and washed with ample amounts of cold pentane.

Scheme A.2. Ligand displacement of K{[ONO^cat]Ni(PPh₃)} with 2,6-diisopropylanilido.
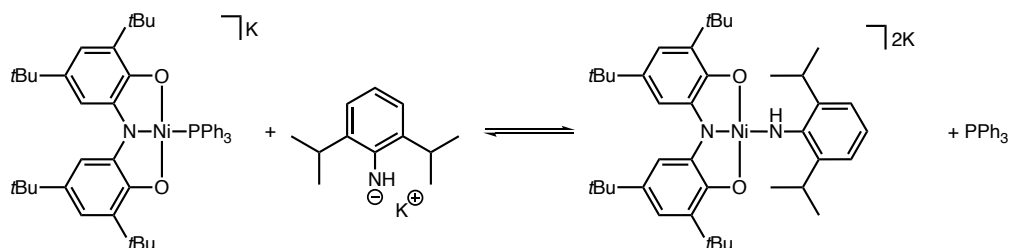
The purple solid, $K_2[\{ONO^{cat}\}Ni(NH\text{-}2,6\text{-}(C_3H7)_2C_6H_3)$ was analyzed by ${}^1H$ NMR to reveal C_{2v} symmetry with 4 aromatic resonances attributed to the [ONO] π system and the phenyl ring of the anilido, 4 singlets in the alkyl region for the 4 *tert*-butyl group and 4 methyl groups of the isopropyl groups and a characteristic quartet for the isopropyl methyne proton. A single crystal was obtained from an Et₂O solution of $K_2[\{ONO^{cat}\}Ni\ NH\text{-}2,6\text{-}(C_3H7)_2C_6H_3)\}$ in the presence of encapsulating agent 2.2.2.-cryptand. However, again X-ray diffraction data revealed a fully reduced [ONO] ligand bound to a nickel metal center with a hydroxide and two potassium ions encapsulated with 2.2.2. cryptands. **Figure A.3** shows the structure of the $\{K(2.2.2.\text{-}cryp)\}_2\{[ONO^{cat}]Ni(OH)\}$ complex with relevant bond metrics reported in **Table A.1**.
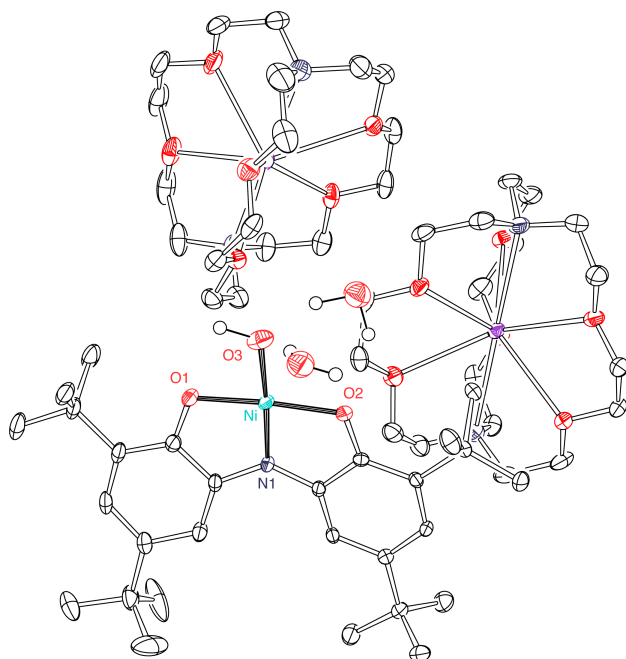
Figure A.3. Solid-state structure of {K(2.2.2.-crypt)}$_2${[ONO^{cat}]Ni(OH)} with thermal ellipsoids set at 50 % probability. Hydrogen atoms and solvent molecules (Et$_2$O) are omitted for clarity.

Despite the results of the solid-state analysis, which was predicted to be the results of trace H$_2$O introduced from the 2.2.2.-cryptand, chemical oxidation of K$_2$[{ONO^{cat}}Ni(NH-2,6-(C$_3$H$_7$)$_2$C$_6$H$_3$)} was sought out. Treatment of K$_2$[{ONO^{cat}}Ni(NH-2,6-(C$_3$H$_7$)$_2$C$_6$H$_3$)} with one equivalent of silver tetrafluoroborate (AgBF$_4$) resulted in a blue paramagnetic solution. This solution was reduced to dryness and analyzed by EPR spectroscopy. The spectrum, shown in **Figure A.4A**, is described by a rhombic signal with g values at 2.02, 2.01, and 1.98 and ^{14}N hyperfine interactions with A(^{14}N) = 41, 28, and 56 MHz. Additionally, attempts to oxidize with AgBF$_4$ and deprotonate with triethylamine (Et$_3$N), the same anilido complex resulted in a blue solution. A single crystal, suitable for diffraction, was obtained from a concentrated solution of this reaction mixture in Et$_2$O at –36 ˚C however, the unit cell of this crystal matched that of [ONO•]Cu(Et$_3$N)[1] suggesting the Et$_3$N displaced the anilido to afford [ONO•]Ni(Et$_3$N). This complex was paramagnetic and displayed a rhombic EPR signal (**Figure A.4B**) with g values at

151

2.01, 2.01, and 1.98 with ^{14}N hyperfine interaction with $A(^{14}N) = 37$, 11, and 54 MHz, indicative of the [ONO•] radical.
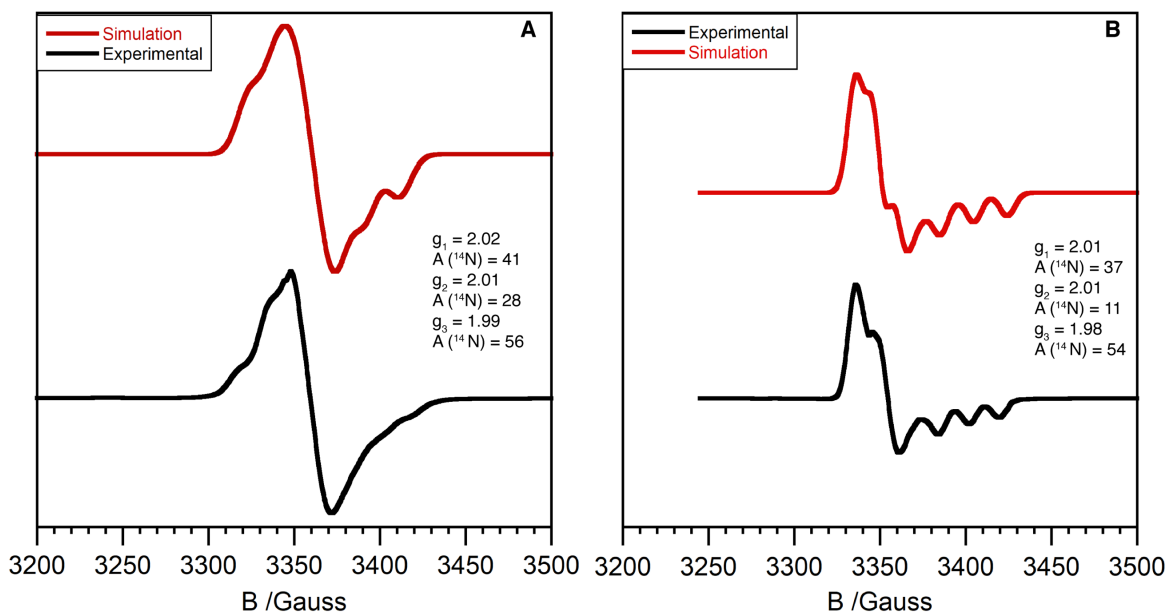

Figure A.4. X-band EPR spectrum of K{[ONO•]Ni(NH-2,6-(C$_3$H$_7$)C$_6$H$_3$)} (A) and [ONO•]Ni(Et$_3$N) (B) in toluene at 77 K with experimental spectrum shown in black and simulation in red.

Attempts to isolate a putative nickel imido complex proved helpful in discussing potential catalytic poisons and decomposition pathways. X-ray diffraction data provided a structure of K(2.2.2.-crypt){[ONO•]Ni(OH)} with the [ONO] ligand in its singly oxidized semiquinonate form. The structure provided some insight into contaminants in the reaction mixture. **Scheme A.3** shows potential pathways that result in hindered catalysis due to solvent interference.

Scheme A3. Potential diverted pathways during nitrene transfer reactivity from K{[ONO^cat]Ni(py)} and *p*-tolylazide.
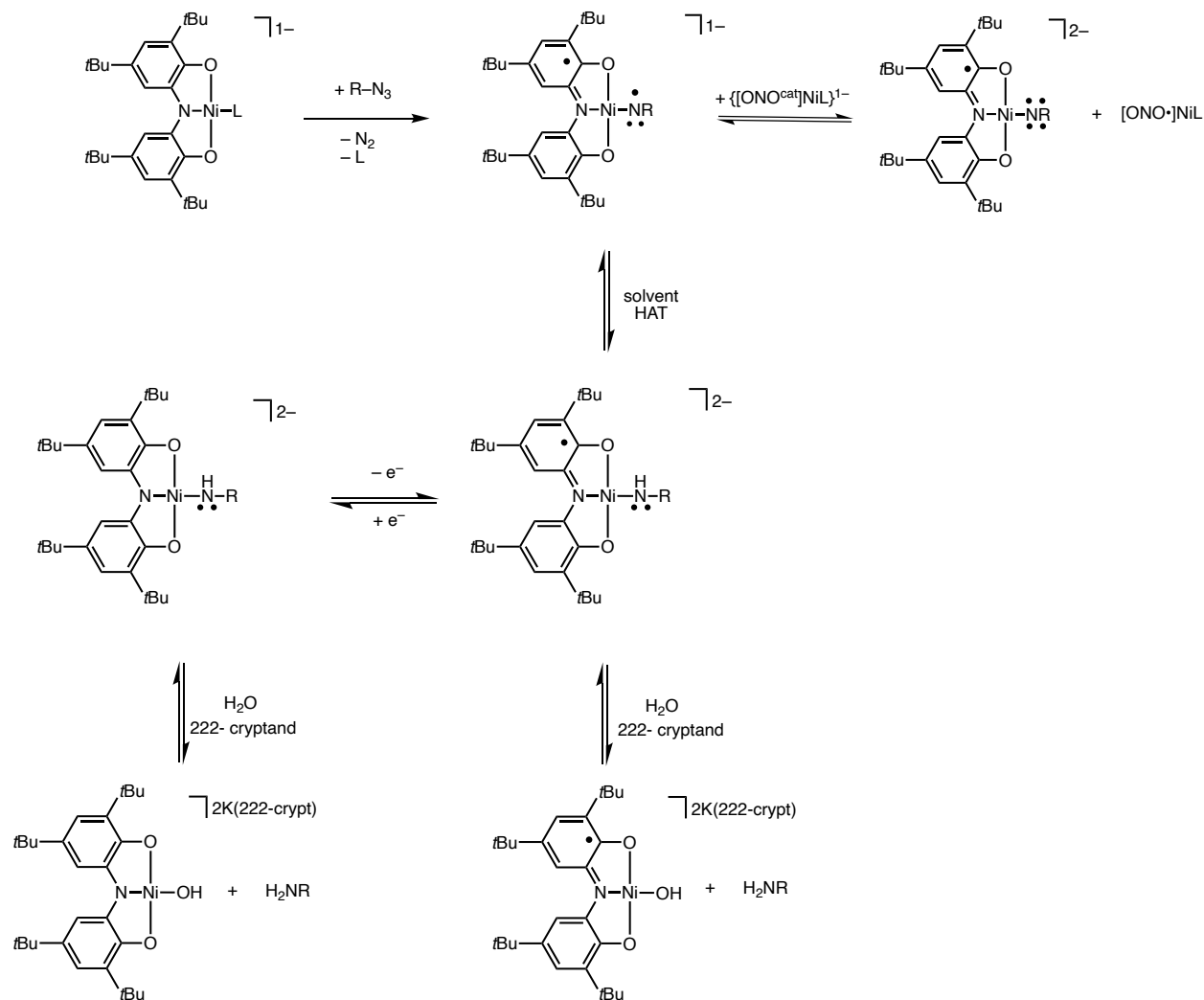
As discussed in Chapter 3 Section 3.1, there exists several viable oxidation-state assignments for transition metal nitrenoid complexes and the incorporation of redox-active ligands add more oxidation-state options. The putative nickel imido complex K{[ONO^q]Ni(N-tolyl)} could exist as the valence tautomer K{[ONO•]Ni(•N-tolyl)}, the nickel imnyl. If this tautomer is favored, it is thought that if there is residual THF from complex synthesis, an H-atom abstraction from THF (BDE = 92 kcal mol^{-1})[2] could occur to afford an anilido, K{[ONO•]Ni–(NH-tolyl)}. This anilido K{[ONO•]Ni–NH-tolyl} complex would then deprotonate trace H$_2$O introduced with

153

the 2.2.2.-cryptand and afford the K(2.2.2.-crypt){[ONO•]Ni(OH)} and *p*-toluidine, shown during

analysis of the mother liquor from the crystal. Attempts to independently synthesize this anilido

complex {[ONO•]Ni–(NH-tolyl)}$^{1-}$ from ligand displacement from the {[ONO^{cat}]Ni(PPh$_3$)}$^{1-}$

followed by chemical oxidation were then sought out. 2,6-disisoprolyaniline was used instead of

p-toluidine in attempts to sterically protect a potential Ni–NR bond. The ligand displacement

proceeds cleanly to afford K$_2$[ONO^{cat}]Ni(NH(2,6-(C$_3$H$_7$)C$_6$H$_3$)}. However, in the presence of the

same 2.2.2.-cryptand, a hydroxide complex K$_2$(2.2.2.-crypt)$_2${[ONO^{cat}]Ni(OH)} was crystallized.

Despite the solid-state data, in the absence of cryptand, solution NMR analysis suggested clean

conversion; therefore, the K$_2${[ONO^{cat}]Ni(NH(2,6-(C$_3$H$_7$)C$_6$H$_3$)} complex was subject to

oxidation with AgBF$_4$ and analyzed by EPR spectroscopy. The EPR spectrum was similar to one

of the species from the reaction of K{[ONO^{cat}]Ni(py)} with *p*-tolylazide with a rhombic signal

with g values ~2 and similar ^{14}N hyperfine values, suggesting this is a signature of the [ONO•]

radical ligand.

A.3 Conclusion

The investigation into the potential diverted pathways that hinder the catalytic activity of

p-tolylazide and CN^{t}Bu over K{[ONO^{cat}]Ni(py)} showed that trace solvent interfered with

catalytic turnover. Residual tetrahydrofuran from K{[ONO^{cat}]Ni(py)} synthesis provides an H-

atom the transient nickel iminyl to abstract and form a nickel anilido complex. The isolation of the

two nickel hydroxide complexes indicates that trace water was introduced with the 2.2.2.-cryptand.

The nickel anilido complexes generated from both the HAT of THF and independent synthesis,

were both able to deprotonate water to afford their corresponding anilines and nickel hydroxide

complexes. EPR spectra of the products of oxidation of the independently prepared nickel anilido

complex showed similar spectroscopic signatures discussed in Chapter 5 for the signal for the

[ONO•] ligand. The results from this work suggest methods to increase the catalytic activity of the nitrene transfer facilitated by the K{[ONO^{cat}]Ni(py)} complex.

A.4 Experimental

General Considerations. The compounds and reactions reported below show various levels of air- and moisture- sensitivity; therefore, all manipulations were performed using standard Schlenk-line and glovebox techniques. Hydrocarbon and ethereal solvents were sparged with argon before being deoxygenated and dried by passage through Q5 and activated alumina columns, respectively. Halogenated solvents and triethylamine were sparged with argon and passed through two activated alumina columns. 2.2.2. cryptand, PPh$_3$, and AgBF$_4$ were used as received. Potassium hydride was obtained in mineral oil and washed with pentane prior to use. 2,6-diisopropylanline was distilled and freeze pump-thawed thrice and stored over sieves.

Physical Methods. NMR spectra were collected at 298 K on a Bruker Avance 400 MHz or 600 MHz spectrometer in dry, degassed C$_6$D$_6$, or CD$_3$CN. ^{1}H NMR spectra were referenced to tetramethylsilane (TMS) using residual proteo impurities of the solvent (7.16 ppm, or 1.93 ppm) and ^{31}P{^{1}H} NMR spectra were referenced with an external standard of phosphoric acid (H$_3$PO$_4$, 85%, 0.00 ppm). All chemical shifts are reported in standard δ notation in parts per million. Perpendicular-mode X-band (9.352 GHz) EPR spectra were collected at 77 K using a Bruker EMX spectrometer equipped with ER041XG microwave bridge. The following spectrometer settings were used: attenuation = 20 dB, microwave power 1.997 mW, frequency = 9.352 GHz, modulation amplitude = 10.02 G, gain = 1.00 x 10^3, conversion time = 4.91 ms, time constant = 81.92 ms, sweep width 5500 G and resolution 1024 points. The spectra were simulated using EasySpin for MATLAB. Electrospray ionization mass spectrometry (ESI-MS) data were collected on a Waters LCT Premier mass spectrometer using dry, degassed MeCN or THF.

Crystallographic Methods. X-ray diffraction data were collected at low temperatures on single crystals covered in Paratone and mounted on glass fibers. Data were acquired using a Bruker SMART APEX II diffractometer equipped with a CCD detector. Measurements were carried out using Mo K_α (λ = 0.71073 Å) radiation, which was wavelength selected with a single-crystal graphite monochromator. A full sphere of data was collected for each crystal structure. The SMART program package was used to determine unit-cell parameters and to collect data. The raw frame data were processed using SAINT[3] and SADABS[4] to yield the reflection data files. Subsequent calculations were carried out using the SHELXTL[5] program suite. Structures were solved by direct methods and refined on F^2 by full-matrix least-squares techniques to convergence. Analytical scattering factors for neutral atoms were used throughout the analyses.[6] Hydrogen atoms, though visible in the difference Fourier map, were generated at calculated positions, and their positions refined using the riding model. ORTEP diagrams were generated using ORTEP-3[7] for Windows.

Synthesis of $K_2\{[ONO^{cat}]Ni(NH-2,6-(C_3H_7)C_6H_3)\}$ In a scintillation vial in a nitrogen filled glovebox, 2,6-diisopropylaniline (24 µL, 128 µmol, 1 equiv.) was deprotonated with KH (5 mg, 128 µmol, 1 equiv.) in THF (5 mL). Once the bubbles ceased a green solution of $K\{[ONO^{cat}]Ni(PPh_3)\}$ (100 mg, 128 µmol, 1.0 equiv.) in THF (10 mL). The reaction stirred at room temperature for 1 hour, when the brown solution was filtered through Celite using a medium porous fritted funnel and washed with 5 mL THF. The filtrate volatiles were concentrated to 5 mL and precipitated with 30 mL of pentane. The brown solid was washed with cold pentane (20 mL) to afford a purple solid in a 65 % yield (56 mg) ^{1}H NMR (CD$_3$CN, 400 MHz) δ/ppm : 7.03 (s, 2H, aryl-H), 6.96 (d, J = 8 MHz, 2H, aryl-H), 6.67 (t, J = 8 MHz, 1H, aryl-H), 6.07 (s, 2H, aryl-H),

2.94 (q, J = 6.8 MHz, 2H, -C*H*(C$_2$H$_6$)), 1.23 (s, 36H, -C(C*H*$_3$), 1.21 (s, 6H, -CH(C$_2$*H*$_6$)), 1.89 (s,

6H -CH(C$_2$*H*$_6$)),. λ_{max} / nm (ϵ/ M^{-1}cm^{-1}): 394 (900) .
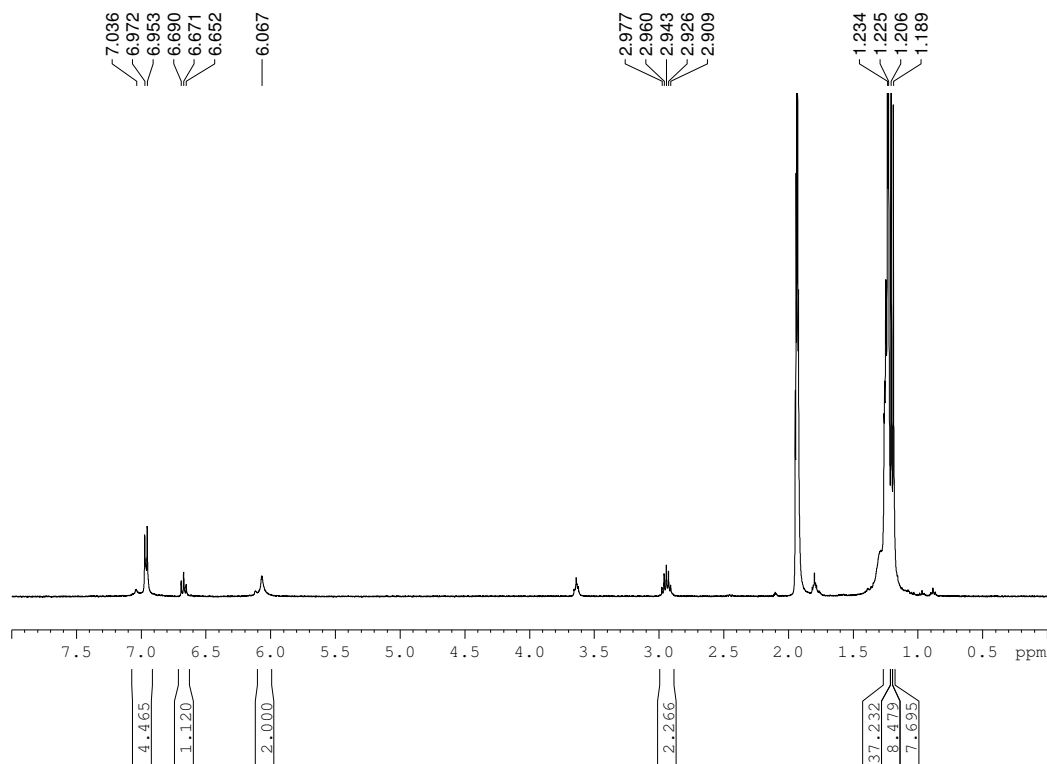
Figure A.5. ^{1}H NMR spectrum of K$_2${[ONO^{cat}]Ni(NH-2,6-(C$_3$H$_7$)C$_6$H$_3$)} in d$_3$-ACN at room temperature.

A.5 References

1   P. Chaudhuri, M. Hess, T. Weyhermüller and K. Wieghardt, *Angew. Chemie - Int. Ed.*, 1999, **38**, 1095–1098.
2   H. X. Wang, L. Wu, B. Zheng, L. Du, W. P. To, C. H. Ko, D. L. Phillips and C. M. Che, *Angew. Chemie - Int. Ed.*, 2020, **60**, 4796–4803.
3   *SAINT*, Bruker AXS Inc.: Madison, WI, 2013.
4   G. M. Sheldrick, *SADABS*, Bruker AXS Inc.: Madison, WI, 2014.
5   G. M. Sheldrick, *SHELXTL*, Bruker AXS Inc.: Madison, WI, 2014.
6   *International tables for crystallography. Vol. C: Mathematical, physical and chemical tables*, Kluwer Acad. Publ, Dordrecht, 3. ed., 2004.
7   L. J. Farrugia, *J. Appl. Crystallogr.*, 2012, **45**, 849–854.

Everything will be okay in the end. If it's not okay, it's not the end. –John Lennon